Department of Pure and Applied Chemistry

University of Strathclyde

Understanding Cholesterol Modified Nanoparticles as Photothermal Agents for Cardiovascular Disease Studies

Fatima Ali

A thesis presented to the Department of Pure and Applied Chemistry, University of Strathclyde, in fulfilment of the requirements for the degree of Doctor of Philosophy.

Fatima Ali

University of Strathclyde

Signed: Date:

"There is always light at the end of the tunnel"

Acknowledgments

The PhD journey is a test of an individual's dedication, patience, and perseverance. Although one must cross the finishing-line alone, the journey is impossible without the help, support, and love of certain individuals. This success is attributed to those who helped me along the way….

First and foremost, my sincerest gratitude to my supervisors Prof. Duncan Graham and Prof. Karen Faulds for this opportunity, for having faith in me that I could do it! Thank you for your support and advice along the way. Furthermore, I will always be grateful to Prof. Ewen Smith for investing his time to provide us with Raman tutorials, for his extensive discussions, and helping me whenever I asked him. Thank you ever so much!

To the 'pillars' of bionano, the post-docs (past and present). Thank you for all your help and support over the years and for answering all my stupid questions! Corinna, thank you for teaching me how to culture cells and for always listening to me when I wanted to off-load, oh, and for your hugs also! My greatest appreciation for Dr. Will Tipping, Dr. Hayleigh May, and Dr. Sian Sloan Dennison, who took the time to read over chapters and provide me with feedback. Will, thank you for all the cell lab 'bants,' for always being supportive when I'd come running for help and always listening to me. Your advice and help have been invaluable. Hayleigh, I cannot even begin to thank you. Your support throughout the entire journey has been so precious to me, especially towards the end when it was a 'rocky ride.' For always reassuring me that I would be fine, thank you for all the 'pep' talks, advice, and help. I will never forget it! We were the 'dream team' and it will always remain like that.

To the entire bionano group, past and present! I, whole-heartedly thank each one of you for your genuine friendship, love, care, during my time with

the group. All the happy memories made will forever remain with me. Yosemite, (Matthew, Andrew, Sam, Marie, and Bethany), I will miss the frequent gossip sessions and all the love I got from you all. P.s. Sam, our pizza catch-ups need to continue. Maria and Melissa, thank you for carrying out the SEM analysis for me, especially towards the end when I needed the images asap.

To the best cohort (Iona, Emma, and Bethany). You girls will forever hold a special place in my heart. This journey was so much easier with your support. Thank you for being there when I needed to off-load, cry about bad results, or celebrate. For constantly reassuring me that I was going to reach the end line. Bethany, my desk neighbour/bestie/advisor/consoler all in one! 'Started from the bottom and now we here.' Your constant support and encouragement right from the beginning have been invaluable. Thank you for being my desk and travel buddy! I'm going to miss our afternoon walks, dessert missions, and other adventures we went off on!

My dearest, my family. The people who had to put up with a stressed, torn, emotional Fatima. Mum and dad, this one is for you! Your unconditional and pure love throughout the entire process made this journey bearable. I am who I am today because of you. My siblings, Asim, Qasim, Hamzah, and Aminah who had no choice but to put up with me, thank you for your love and for always cheering me up. Especially to Asim, who was especially supportive throughout the PhD journey and in the write-up stage. Constantly making sure I was okay, reassuring me, and asking if I needed anything, I will always be grateful for your efforts and love.

Above all, I acknowledge the One who is the All-Knowing. From whom all knowledge emanates…

Abstract

Atherosclerosis is the primary reason for Cardiovascular disease, in which arteries become narrowed due to plaque development. Accumulation of low-density lipoprotein (LDL-C) at the site of damage (the endothelium) is known to be a key factor in the pathogenesis of atherosclerosis. By targeting the site of damage, subsequently utilising photothermal therapy should effectively halt or stop the atherosclerotic process. Lipid modifications are known in the literature to increase cellular interactions. Cholesterol is a lipid, which can be functionalised onto nanoparticles potentially increasing uptake of gold nanoparticles. This essentially creates a 'fatty nanoparticle' which can also imitate LDL-C, hence being able to target plaques.

Herein, the research focus was to investigate the cellular uptake of cholesterol modified nanoparticles and upon success, their capabilities as photothermal agents for targeting plaque sites. Gold nanoparticles were functionalised with cholesterol-DNA. Thereafter, a series of *in vitro* studies were carried out using two cell lines: RAWs and HUVECs, to determine cellular uptake. Using 2D and 3D SERRS mapping, the first study determined successful uptake and the second study determined that the uptake was greater in endothelial cells. A 'semi-quantitative' method was applied to calculate the % relative SERRS response from each cell line, allowing for comparisons to be made. Cell viability studies confirmed the non-toxic nature of these probes.

In the second part of this research, HGNs were used as the core for these 'fatty nanoparticles' due to their LSPR in the NIR, and commendable photothermal properties. Cholesterol modified HGNs displayed efficient cellular ablation with an in-house photothermal setup.

This work successfully provided the basis for using cholesterol modified nanoparticles as photothermal agents in the treatment of CVD.

Abbreviations

2D	Two-Dimensional
3D	Three-Dimensional
a.u.	Arbitrary Units
AgNPs	Silver Nanoparticles
AuNPs	Gold Nanoparticles
Chol-DNA	Cholesteryl-TEG DNA
CVD	Cardiovascular Disease
CW	Continuous Wave
DCLS	Direct Classical Least Squares
DLS	Dynamic Light Scattering
DNA	Deoxyribonucleic Acid
dsDNA	Double-stranded DNA
FDA	Food and Drug Administration
FWHM	Full-Width-Half-Maximum
HDL-C	High-Density Lipoprotein cholesterol
HGNs	Hollow Gold Nanoparticles
HUVECs	Human Umbilical Vein Endothelial Cells
ICAM-1	Intercellular Adhesion Molecule-1
LDL-C	Low-Density Lipoprotein Cholesterol
LSPR	Localised Surface Plasmon Resonance
MBA	4-Mercaptobenzoic Acid
MG	Malachite Green
MGITC	Malachite Green Isothiocyanate

NIR	Near-Infrared Region
NPs	Nanoparticles
PBS	Phosphate Buffer Saline
PBST	Phosphate Buffer Saline with Tween 20™
PEG	Polyethylene Glycol
PFA	Paraformaldehyde
Poly-T DNA	Poly-Thymine DNA
PPTT	Plasmonic Photothermal Therapy
PTT	Photothermal Therapy
RNA	Ribonucleic Acid
RRS	Resonance Raman Scattering
SEM	Scanning Electron Microscopy
SERRS	Surface Enhanced Resonance Raman Spectroscopy
SERS	Surface Enhanced Resonance Spectroscopy
SHE	Standard Hydrogen Electrode
SMC	Smooth Muscle Cells
SPR	Surface Plasmon Resonance
SRS	Stimulated Raman Spectroscopy
ssDNA	Single-stranded DNA
TEG	Triethylene Glycol
TEM	Transmission Electron Microscopy
VCAM-1	Vascular Cell Adhesion Molecule-1
WHO	World Health Organisation
WiRE™	Windows®-based Raman Environment

Table of Contents

1. Introduction

1.1 Cardiovascular Disease

Cardiovascular Disease (CVD) is a collective term used to define diseases of the heart and its blood circulation, describing conditions such as coronary artery disease, stroke and angina. Classified as one of the most prevalent disease states, it is generally accountable for more than a quarter (27%) of all deaths in the UK, approximating to one death every three minutes.[1] Worldwide, as per the World Health Organisation (WHO), an estimated 17.9 million people die from CVD diseases each year.[2] Factors such as obesity, smoking, and inactiveness are a few of the underlying reasons which trigger CVD, highlighting the ability of a healthy lifestyle preventing such a condition.[3] In parallel to the number of fatalities, CVD has a huge economic impact costing the UK economy £9 billion each year and with longer life expectancies, this figure is guaranteed to rise.[1]

1.1.1 Atherosclerosis

CVD is mainly dependent on atherosclerosis: a chronic, progressive, inflammatory disease resulting from the build-up of plaque in the artery wall.[4] Consequently, narrowing and hardening the artery, and restricting blood flow to and from the heart. Without any or delayed intervention, it can become life-threatening, thus resulting in serious outcomes i.e., a stroke or myocardial infarction. Figure 1.1 illustrates the development of a plaque in an artery.
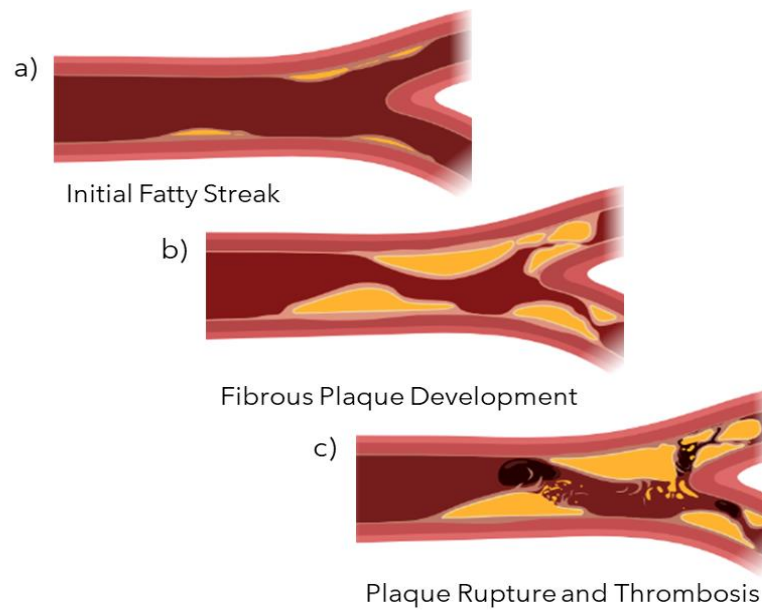
Figure 1.1: Schematic illustrating plaque development in an artery. (a) The atherosclerotic process begins with an initial fatty streak, (b) this continues to develop into a fibrous plaque, and finally, (c) the plaque ruptures, resulting in myocardial infarction or a stroke occurring.

With an asymptomatic phase, atherosclerosis begins in the early years of humans and progresses over time, through multiple stages, as detailed below: [3,5,6]

I.   Endothelial dysfunction: Damage to the endothelial cell lining subject to irritative stimuli such as hypertension, hypercholesterolemia, etc, allowing entry and retention of low-density lipoprotein-cholesterol (LDL-C) and triggering an inflammatory response.

II. Inflammatory Response: Cell adhesion molecules: ICAM-1, VCAM-1, and P-selectin are upregulated, recruiting inflammatory response cells such as monocytes and leukocytes into the activated subendothelial matrix.

III. Foam Cells/Initial Fatty Streak: Monocytes entering into the subendothelial space, differentiate into macrophages, subsequently forming foam cells upon accumulating oxidised-LDL. As a result, a fatty streak forms.

IV. Plaque Growth: Smooth muscle cell (SMC) migration and proliferation occurs. Together with the accumulation of lipid-rich necrotic debris and SMC, plaque growth persists. The body reacts by forming a fibrous cap around the plaque.

V. Initial Clinical Events: Calcium deposits on the plaque harden and restrict artery movement. Blood flow is also reduced. Therefore, clinical events such as angina occur.

VI. Thrombosis: Increased pressure within the artery results in the plaque rupturing, which can lead to events such as myocardial infarction and stroke. Clot break-offs can travel and block other arteries downstream.

Differing opinions exist on the primary contributor to this series of biological events. Some believe that endothelial dysfunction and upregulation of LDL-C are the main reason, acting as a trigger to the cascade of events which follow.[6] However, others believe that macrophages differentiating to foam cells are the principal reason, as foam cells extensively contribute to the bulking of the plaque.[7] Amidst all the opinions, the former is thought to be stronger.[5,6]

1.1.2 An Insight into Cholesterol

Colloquially known as 'a ball of fat,' cholesterol is an essential biomolecule to the human body. It is synthesised by hepatocytes in the liver, with certain foods also being a source.[8] Although this hydrophobic lipid has the main function of maintaining cellular structure, it also serves as a precursor for the synthesis of substances vital to the body, such as steroid hormones and vitamin D.[9] Cholesterol in the body can exist as unesterified (free) or esterified. Free cholesterol is biologically active and possesses cytotoxic effects in comparison to the cholesteryl esters which are the protective form for storage in cells and transport through the plasma.[10] The structure of cholesterol is given in Figure 1.2 and the biosynthesis pathway of cholesterol is provided in Appendix 1.
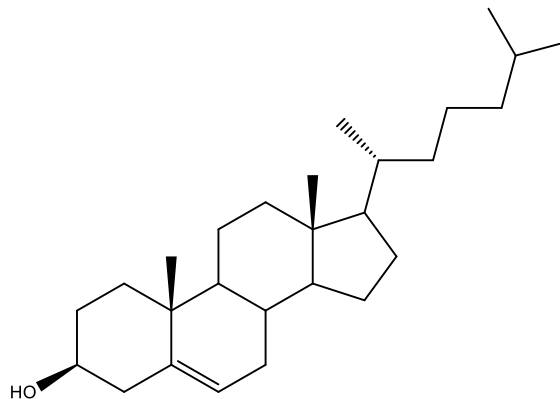
Figure 1.2: Structure of an independent cholesterol molecule. In the body, cholesterol can exist in other forms such as cholesteryl esters.

Due to cholesterol being water-insoluble, it is unable to travel through the bloodstream alone, hence it is transported around the body by macromolecular complexes known as lipoproteins.[11] In the 1950s and 1960s, physiologists put forth the two major cholesterol carrying lipoproteins. These are identified as LDL-C (low-density lipoprotein-

cholesterol) and HDL-C (high-density lipoprotein cholesterol), also known as bad and good cholesterol respectively.[12,13] Elevated levels of LDL-C in the blood have strongly been associated with atherosclerotic events. Derivation of the disease name comes from the Greek words 'athere' meaning accumulation of lipid and 'sclerosis' referring to hardening.[14] A schematic depicting the cross-section of LDL-C is shown in Figure 1.3.
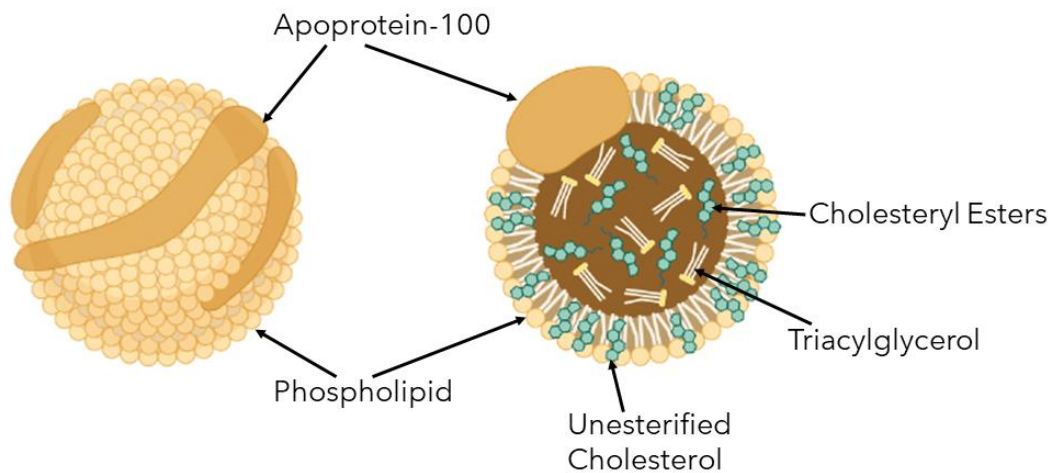
Figure 1.3: Cross-section of LDL. The external layer is made up of phospholipids and free cholesterol, encasing a hydrophobic core of cholesteryl esters and triacylglycerols. Image reproduced (adapted) with permission from Encyclopaedia Brittanica, Inc.

Vogel *et al.* first linked cholesterol and atherosclerosis together when he identified deposits of cholesterol in the artery wall in the 1840s.[15] The pioneering work of Alexander I. Ignatowski, in which he fed rabbits protein and dairy to effectively induce atherosclerosis, confirmed this relationship.[16,17] His work allowed scientists to intensify the research to help elucidate the atherosclerotic mechanism, which we understand today.

The understanding that LDL-C is a favourable contender in the development of atherosclerosis stemmed the interest of investigating the role of synthesised 'fatty particles' *in vitro*, in this study. Furthermore, this would help to decipher whether using these as photothermal agents could allow

for a potential therapy method for atherosclerosis. This will be spoken about in greater detail in section 1.3.2.

1.1.3 Current Treatment Methods for Atherosclerosis

Treatment for atherosclerosis is dependent on the severity of the condition. In cases where disease progression is within the early stages, and there is no considerable damage to the artery, patients are advised to maintain a healthy lifestyle, with attention to diet, exercise, and abstaining from smoking.[4] Aside from this, statins can be prescribed to the patient as a first-line therapy method.

Statins are prescription-based lipid-lowering drugs designed to reduce the high levels of LDL-C in the serum. These 3-hydroxy-3-methylglutaryl coenzymes A reductase (HMG CoA-reductase) inhibitors target the rate-limiting step of the mevalonate pathway. Their high affinity for HMG CoA reductase allows them to significantly block mevalonate, which is a necessary precursor in cholesterol biosynthesis.[18,19] Added to this is the fact that statins also possess 'pleiotropic effects,' a term which collectively describes beneficial effects of statins, independent of cholesterol levels. Its advantageous properties concerning CVD include improved endothelial function, reduced vascular inflammation, and increased atherosclerotic plaque stability.[20] Various trials investigating the strengths of various statins have demonstrated that these drugs decrease the rate of atherosclerotic disease progression, and also under some circumstances, are shown to regress the plaque development.[4,21-23]

Unfortunately, in extreme cases where the disease has substantially progressed and the artery/arteries are considerably narrowed with reduced blood flow, surgical procedures have to be carried out. These surgeries aim to either: widen the narrowed artery using a balloon or stent (coronary angioplasty), remove the built-up plaque (carotid endarterectomy), or carry

out a bypass to redirect the flow of blood (coronary artery bypass grafting).[24] The aforementioned list of procedures does not encompass the entirety of surgical interventions available as this is out with the scope of this thesis work, however, it should be noted that other surgical procedures do exist.[25] Recent advances in treatment methods include photothermal therapy (PTT), in which a photothermal agent is directed towards the site of interest and with applied heat, can dissipate that heat to the surrounding environment, ablating atherosclerotic lesions.[26] Nanoparticles are suitable photothermal agents due to their ability to penetrate deep into biological tissue and also become activated using a near-infrared region (NIR) laser.[27] A greater insight is provided in section 1.3.2.

1.2 Nanotechnology

The concept of nanotechnology was first spoken off in a lecture titled: 'There's Plenty of Room at the Bottom' by Richard Feynman, in 1959.[28] His vision was the birth of nanotechnology, although the official name was coined by Norio Taniguchi in the 1970s.[29] These visionaries paved the path to today's rapidly evolving field of science, particularly beneficial in areas of human health care and medicine.[29-31] Nanotechnology is a referral to materials with dimensions between 1-100 nanometres (nm).[32] Their size and shape dependent properties, which differ from their bulk behaviour, are seen to be attractive for numerous applications. Typically, nanostructures are obtained using two general strategies: the 'Bottom-up' and 'Top-down' methods. The former utilises atoms produced from the reduction of ions, which assemble to generate nanostructures. The latter produces the desired nanostructure through the removal of the nanomaterial from bulk material.[33]

Over the last couple of decades, metallic materials have attracted particular attention, evident from the increasing number of publications, especially

with gold (AuNPs) and silver nanoparticles (AgNPs), since the start of the 21st century.[33]

1.2.1 The History of Nanoparticles

Nanoparticles (NPs) have existed for many centuries. Plausibly, the earliest, well-known example is the famous Lycurgus Cup (Figure 1.4), which has been dated back to the 4th century AD.[34] The cup was seen as extraordinary due to its dichroic glass, showing a jade-green colour in reflected light and a ruby-red colour in transmitted light.[34] This phenomenon was attributed to the unique optical properties of the AuNPs and AgNPs, contained within the glass, in a colloidal dispersion.[34]

Figure 1.4: The Lycurgus cup appearing red in transmitted light (left) and as green in reflected light (right). Image reproduced with permission from © Trustees of the British Museum.

In 1857, Michael Faraday, the renowned chemist, and physicist, established that individual AuNPs behave differently compared to their bulk form. He synthesised the first pure colloidal gold solution by the reduction of an

aqueous solution of chloroaurate ($AuCl_4^-$), and this was published in his work titled 'Experimental Relations of Gold (and Other Metals) to light.'[35]

In the interest of this research work, the focus will be on applications of metallic NPs in disease therapy. However, it should be noted that the unique chemical and physical properties of metallic NPs have allowed for their application across many other research interests such as bio-sensing,[36] electronics[37], and environmental remediation.[38]

1.2.2 Synthesis of Gold Nanoparticles

In the last few decades, a variety of routes have been presented for the synthesis of metallic NPs, such as electrochemical,[39] photochemical[40] and solution-based syntheses.[41] A prime focus on solution-based synthesis approaches has allowed the development of methods which control nanoparticle parameters such as size, shape and surface functionalities.[42]

The most common method of AuNP synthesis known as the Turkevitch method was published by John Turkevitch in 1951.[43] Commonly known as the citrate reduction method, this approach utilises citrate as both the reducing and capping agent in an aqueous system. Frens *et al.* refined this method in 1973, to demonstrate that by varying the ratio between the gold salt and reducing and stabilising agent (i.e the citrate to gold ratio), the size of AuNPs could be effectively tuned to between 15 and 150 nm.[44,45] Following on from this, the Brust-Schiffrin method was published in 1994, which has since been one of the most cited papers in *Chemical Communications*.[46] Brust *et al*. took inspiration from Faraday's two-phase system, which produced thiol stabilised NPs with average diameters below 5 nm.[47]

In light of all these methods, the Turkevich method has always remained the 'gold standard' method of synthesis. The only downside to this method is NP polydispersity above dimensions of ~50 nm. To reduce this, many have

navigated towards a 'seeding' approach, whereby seeds of ~15 nm are prepared, subsequently followed by the reduction of Au onto their surface, yielding monodispersed colloidal solutions with average dimensions up to 200 nm.[48]

Generally, noble metal NPs are the most readily used particles by researchers, due to their unique chemical and optical properties, in addition to their stability and ease of preparation. AuNPs are considered advantageous to biological applications, due to their non-cytotoxic capabilities, a reason for their preference over AgNPs. However, the key property of metallic NPs exists with localised surface plasmon resonance (LSPR). This is the phenomenon that arises when light interacts with the nanoparticle.

1.2.3 Surface Plasmon Resonance

Resident electrons on the surface of an NP are referred to as plasmons when they collectively oscillate.[49] Upon the interaction of an electromagnetic wave with an NPs surface, collective oscillations of the free conductive band electrons occur, a phenomenon known as surface plasmon resonance (SPR).[50] As the light wave passes through the NP, the electron density in the NP is polarised and oscillates in resonance with the frequency of the interacted light. This effect is termed localised surface plasmon resonance (LSPR) when confined to particles on the nanoscale.[51] The LSPR is characterised by a resonance band in the excitation spectrum (the combination of absorption and scattering) of the NP. Gustav Mie was the first person to describe the LSPR phenomenon in 1908 when he applied Maxwell's equation to spherical nanoparticles.[52,53] His reports specified that the plasmon band was a result of the dipole oscillations of the free electrons in the conduction band, which is today known as the explanation for SPR. A

schematic illustrating light interacting with a spherical metallic NP is shown in Figure 1.5.
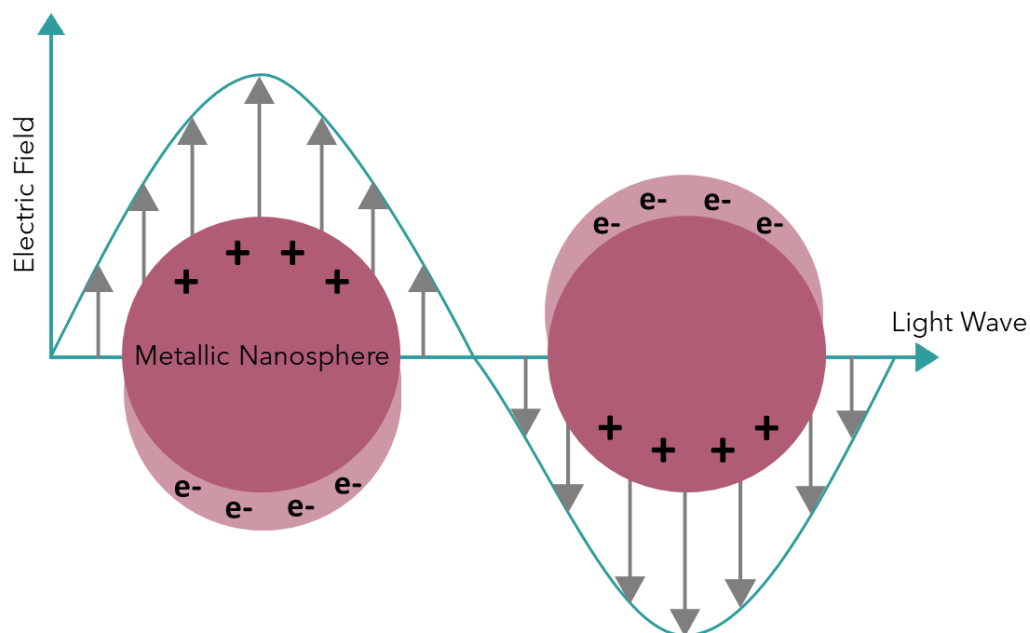
Figure 1.5: Illustration of the LSPR phenomenon, in which the electromagnetic light interacts with metallic, spherical nanoparticles, inducing collective oscillations of the conductance band electrons.

Monodispersed, 50 nm spherical AuNPs will give one band in the region of ~520 nm.[54] This, however, is subject to change depending on various factors such as choice of core metal, particle size, shape, and the surrounding dielectric medium.[55] Generally, an increase in the NP diameter will result in a bathochromic shift of the LSPR.[56] As the morphology of the NP deviates away from the typical spherical shape, such as stars and HGNs, this can have a pronounced effect on the LSPR, shifting it closer to or into the NIR region.[57-59] Such shapes also possess the characteristic of LSPR tuning by effectively adjusting the ratios of key components during the synthesis. Greater insight into tuning of the HGNs LSPR is provided in Chapter 4 of this thesis. Changes in the dielectric constant of the NPs surrounding environment can induce LSPR changes also, for example, due to surface modifications.[60] Finally, the

core metal can drastically affect the LSPR, and a clear example of this is the difference in LSPR between AgNPs and AuNPs. 50 nm AgNPs typically have extinction maxima at ~420 nm, and 50 nm AuNPs are ~520 nm.[61,62]

A unique characteristic of a NPs LSPR is its ability to shift which is extremely beneficial in many applications. For example, when two nanoparticles come into close proximity with one another, the surface plasmons couple resulting in a bathochromic shift of the excitation wavelength. This shift is towards longer, lower energy wavelengths, more commonly known as the 'red-shift.' This phenomenon was first exhibited by Mirkin *et al.,* who looked at assembling nanoparticles into aggregates using complementary oligonucleotides. This was a reversible process and LSPR changes were detected using extinction spectroscopy.[63] Similarly, a 'blue-shift' is observed when the LSPR tends towards higher energy wavelengths, known as a hypsochromic shift.[64] This reduced inter-particle distance results in signal enhancement and is exploited in SERS and will be explained in greater detail in section 1.4.4. It can also be particularly useful in determining the extent of aggregation in colloidal solutions and confirmation of surface modifications as will be seen in subsequent chapters.

1.3 Nanomedicine

Nanoparticles incorporated with studies in medicine have revolutionised areas of disease diagnostics and therapy. Since the start of the century, the number of publications have increased rapidly with many efforts to also navigate towards commercialisation. This is evident from the 6.8 fold increase in publications from 2005 to 2016[65,66] and is also representative of the interest and need for nanomedical research.

Nanomedicine has the potential to overcome the limitations of current conventional therapies such as surgery, chemotherapy and radiation. Issues

such as harmful side effects and poor biodistribution can be minimised by introducing localised NP treatment, with methods such as photothermal therapy and targeted drug delivery. The first case in nanomedicine to attain clinical success was the nanoparticle drug, Doxil®.[67] FDA (Food and Drugs Administration) approved doxorubicin, encapsulated within a liposomal coating to create a drug delivery NP, in treating Kaposi's sarcoma, ovarian cancer, metastatic breast cancer and multiple myeloma.[68]

NPs are extremely versatile as they can undergo surface modifications with a plethora of molecules/biomolecules, such as shown in Figure 1.6. Various methods of anchoring these moieties to the NP surface exist: thiol modifications can aid in adhering molecules such as DNA and drug molecules to the surface,[69] polyethylene glycol (PEG) linkers can become a medium for antibody attachment,[70] and electrostatic interactions also act as a method of addition for various proteins, dependent upon the charge of the NP surface and the protein.[71] It is clear why NPs have received much attention as nanomedical agents. Longer circulation times, greater permeability and disease specific biomarker modifications are some advantageous properties, which have led to many research outputs. Specifically, AuNPs have received much attention due to their non-cytotoxic capability, allowing for applications in the majority, if not all, of *in vivo* studies.[30]

Although nanomedicine research is focussed on all disease conditions, much attention is now fixated on CVD due to it reigning in the lives of a high percentage of the population.
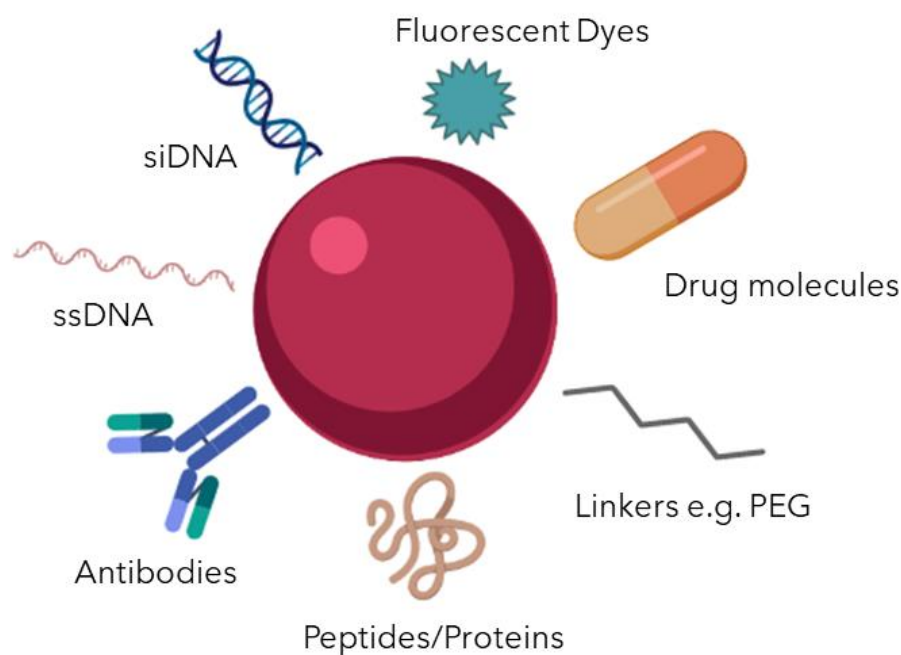
Figure 1.6: A schematic representing nanoparticle functionalisation with varying molecules/biomolecules which can be used for targeting, therapy, shielding and detection.

1.3.1 Nanomedicine in Cardiovascular Disease

The focus on CVD, from the nanomedical point of view, has been extremely advantageous, as can be seen with the library of reviews talking about progression within the field.[66,72] In a review by McCarthy *et al*., they remark that atherosclerosis, from all CVD syndromes, is the most popular in terms of nanomedicine research due to the high number of consequential outcomes from this condition.[73] In the cascade of atherosclerotic events, there come forth many biomarkers and biomolecules, which can be used as detection/therapeutic agents for selective targeting of CVD.

Amongst the plethora of examples, vascular inflammatory biomarkers have been targeted using antibody functionalised nanoparticles, in the novel work of Noonan *et al*. They took a multiplexed approach to target the adhesion molecules: ICAM-1, VCAM-1, and P-selectin using surface enhanced Raman scattering (SERS), successfully detecting all three

biomarkers *in vivo* with mice. This was the first case of applying a SERS multiplexing approach to atherosclerosis, propitiously demonstrating that functionalised nanoparticles combined with SERS imaging could be advantageous in the non-invasive, simultaneous detection of inflammation biomarkers. This suggests that Raman spectroscopy could address unmet clinical needs in CVD.[74] Other molecules such as DNA, peptides[75], and polymers,[76] have also been utilised to direct nanoparticles to the tumour site, highlighting the versatility of metallic nanoparticles as detection and therapeutic agents for CVD.

Recently, nanoparticles are being appreciated as photothermal agents, due to their commendable ability to ablate surrounding tomourous cells at selected sites of damage.

1.3.2 Photothermal Therapy

The conversion of light into heat is known as the photothermal effect. Upon the interaction of incident photons with metallic nanoparticles, the energy is absorbed and converted to heat, subsequently dissipating to the surrounding environment.[77] If applied *in vivo*, the local environment is more often tumorous cells, which can be thermally destroyed. This effect is termed photothermal therapy and became popular in the 1960s when it was first used for tumour eradication.[78] Today, it's widely used across many areas of medicine such as ophthalmology,[79] gynecology[80] and orthopaedic surgery.[81]

Photothermal agents are not restricted to metallic NPs, however, in the interest of this thesis, NP will be the sole focus. Their appeal is attributed to the enhanced absorption they experience in the NIR due to their LSPR. This is referred to as plasmonic photothermal therapy (PPTT). El-Sayed and his group have an extensive bank of publications for using various gold nanostructures with PTT, taking a closer look at the process by which the

light to heat conversion takes place through the use of nanoparticles. Using the medium of time-resolved transient absorption spectroscopy, they have detailed a series of photophysical processes which take place as described below in Figure 1.7.[78,82-84]

Electron Thermalisation	•Incident photons excite electrons on the surface of the metallic nanoparticle, producing hot electrons which can reach temperatures of ~1000 K.
Lattice Formation	•Energy exchange occurs between the hot electrons and lattice. •Electron-electron and electron-phonon processes, occuring on femto-seconds and picoseconds, respectively, allowing for the formation of a hot metallic lattice.
Lattice Cooling	•The lattice cools through the process of phonon-phonon relaxation, subsequently transferring it's heat to the surroundings. •This occurs on orders of several hundreds of picoseconds.

Figure 1.7: A summary of the steps involved within the photothermal effect; whereby light energy is converted to heat energy.

PTT has been extensively used for cancer therapy attributed to the low thermal tolerance of cancerous cells, making it slightly easier to ablate such cells.[78] Although the first case of using lasers to ablate an atherosclerotic plaque was carried out in 1963 by McGuff *et al.*,[85] only recently are researchers beginning to apply PTT to CVD. This is with the belief that greater challenges lie with CVD nanomedicine in comparison to cancer.[86]

PTT-CVD has not only come as an alternative approach to current conventional techniques but is trialing to bridge diagnosis and therapeutics, by taking on a theranostic approach. For example, Yeager *et al.* used silica-coated gold nanorods as photothermal agents to identify plaque progression, simultaneously heating tissue using a continuous wave near-infrared illumination. Detection and monitoring of the process were carried out using intravascular ultrasound and photoacoustic (IVUS/IVPA), which are current clinical imaging techniques for atherosclerosis.[87] It is understood that PPTT, combined with current techniques, is making efforts to by-pass current clinical boundaries. The most remarkable case saw the first-in-man trial using PPTT to target atherosclerotic lesions.[26] One set of patients received a bio-engineered on-artery patch of silica-gold NPs, which was implanted using a minimally invasive cardiac surgery, and the other group had silica-gold iron NPs delivered to the artery via a micro-catheter. These two approaches to nanoparticle delivery saw the regression of atheroma plaque, meeting clinical levels of safety and efficacy.

Such examples are reassurance that PPTT is effective for CVD, and although still in its infancy, has great potential for the future. With this in mind, this work had a particular emphasis on using PPTT with functionalised cholesterol DNA nanoparticles, in contributing to the developments of PTT-CVD. A general schematic depicting the phenomena of PPTT in humans is depicted in Figure 1.8. Here, nanoparticles are shown to be intravenously injected into the body, and once at the site of interest, they are irradiated with a laser, which typically has a NIR wavelength. This schematic is not based on one particular study and is provided for visualisation purposes of this phenomenon.
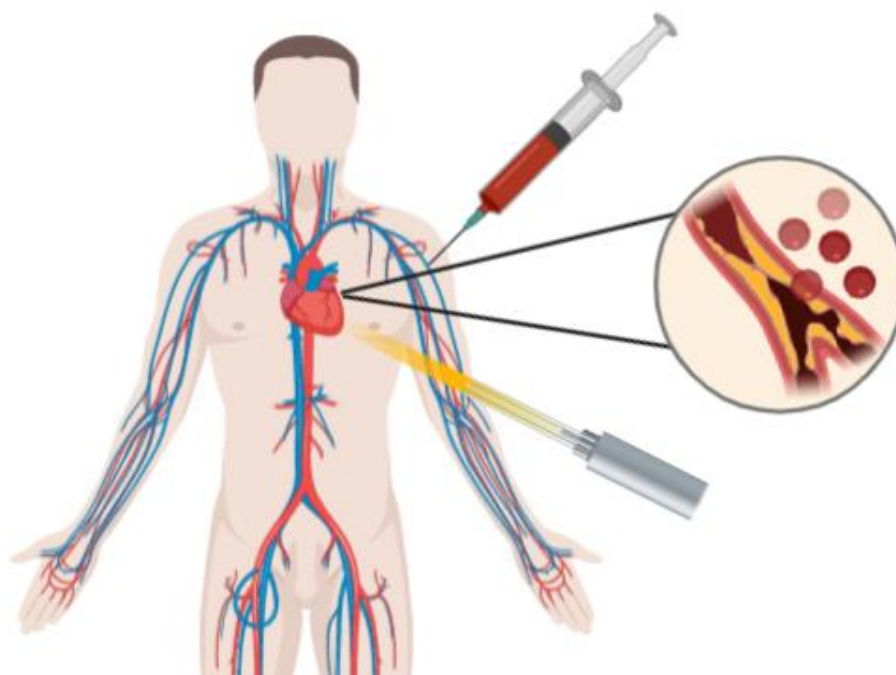
Figure 1.8: Illustration depicting PPTT in which nanoparticles are intravenously injected into the human body, and upon accumulation at the site of interest, can be irradiated with a NIR laser, which will in turn ablate surrounding cells. Schematic provided for visualisation purpose and is not the basis of one particular experiment.

Prior to PPTT experiments in this work, it was essential to deduce the uptake of the modified NPs *in vitro*. For this purpose, 2D and 3D Raman mapping was utilised.

1.4 Raman Spectroscopy

When light interacts with matter, it is either, absorbed, emitted or scattered. Spectroscopy is used to identify these interactions and provides us with information on the molecular structure in question. Raman spectroscopy is a technique focussed on the study of scattered light from molecules, specifically, the inelastic scattering of light.[88]

Today, Raman spectroscopy has become increasingly popular due to its ability to provide a unique fingerprint spectrum for molecules, together with producing qualitative and quantitative information. Over the years the technique has seen advancements such as SERS and stimulated Raman spectroscopy (SRS). These have greatly improved the Raman signal together with the imaging speed allowing for the compilation of intricate information at the cellular level. The techniques have been revolutionary in areas of disease diagnostics,[89] drug development[90] and environmental sciences.[91,92]

1.4.1 The History of Raman Spectroscopy

The theory of Raman was first postulated by Adolf Smekel in 1923.[93] It was Professor Chandrasekhara Venkata Raman and his student, Kariamanickam Srinivasa, who were the first to demonstrate this experimentally in 1928.[94] In this experiment, the professor and his student used sunlight as the source of light, a pocket-sized spectroscope and the human eye as the detector. This experiment was a demonstration of scattered radiation of a different frequency to the incident light being detected, confirming their hypothesis and forming the basis for Raman spectroscopy. This discovery led to Professor Raman receiving the Noble Prize in Physics in 1930.[95]

1.4.2 Principles of Raman Spectroscopy

When a photon of light interacts with a molecule, the photon is either absorbed, scattered or penetrates through the molecule without any interaction.[88] In the case where the energy of the incident photon equates to the energy gap between the ground state and excited state of a molecule, the photon may be absorbed, resulting in the molecule being promoted to a higher excited energy state. In another case, the photon of light may interact with the molecule and scatter. As light interacts with a molecule, it distorts the cloud of electrons around the nuclei, forming short-lived virtual

energy states. These states are not stable, allowing the photon to re-radiate rapidly by scattering.[88]

The most common form of scattering is Rayleigh scattering, an elastic process by which the electron cloud is distorted but without any disruption to the nucleus. As a result, light is scattered at the same frequency as that of the incident light. However, 1 in every 10^6-10^8 photons is in-elastically scattered,[88] therefore resulting in a change in frequency of the scattered light by one vibrational unit of energy compared to the incident light. This is Raman scattering and occurs due to nuclear motion. Raman scattering can be sub-categorised, depending on whether energy is transferred from the incident photon to the molecule (Stokes scattering) or from the molecule to the scattered photon (anti-Stokes scattering).[96] Most commonly a Jablonski diagram is used to illustrate the processes of Rayleigh and Raman scattering, as shown in Figure 1.9.
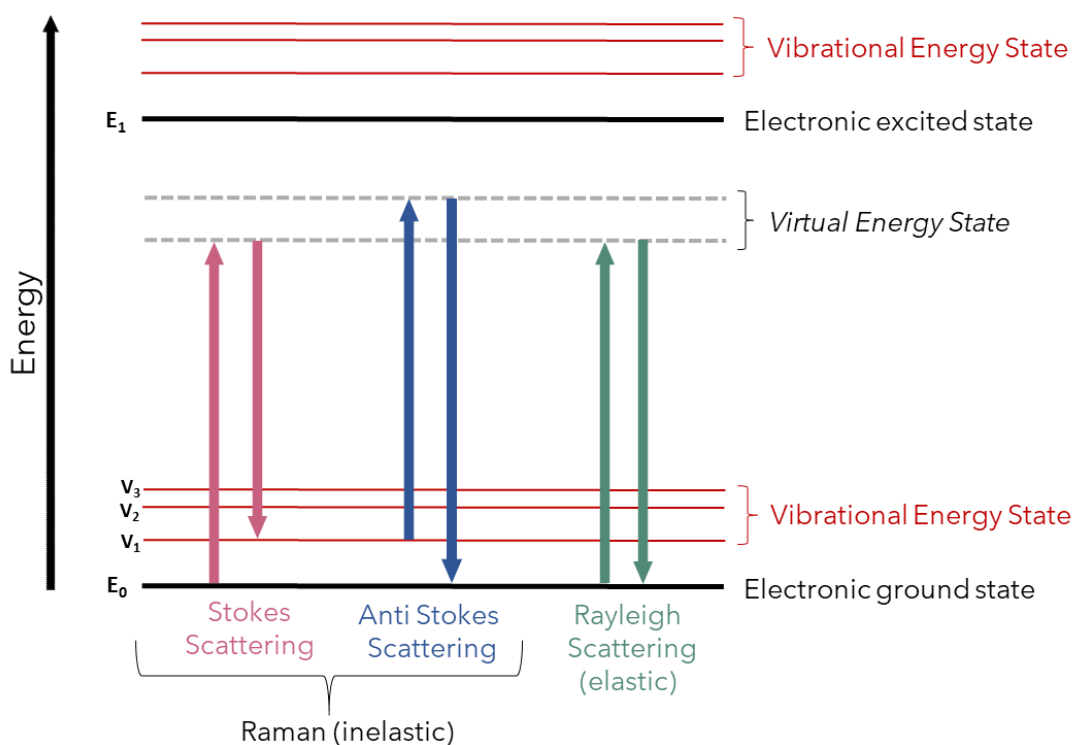
Figure 1.9: Illustration of a Jablonski diagram, which is typically used to show the variance in the processes of Rayleigh, Stokes and anti-Stokes scattering.

Stokes scattering involves the photons being scattered with lower energy than the incident photons. This is due to the molecules returning to an excited vibrational state, which is higher in energy than the ground vibrational state. At higher temperatures, there will be a greater number of molecules present in the excited vibrational state, which relax to the ground vibrational state when irradiated. This is anti-Stokes scattering, however, is the weaker of the two as at room temperature molecules will primarily be resident in the ground vibrational state. Hence, stokes scattering is greater in intensity. The ratio of intensities of Stokes and anti-Stokes scattering can be predicted using the Boltzmann equation:

$$\frac{N_n}{N_m} = \frac{g_n}{g_m} \exp\left[\frac{-(E_n - E_m)}{kT}\right]$$

Equation 1: The Boltzmann Equation

Where N_m and N_n are the number of molecules in the ground vibrational level and excited vibrational level respectively, g is the degeneracy of the m and n energy levels, k is the Boltzmann constant (1.3807×10^{-23} J K^{-1}), T is the temperature in kelvin (K) and E_n – E_m is the energy difference between the vibrational energy levels E_n and E_m.[88]

It should also be noted that the intensity of the scattering can be predicted using Equation 2.

$$I = KI_L\alpha^2v^4$$

Equation 2

Where I is the Raman intensity, K is a constant, I_L is the laser power the sample is exposed to, α is the polarizability and v is the frequency of the incident radiation. The intensity is proportional to the fourth power of the frequency, hence, improvements to the Raman intensity can be made by using shorter excitation wavelengths with a higher frequency, and also by increasing the laser power.[88] However, such adjustments can damage samples. This issue can be addressed by utilising resonance Raman scattering (RRS) and SERS. These techniques are also able to enhance signals comparatively to conventional Raman scattering.

1.4.3 Resonance Raman Scattering

To intensify the Raman scattering, the frequency of the laser beam can be matched with that of an electronic transition in a molecule. This is known as RRS and the difference between this and conventional Raman scattering is that, in the former, the absorption of photon results in the excitation of a molecule to a vibrational energy state within the first excited state, whereas in the latter, the excitation of a molecule is to a virtual energy state.[97] Therefore, with RRS, signal enhancements of 10^3-10^4 can commonly be observed with maximum intensity being up to 10^6.[88] An example of the use of RRS is in the study of heme-containing proteins.[88] A Jablonski diagram depicting the difference between Raman stokes scattering and resonance Raman stokes scattering can be seen in Figure 1.10.
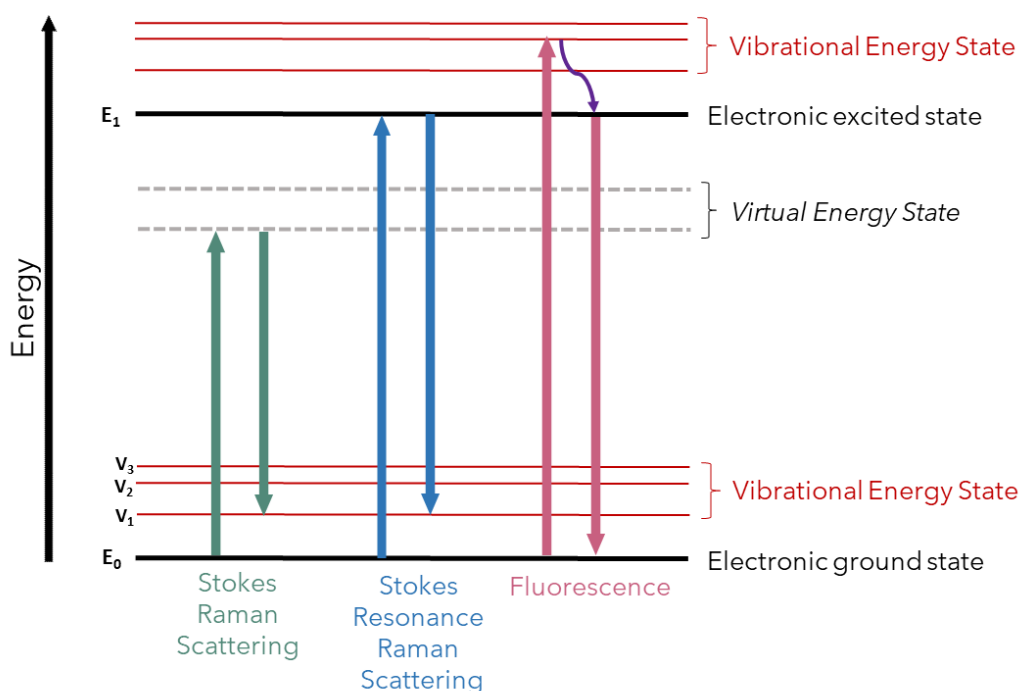
Figure 1.10: A Jablonski diagram showing the difference in stokes Raman scattering and stokes resonance Raman scattering. The difference between these and fluorescence is also illustrated.

RRS does, however, come with its limitation. The main disadvantage is that it competes with fluorescence processes resulting in the emergence of a high fluorescence background.[97] Fluorescence is the process by which a molecule is promoted to a high energy vibrational state of the first excited energy state. However, it slowly relaxes to the ground vibrational state of the first excited state (Figure 1.10). The one advantage is that the timescale these processes occur on are different, with Raman occurring over picoseconds and fluorescence over nanoseconds.

Fluorescence can obscure Raman signals, however, can be limited with the use of pulsed lasers or using a longer wavelength excitation source. Another step is to incorporate metallic nanoparticles with Raman spectroscopy, which can quench fluorescence and also enhance the Raman signals.

1.4.4 Surface Enhanced Raman Scattering

This technique was first observed in 1974, by Fleischmann and co-workers, who observed SERS when pyridine was adsorbed onto a roughened silver electrode.[98] This produced an intense signal, which was initially thought to be due to the increased surface area, consequential from the roughening process, allowing for more pyridine molecules to be adsorbed onto the surface. However, two separate research groups believed that signal enhancements of 10^6 could not be due to the increased surface area alone, disputing this theory in 1977. Jeanmarie and Van Duyne proposed that the enhancement was due to the electromagnetic effect,[99] opposingly Albrecht and Creighton believed that the enhancement came from the charge transfer effect.[100]

Today, the SERS phenomenon is conditioned on two effects: electromagnetic and chemical enhancement, with the former being considered as the dominant one. The electromagnetic enhancement is thought to occur due to the interaction between the oscillating electrons on the metallic surface (LSPR) with the adsorbed molecule. Subsequently, the local field experienced by the analyte adsorbed onto the surface is increased. Perpendicular oscillations are achieved through roughening the surface which is vital to observe scattering. With increased polarisation around the molecule, the Raman signal increases.[101] The enhancement effect is not uniform around every nanoparticle and is greater when nanoparticles are in close proximity to one another, i.e. coupling or clustering.[88,102] There may also be extremely active parts of an NP surface, termed 'hot spots' which result in strong SERS signals.[88]

The second effect is thought to be inferior but is still reasoned to contribute to the SERS effect. Known as the chemical enhancement or as a charge transfer, here, the analyte is held closely to the metal surface through the formation of a bond. As a result, a charge transfer occurs either from the analyte to the metal surface or vice versa. Consequently, there is a rise in the

polarizability of the molecule, therefore increasing the Raman signal. This is reasoned to be due to new electronic states arising from the bond formation between the metal surface and the analyte, which resonate with the laser excitation wavelength.[103,104]

Although there are deliberations that SERS is attributed to either one of the effects, many scientific researchers are of the belief that SERS occurs as a result of the combination of electromagnetic and chemical enhancement. Lombardi *et al.* presented a 'unified expression' to the SERS phenomenon, addressing the third contribution to this technique, which was shown to be due to resonances from the analyte itself. By providing an expression incorporating the three contributions, they posed that each contribution could not be considered independently as a factor to the SERS enhancement, and further provided an approach to experimentally determine the degree of contribution each possessed.[105]

Many metals can be used as SERS substrates, such as gold,[106] silver,[107] copper[108] and aluminium.[109] However, gold and silver are predominantly used due to their stability and the fact that their LSPR's lie in the visible region of the electromagnetic spectrum, therefore suitable with the visible and NIR laser systems commonly used for Raman spectroscopy.

Since the development of SERS, it has become widely applied in various areas of interest, evidently witnessed from the short history yet thousands of research publications. In specific, one area which has greatly benefited from SERS is disease diagnostics and therapy. Researchers have increased and amplified publications on the detection of numerous biomarkers for various cancers, infections, and disease state, monitoring their presence and progression rates. Specifically, for CVD, Mabbott *et al.* looked at the detection of miRNA through the use of 3D microfluidic devices and SERS for CVD. Here, the quantitative nature of SERS was highlighted by following the intensity of the SERS signal. By using a portable Raman spectrometer, their work enhanced the vision of Raman spectroscopy becoming part of the

point of care (POC) testing in the future.[110] Similarly, Chon *et al.* reported a competitive SERS-based immunoassay for the detection of two cardiac biomarkers, troponin I (cTnI) and isoenzyme MB of creatine kinase (CK-MB).[111] In other areas of interest, Kearns *et al.* were able to successfully detect multiple food pathogens through multiplexing, a technique whereby molecules/biomolecules can be isolated from a mixture and simultaneously detected. Three sets of biorecognition nanoparticles were prepared, each with strain-specific antibodies, and each with a distinctive Raman dye. Detection of the Raman band confirmed the presence of the bacterial pathogen. Their work, again, highlighting the rapid and ultra-sensitive nature of SERS for the detection of biological components. Multiplexing is a key characteristic of SERS, which techniques such a fluorescence cannot achieve.[112] This multiplexing approach has also been extended to *in vivo*, where the simultaneous detection of co-cultured cell lines was possible with functionalised NPs, which targeted epidermal growth factor receptors (EGFR) and the HER2 biomarker expressed in cancer cells.[113] In other areas of study, Milligan *et al.* were able to use SERS to detect various nitroaromatic explosive molecules simultaneously through the detection of a coloured Janowsky complex.[114]

Such examples have shown SERS as rapidly becoming an increasingly used technique in various fields of interest and paving the way forward as a sensitive, practical and efficient mode of detection. These points are reiterated time and again in the many reviews published on SERS and it's thriving future.[115-117]

1.4.5 Surface Enhanced Resonance Raman Scattering

The technique of surface enhanced resonance Raman scattering (SERRS) was first reported by Stacey and Van Duyne in 1983,[118] which effectively combines the surface enhancement of SERS with the molecular resonance enhancement of RRS. SERRS refers to enhancements generated by an analyte possessing a chromophore, with an absorbance maximum in resonance with the laser excitation wavelength. Resultingly, this technique has increased the sensitivity of Raman scattering, providing enhancement signals up to 10^{14},[88] a ten-time fold increase in comparison to conventional Raman scattering. A common SERRS reporter is malachite green isothiocyanate (MGITC), which is typically used with a 633 nm laser excitation.[119] For example, the work of Barrett *et al.* saw the functionalisation of MGITC onto oligonucleotide-AuNPs for enhanced stability. The SERS of the conjugates were reported using a 633 nm laser excitation.[120]

A key advantage of SERRS is its ability to quench fluorescence signals obtained from the sample, thus allowing a plethora of resonant molecules to be used as SERRS analytes, regardless of possessing fluorescent/non-fluorescent characteristics. Additionally, lower laser powers and shorter accumulation times can be utilised, allowing surface photodecomposition to be of a minor issue.

1.4.6 An Insight into Raman Imaging

In the current research, Raman imaging is becoming increasingly popular, attributed to the superior laser microscopes we have today. This technique can produce false colour images from the Raman spectrum of a sample, typically cells, bacteria, tissue, etc (Figure 1.11). A pre-selected area allows for the collection of a spectrum at each pixel. From this data, many analyses can be carried out, such as direct classical least squares (DCLS), which is desirable for SERS as it can follow a dye spectrum in a cell. Generally, after

mapping, the unknown data is fitted to the reference spectrum of a Raman dye and a good spectral fit is plotted as a false colour image. Another option is to monitor the distribution of the intensity of a specific vibration. This technique was exploited in the work of Jamieson *et al.,* in which they investigated three different fatty acids with alkyne tags and their intracellular uptake. They exhibited their results by false colour maps, highlighting the intensity of the 2118 cm^{-1} alkyne band.[121]

This approach has allowed Raman spectroscopy to make the transition into the clinical setting. Since the first confocal Raman microscope, in 1990, which was used to study single cells and chromosomes, Raman imaging has become a common technique to study cellular dynamics.[122] A review by Smith *et al.,* discussed the link between Raman imaging and cellular studies, mentioning this technique overcoming the limitations of current techniques and becoming a 'routine tool' in assessing the cellular environments.[123] These recent advancements have paved the way for live cell mapping and 3D cell mapping to be carried out, techniques which will be utilised in the work presented here. Generally, live cell mapping is an appreciable technique utilised for observing living cells in their physiological conditions.[123] On the other hand, 3D Raman mapping is ideal for studying the biochemical composition for single cells or tissue cross-sections.[124] An enhanced insight on these techniques will be presented in Chapter 3.
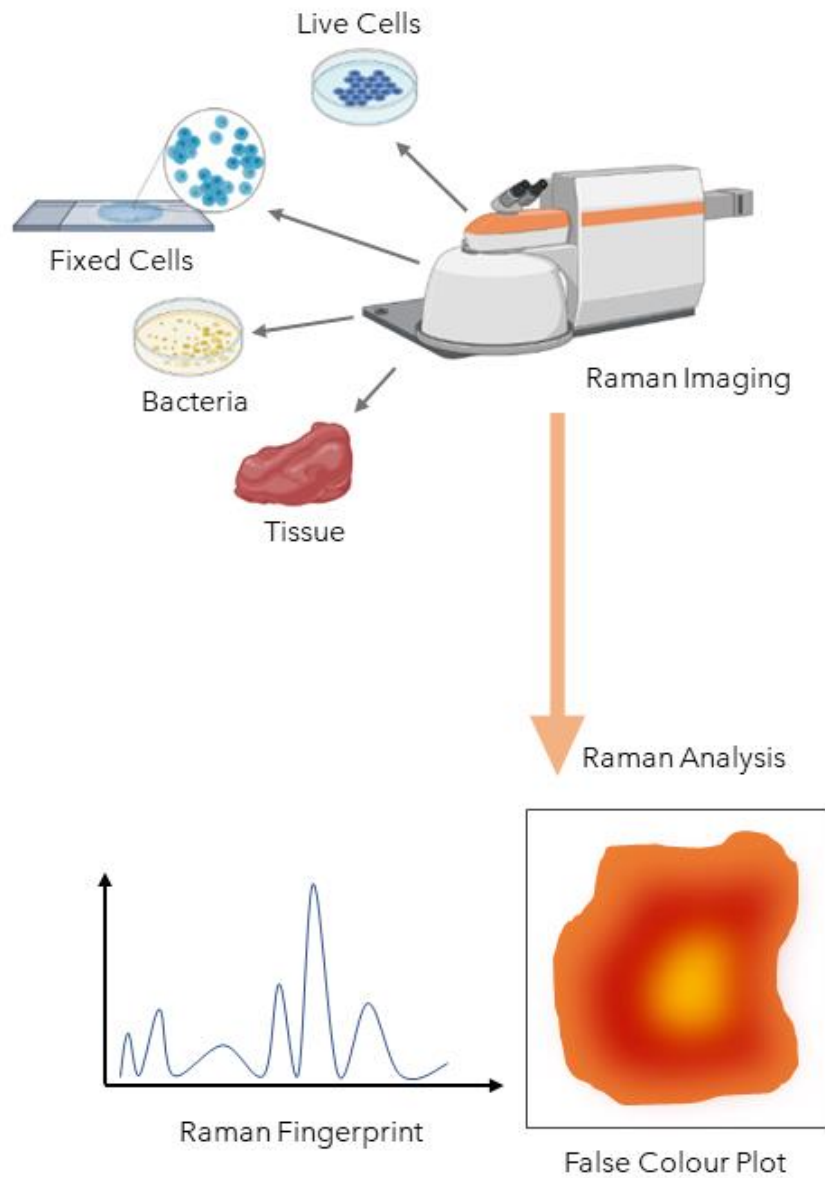
Figure 1.11: Schematic illustrating the technique of Raman imaging using a confocal Raman spectrometer, which can be used for analysis of live/fixed cells, bacteria and tissue. The Raman/dye fingerprint can be analysed post mapping or false colour plots can be constructed using specialised software.

2. Research Aims

The focus of this research was to determine the cellular uptake of AuNPs with cholesterol modifications, and whether these could become potential agents for photothermal therapy. The research was broken down into three main sections, in which, firstly the focus was on developing stable cholesterol modified nanoparticles, following on with *in vitro* studies in the second section, to determine their interactions with cells, in specific endothelial cells. And finally, the last area of study focussed on trying to design suitable photothermal agents for CVD, using cholesterol modifications. The specific aims of each study are given below:

I. Chapter 3 (sub-section I): This section focused on the method of cholesterol attachment to nanoparticles, in which the route of DNA functionalisation was chosen. A series of analyses to determine successful functionalisation included: extinction spectroscopy, dynamic light scattering and SERS measurements. The stability of these conjugates was also studied.

II. Chapter 3 (sub-section II): Here, the aim was to investigate cholesterol modified nanoparticles *in vitro*. Studies were carried out with two cell lines. RAWs (macrophages) determine the uptake of cholesterol modified nanoparticles, and HUVECs are used to outline whether the uptake of these probes is greater in endothelial cells. 2D and 3D SERRS mapping were used for investigations, along with live cell mapping. A multiplexed approach was applied to determine the enhanced uptake of these

conjugates over the control. Cell viability studies also revealed the non-toxic nature of these modified nanoparticles.

III.   Chapter 4: Herein, HGNs were studied as the core for photothermal agents. Their tunable LSPR and heating capabilities were exploited. Subsequently, cholesterol was functionalised onto HGNs and their photothermal abilities to destruct cells were noted. 2D SERRS mapping was used to determine the uptake of these functionalised HGNs in HUVECs, and cell viability studies highlighted the non-cytotoxic behaviour of them.

3. Cholesterol Modified Nanoparticles

3.1 Functionalisation of Cholesterol Modified Nanoparticles

3.1.1 Sub-Chapter Introduction

Decorating inorganic nanoparticles with DNA molecules has become common in nanotechnology today. The concept was first introduced by the groups of Mirkin and Alivisatos in their pioneering works in 1996.[125] Mirkin *et al.* attached thiol modified DNA to 13 nm AuNPs,[63] and Alivisatos *et al*. had a similar approach where they functionalised thiolated oligonucleotides to 1.4 nm nanocrystals, both approaches for assembling AuNPs into aggregates.[126] These essential 'proof of concept' studies paved the way and today, nanoparticles can be coated with varying nucleic acid moieties such as ssDNA and dsDNA[127] for usability in drug delivery,[128] gene regulation,[129] and photothermal therapies.[130,131] DNA strands can themselves can be modified with various hydrophobic/hydrophilic groups, fluorescent dyes, and linker molecules, to name a few amongst the plethora of possible attachments. The work herein, utilised DNA functionalisation as a means of attaching a cholesterol group to the NP surface.

Lipid modifications on nucleic acids are not uncommon. Primarily, these modifications are used to strengthen cellular interactions. DNA itself cannot diffuse through the cell membrane as its hydrophilic and anionic character has a poor affinity for the hydrophilic exterior of the phospholipid membrane (Figure 3.1). Therefore, hydrophobic moieties such as cholesterol, squalene, or fatty acids are chemically conjugated onto oligonucleotides to improve the delivery of these biomolecules.[132] Lipids are advantageous as they can be used for both membrane binding[133-135] and for

also by-passing the cellular boundaries in some instances.[136] In the case of the former, lipid-modified DNA has been used for membrane scaffolds[137] and controlling membrane bending.[138] Recently, a study by Tian *et al.* was published in which they utilised cholesterol functionalised nanostars to anchor onto exosomes, which can be used as an indicator of cancer.[139] The cholesterol allowed for attachment to the exosome surface by hydrophobic interactions between cholesterol and lipid membranes. The latter, in which cholesterol is used for by-passing cell boundaries, is useful for drug delivery, disease detection etc.[140,141]
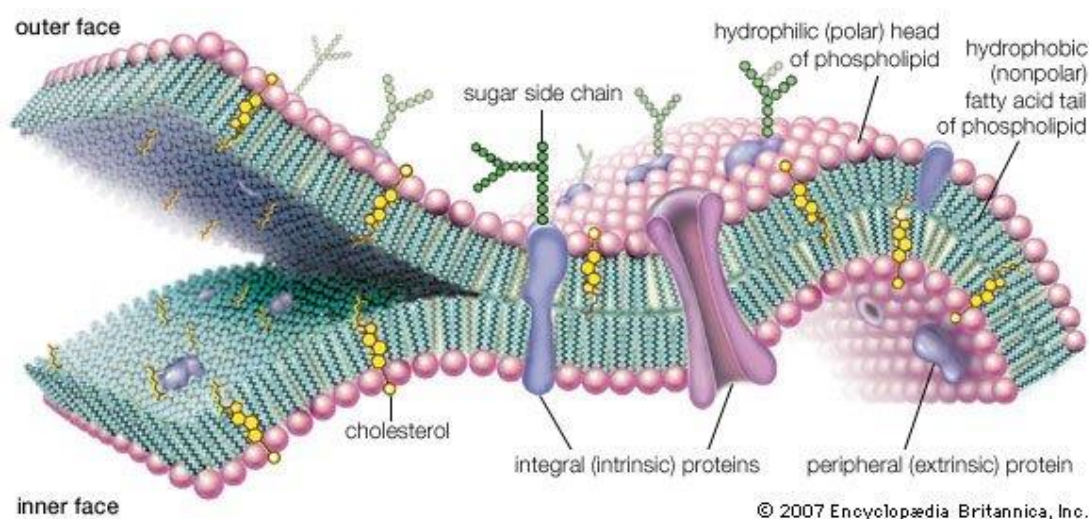
Figure 3.1: Pictorial representation of the cell membrane, consisting of cholesterol, various proteins and ion channels. Image reproduced with permission from Encyclopaedia Brittanica, Inc.

Cholesterol has received much attention as a useful lipid due to its biocompatibility. Its existence within the human body potentially means that the body does not screen it as a foreign substance. Covalently attached to the oligonucleotide, a cholesteryl-TEG (cholesteryl ester with a triethylene glycol group) anchor is found to incorporate well into lipid membranes, without disturbing the bilayer structure and dynamics.[133,142-144] Furthermore, this modification of cholesterol on DNA was found to not induce significant

condensation of the membrane lipids, in comparison to its counterpart – cholesterol.[143] Hence, this was the preferred modification of cholesterol onto an oligonucleotide. Cholesteryl-TEG was first investigated by Pfeiffer and Hook in their research, in which they used cholesteryl-TEG modified ssDNA for spontaneous anchoring into the hydrophobic core of the lipid membrane.[145] Later, groups such as Bunge *et al.* studied the lipid-modified oligonucleotides through various routes such as NMR and fluorescence methods, and concluded that this specific nucleic acid 'incorporates well into the lipid membranes without disturbing the bilayer structure and dynamics.'[143] From various research works, it is evident that cholesteryl-TEG can fit comfortably within the cell membrane itself. The uptake of these functionalities combined with AuNPs has not been extensively studied and it would be interesting to determine their role in cellular uptake and whether they can also be used as photothermal agents, as will be discussed in subsequent chapters. It should be noted that from here on cholesteryl-TEG-DNA is referred to as cholesterol-DNA (chol-DNA) for ease.

3.1.2 Chapter Aims

The focus of this chapter was to functionalise AuNPs with chol-DNA to create a synthetic 'fatty particle,' which would later be investigated within a cellular environment to determine whether these particles bind to the membrane itself or are able to by-pass it. Multiple factors were considered such as NP core size, DNA loading and the type of Raman active dye to be used. The addition of a hydrophobic moiety to the DNA can be challenging as its suspension is difficult, however, the presence of a surfactant can solve this issue. Here, Tween 20™ was used to aid the suspension of chol-DNA in solution at a low concentration, which would not be detrimental to cells. Finally, the short- and long-term stability was investigated through a set of stability studies, which included a continuous kinetic study subsequent upon

completion of the functionalisation procedure, and another one over three weeks. The stability of the conjugates was vital as for subsequent *in vitro* studies, these had to retain stability and it was important to investigate whether the cholesteryl moiety was retaining solubility or if it was beginning to aggregate.

3.1.3 Results and Discussion

3.1.3.1 Synthesis of Spherical Gold Nanoparticles

The preference of utilising AuNPs over AgNPs was attributed to the non-toxic nature of the former.[146-149] This was vital as the main goal was to introduce the modified nanoparticles into an *in vitro* setting, thus mandatory that the particles do not cause cell death. Spherical AuNPs were the 'core' of the fatty nanoparticles, synthesised using a modification of the Turkevich method. The reaction proceeded with the reduction of Au^{3+} to Au^0 by citrate salt, which fulfilled the role of both the reducing and capping agent. The overall negative surface charge resulting from the citrate would allow for electrostatic repulsion between individual nanoparticles, therefore resulting in a monodispersed solution. Here, synthesis for 40 nm AuNPs were carried out as typically larger nanoparticles give enhanced SERS in comparison to smaller ones.[150] The resulting wine-red colloid was characterised using extinction spectroscopy, dynamic light scattering (DLS) and zeta measurements. The extinction spectrum is provided in Figure 3.2:
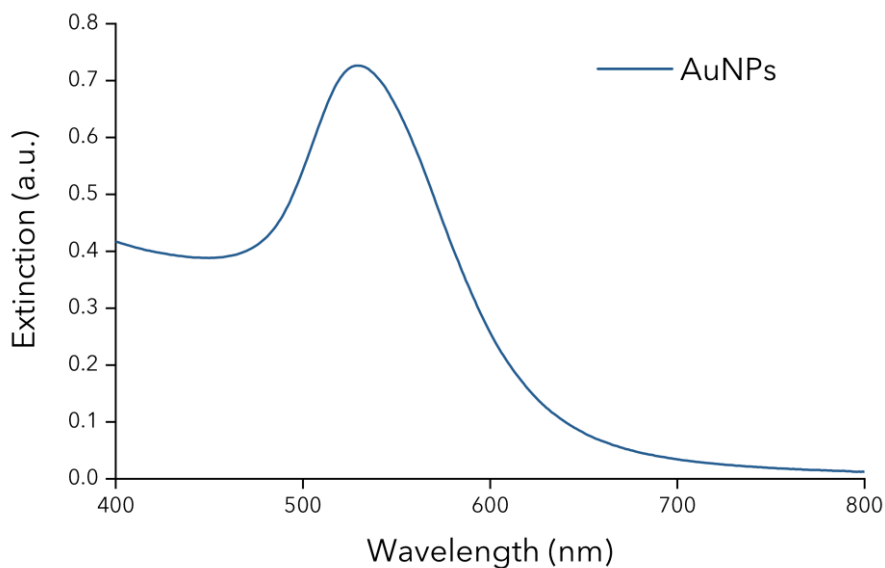
Figure 3.2: Extinction spectrum of bare AuNPs exhibiting a LSPR of 530 nm. Spectrum was collected using a scan rate of 600 nm/min and a 1 in 2 dilution was carried out prior to data analysis.

The extinction spectrum displayed the LSPR of AuNPs at 530 nm, which was anticipated for spherical gold with an average diameter of ~48 nm according to literature.[61] The fairly narrow band was indicative of a monodispersed colloidal solution, a key characteristic of the Turkevich method.[151] DLS measurements indicated the average diameter to be 51 ± 0.8 nm, which was a slight overestimation. The DLS measurement is the hydrodynamic diameter, including: the inorganic core, the coating material and the solvent layer as it moves under the influence of the Brownian motion.[152,153] Hence, DLS measurements can only be taken as an indicative size of the nanoparticles. It should also be noted that the '± 0.8' was the error associated with the acquired data and not correlated to the particle size distribution. For a more accurate representation, scanning electron microscopy (SEM) was carried out (Figure 3.3). In such a case, an electron beam is focused onto the sample, relaying an image gathered through the secondary/backscattered electrons.[154] This size data is considered more accurate as the metallic core is measured, in comparison to DLS, in which

case the hydrodynamic diameter is given. The SEM data was evidence that the majority of AuNPs were around the 40 nm mark, which was the intended size during synthesis.
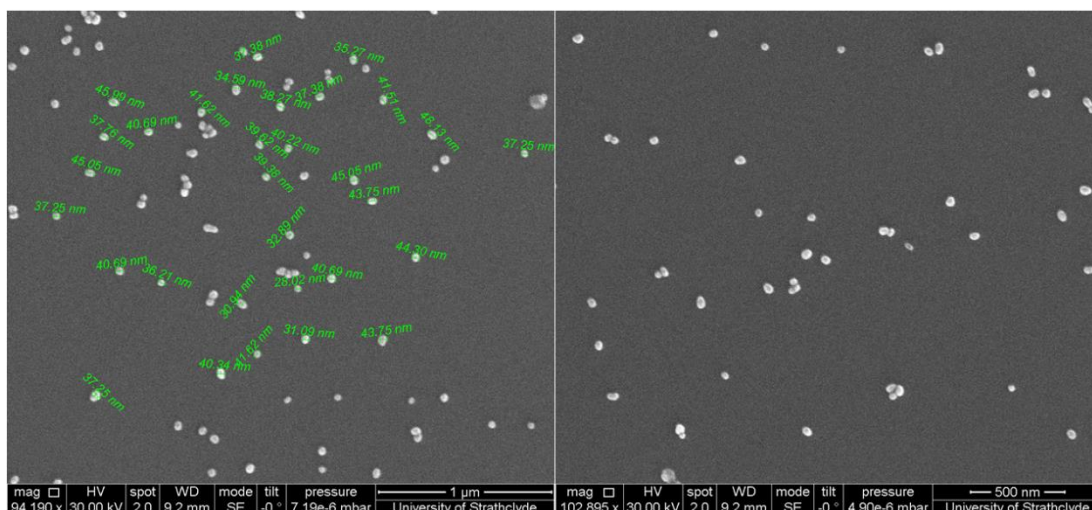
Figure 3.3: SEM images of bare AuNPs which display the majority of the AuNPs being between 37 – 45 nm.

The dispersity of the nanoparticles was accredited to the negative surface charge provided by the citrate ions, which allowed them to electrostatically repel one another and not form aggregated clusters. Zeta measurements display the surface charge of the colloidal solution, therefore determining the stability of the colloid also. The zeta potential for AuNPs was found to be -47.7 ± 8.9 mV. As the values tend towards increasing negative figures, the colloidal stability is increased with values by-passing -30 mV showing the greatest stability.[155] In the case here, the AuNPs were considered stable.

3.1.3.2 Cholesterol DNA Functionalisation

Two key components mandatory in the assembly of a 'fatty SERS nanoparticle' were: cholesterol and a Raman active dye. A facile route of functionalising cholesterol onto the nanoparticle surface was via the medium of DNA functionalisation. This route was preferred as it is relatively straightforward conjugating a cholesterol moiety onto ssDNA, and subsequently functionalised onto the nanoparticle surface via a thiol group. The dye was also pivotal as this would primarily be used to detect the functionalised AuNPs *in vitro*, helping to understand cellular uptake. In this study, malachite green isothiocyanate (MGITC) was chosen due to its strong scattering providing a characteristic, intense SERRS signal. A schematic of the functionalisation process which depicts the dye, MGITC, and chol-DNA functionalised to an AuNP is provided in Figure 3.4.
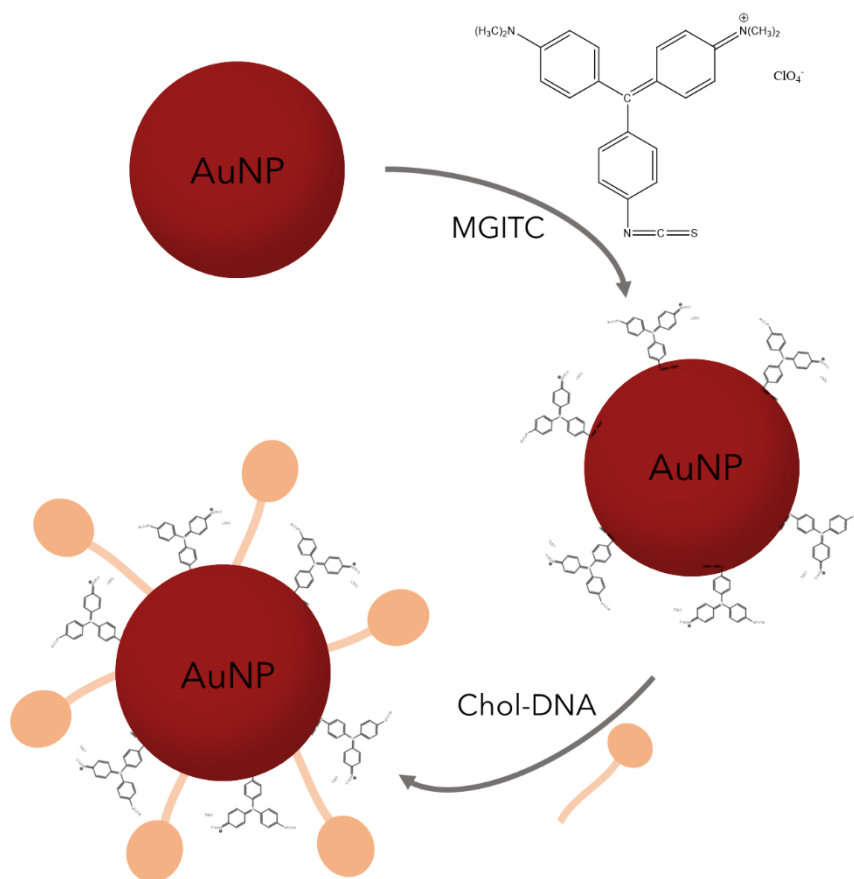
Figure 3.4: Schematic illustrating the step-by-step functionalisation of a Raman dye (MGITC) and chol-DNA onto the surface of a AuNP. Schematic is not drawn to scale and is not a true representation of MGITC and DNA loading onto the AuNP surface.

Chol-DNA consisted of a single 12-thymine base strand, which was modified at the 5' and 3' position with a thiol group and a cholesteryl-TEG functionality respectively. Thiol linkages are widely used for chemisorption onto the AuNP surface.[156] This covalent attachment allows for a stable conjugation between the nanoparticle and the oligonucleotide.[156,157] The cholesteryl-TEG moiety, consisted of a triethylene glycol (TEG) group which is most commonly used to link the cholesterol to the DNA.[158] The chemical structure of chol-DNA is given below, in Figure 3.5. The 5' end modified with a thiol linker is illustrated in Figure 3.5(a), and the 3' end modified with a cholesteryl-TEG functionality is given in Figure 3.5(b). It should be noted that a control of poly-thymine DNA (polyT-DNA) was also used in this work, which

essentially was the 12-thymine base strand, modified with a thiol moiety at the 5' position, yet without the cholesteryl-TEG functionality. This would help in understanding the specific role of cholesterol *in vitro.*
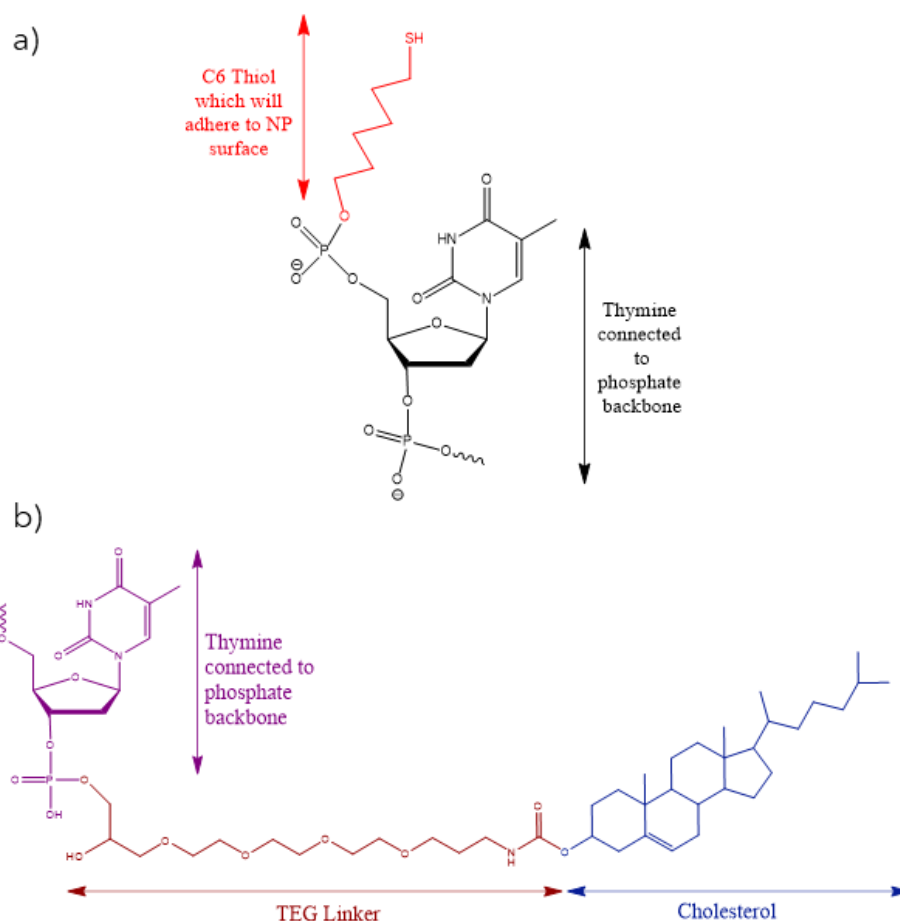
Figure 3.5: Chemical structure of cholesterol DNA, which was made up of 12 thymine bases connected to the sugar-phosphate backbone. Modifications at the 5' and 3' positions consisted of: (a) a thiol moiety at the 5' position and (b) a cholesteryl-TEG group at the 3' position.

The ssDNA is comprised of only thymine bases due to the reason that it has a lower binding affinity for the surface of the NP, in comparison to its other counterparts: adenine, cytosine and guanine (Figure 3.6).[159,160] The counterpart bases have been known to bind to the surface via the two

nitrogens, and since this is not possible with thymine, its affinity for the surface is decreased.[161] In addition to this, a thymine chain does not form any secondary structures.[162] This led to the belief that thymine, from all DNA bases, was least problematic and would be suitable for acting as a linker between the cholesterol functionality and nanoparticle surface. Thymine's disinclination to lie on the surface or fold in itself would potentially result in efficient packing of the oligonucleotide.
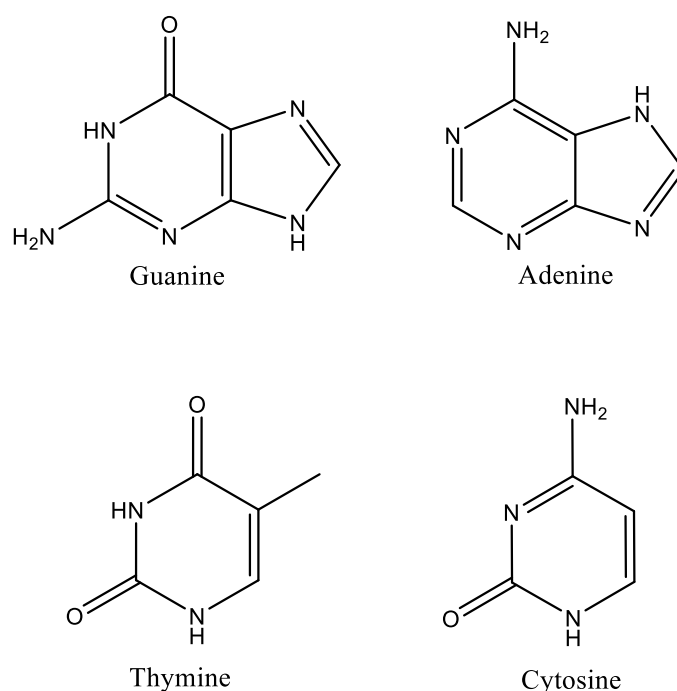
Figure 3.6: Chemical structures of DNA bases: adenine, guanine, cytosine and thymine. Thymine was preferred over other DNA bases due to having a weak affinity for the surface and the ability to not form secondary structures within itself.

Potentially the main challenge of DNA functionalisation is the AuNP surface and the sugar-phosphate backbone of DNA both possessing negative charges. Therefore, electrostatic repulsion prevents spontaneous adsorption of the DNA onto the surface of the nanoparticle. To overcome this, typically, a salt-aging protocol is used during the functionalisation

process, where NaCl is added stepwise over 1-2 days, a concept introduced by Mirkin's group.[163,164] In such a case, the Na$^+$ ions screen the negative charges associated with the DNA phosphate groups and the citrate on the AuNPs, therefore allowing the oligonucleotide to gradually adsorb onto the NP surface. Although, the procedure is said to work less efficiently for large AuNPs (50 nm), with added steps of salt addition becoming a requirement.[165] Another issue here lies in the impracticality of such a step in a lengthy procedure where subsequent cell work has to be carried out, alongside the fact that slow additions need to be added to the suspension so as not to trigger irreversible aggregation within the AuNPs. Zhang *et al*. reported the use of a low pH sodium citrate buffer for quick and efficient loading of DNA onto the AuNP surface where they used a pH 3 citrate buffer for the salt addition steps.[165] Kinetic studies highlighted that >80% of the DNA adsorption took place within the first 2 minutes of pH 3 sodium citrate addition, suggesting DNA adsorption is strongly dependent on pH. Furthermore, they resuspended the conjugates in a pH neutral buffer indicating that pH adjustment was only necessary for that one sodium citrate addition step. Hence, this method of DNA functionalisation was chosen as it was relatively quick and efficient. The NP functionalisation procedure was optimised, and it was found that an estimated 4000 DNA strands per NP (4000:1) were sufficient for monolayer coverage (Figure 3.7). The optimisation study was carried out using extinction spectroscopy, in which the extinction profile of chol-DNA AuNPs exhibited aggregation at low ratios of DNA to AuNP. The optimum was 4000:1 as with an estimated 6000 DNA strands per NP, the absorbance decreased, which potentially may be due to aggregation. Cholesterol is hydrophobic and by increasing the hydrophobicity on the NP surface, this may have reduced the solubility of the NP. When the study was repeated with polyT-DNA AuNPs, it was found that the extinction profile was similar for both 4000:1 and 6000:1 DNA to AuNP ratios. This may have been due to polyT-DNA not being highly hydrophobic, hence allowing the NP to retain solubility. It was decided to

move forward with utilising a 4000:1 DNA to AuNP ratio for all subsequent studies.
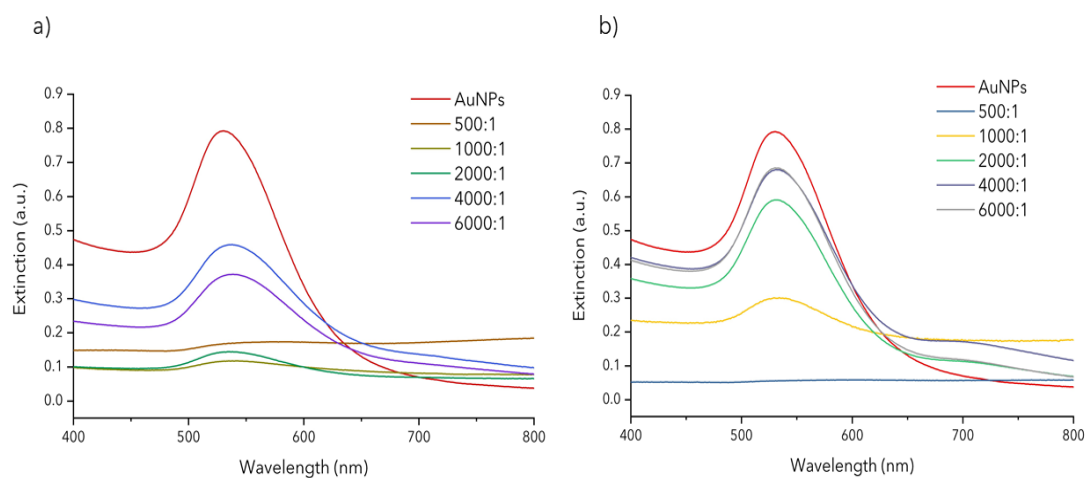
Figure 3.7: Extinction spectroscopy data outlining increasing DNA loading onto AuNPs for a) chol-DNA and b) polyT-DNA AuNPs. In both cases, an optimum ratio of 4000:1 DNA:AuNPs was found and this was used in all subsequent studies. All spectra were acquired using a 600 nm/min scan rate.

Extinction spectroscopy was the preferred route by which these conjugates were characterised. This provided a quick screening method, which would outline changes to the NP surface with a shift in LSPR and would also highlight any aggregation. As a control, PolyT-DNA AuNPs were used which essentially were AuNPs with MGITC and ssDNA, with the latter not possessing the cholesteryl-TEG functionality. Using these as a control would also help to decipher the specific role of cholesteryl-TEG in cellular uptake in subsequent cell studies. Bare AuNPs were also used as a control. The extinction spectra are shown in Figure 3.8.
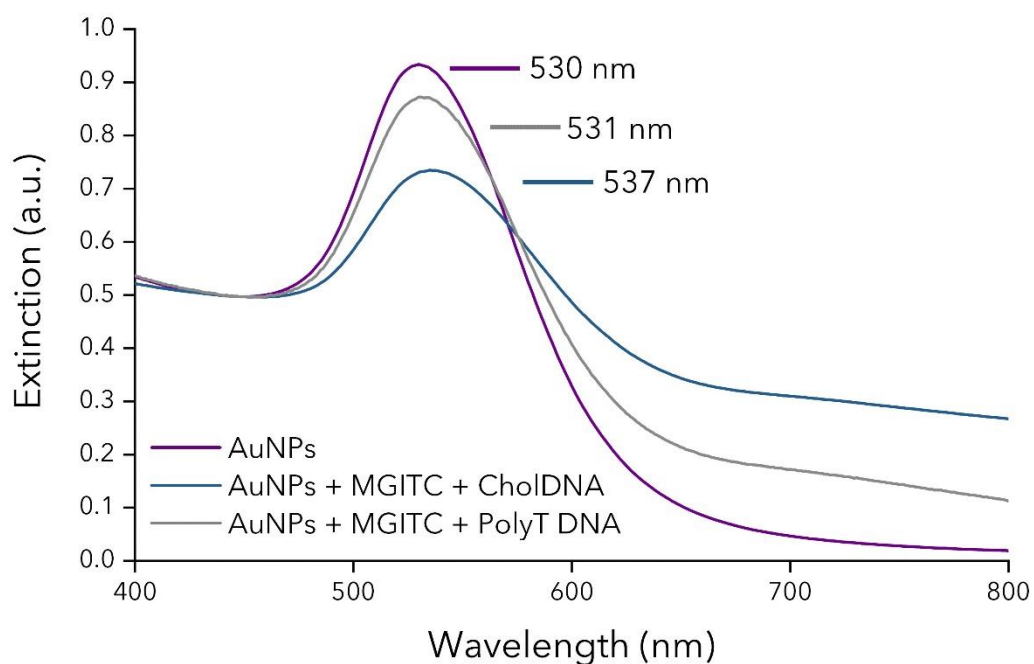
Figure 3.8: Extinction spectra of bare AuNPs (purple), cholesteryl-TEG functionalised AuNPs (blue) and PolyT functionalised AuNPs (grey). Spectra were acquired at a baselined scan rate of 600 nm/min, with three replicates. Spectra were averaged and normalised (at 450 nm) using Microsoft® Excel and Origin®. Un-normalised spectra provided in Appendix 2.

Extinction spectroscopy provided a straight-forward route of determining successful functionalisation as a change in the extinction profile would be relative to AuNP surface modifications. This would be highlighted by a bathochromic (red) shift in the LSPR, peak broadening and peak dampening.[166] A 7 nm LSPR shift of the conjugates was evident of the fact that there was a change in the surface functionality, resulting from a change in the refractive index, indicating that chol-DNA was on the surface. The cholesteryl-TEG was a bulky functionality, and upon addition to the surface changed the overall diameter of the particle which in turn shifted the LSPR to a longer wavelength. This statement could be supported with the DLS data which gave an average hydrodynamic radius of 72 ± 0.7 nm for the

chol-DNA functionalised AuNPs in comparison to 51 ± 0.8 nm from the bare AuNPs and 66 ± 1.6 nm for the control of polyT-DNA AuNPs.

The Raman active dye chosen for this particular work was MGITC (Figure 3.9). This would provide a unique fingerprint spectrum, aiding the detection of the fatty particles once inside the cellular environment. MGITC is known to provide enhancement factors approximately 200-fold higher than that of malachite green (MG).[167] This is attributed to the anchoring isothiocyanate group of MGITC which enables strong electronic coupling to the nanoparticle surface, thus allowing for overall higher enhancement factors due to its more efficient chemical enhancement in comparison to MG. Additionally, it has a strong scattering providing a characteristic, intense SERRS signal. It's strong absorption band at 620 nm (Figure 3.9) meant that it could be used with the in-house available 633 nm laser excitation available with the InVia microscope, which would be used to map cells when investigating cellular uptake.[167] Matching the laser excitation as close as possible to the MGITC absorbance maxima would intensify the scattering due to the resonance enhancement of the dye signal.
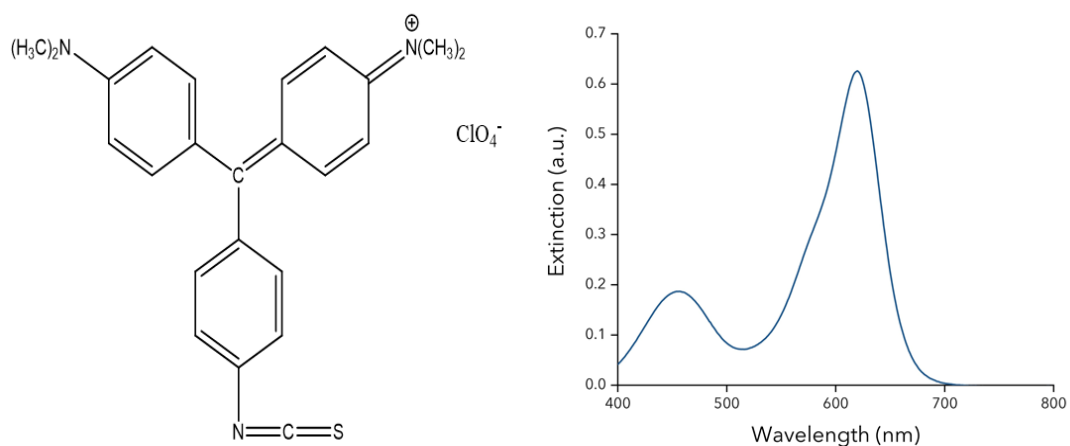
Figure 3.9: (Left) Structure of malachite green isothiocyanate (MGITC), which was chosen as the analyte for detection. MGITC is a triaryl dye made up of two amino groups and one isothiocyanate group, which helps to bind the dye to the AuNP surface. (Right) Extinction spectrum of MGITC showing an LSPR of 620 nm. Spectra acquired using a scan rate of 600 nm/min.

Typically, the dye can be added before or post DNA functionalisation as can be witnessed through the works of Graham *et al*.[168] and McKenzie *et al*.[169] respectively. In this investigation, the dye was added prior to the chol-DNA as mentioned in section 6.1.3.4 of the Experimental chapter. By experimentation, as detailed in section 6.1.3.3 of the Experimental chapter, it was found that functionalisation of DNA prior to dye addition hindered much of the latter from attaching to the surface, likely due to the bulky nature of the cholesterol moiety. This resulted in a weak SERRS response which would not be detected in cells. Reversing the order displayed a considerably intensified SERRS spectrum of MGITC, which was obtained using a Snowy Range Raman spectrometer with a 638 nm laser excitation wavelength. MGITC (1 µM) was added at this particular concentration as it was the lowest concentration which provided an intense fingerprint. The aim was to maximise NP surface for DNA attachment. Upon DNA functionalisation and after undergoing a centrifugation step to remove any unbound dye and DNA, the SERRS spectrum exhibited intense peaks. This highlighted that a high concentration of MGITC had attached to the AuNP surface, and also that the DNA had not displaced it. Although the MGITC was bound via a strong thiol bond, there was a concern that the bulky DNA may cause interferences, however, this did not happen. SERS spectra taken before, and post chol-DNA addition are shown in Figure 3.10.
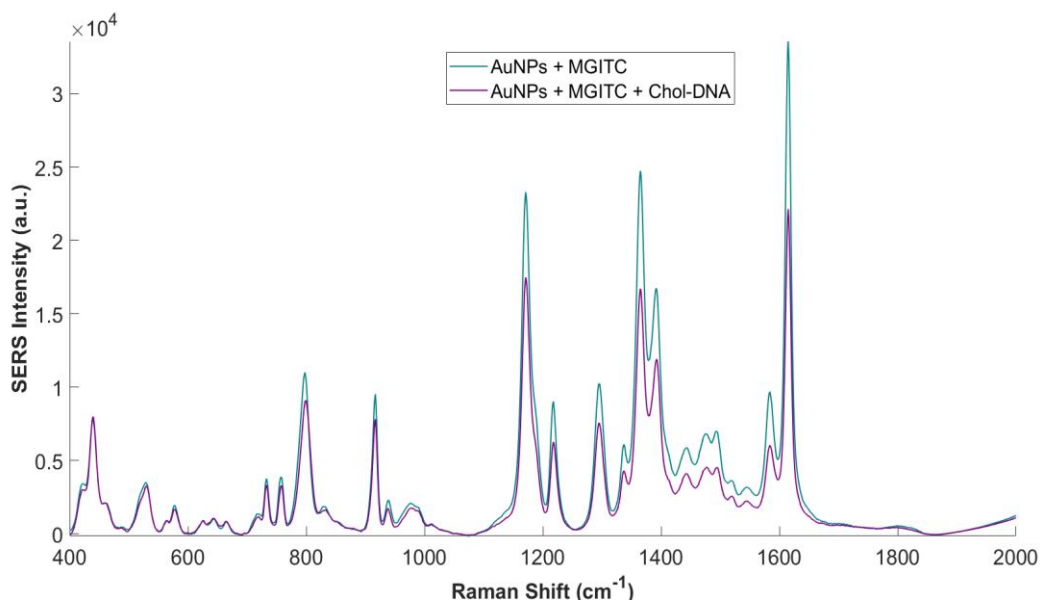
Figure 3.10: SERS spectrum displaying functionalisation of AuNPs and MGITC (Teal) and AuNPs, MGITC and chol-DNA (Purple). Spectra were acquired on a Snowy Range Raman spectrometer using a 638 nm laser excitation wavelength. A 40 mW laser power was utilised with an integration time of 1 second. Data presented is an average of three replicates and all data was processed and averaged in MATLAB®.

From the above spectra, it was evident that there was a slight drop in intensity after the DNA addition and this was attributed to the centrifugation stage at the end of the functionalisation process, which removed excess unbound dye molecules from the solution. Although, there was also the potential that the addition of DNA may have also removed some of the dye. The resulting dye fingerprint provided clear sharp peaks which are commonly characteristic of a typical MGITC spectrum. These peaks are associated with various bending and stretching modes within the molecule and typical assignments correlated with the main peaks are given in Table 1. An intense response from the MGITC was pivotal prior to cell studies as upon successful cellular uptake, a reduction in analyte signal is anticipated as cellular components and cell membrane can interfere with the dye signal.

Table 1: Raman and SERS peak assignments of MGITC.[170,171]

Raman Peak (cm^{-1})	SERS Peak (cm^{-1})	Vibrational Assignment
807	800	C-H bend from benzene ring
920	917	b_{1u} in plane benzene ring
1178	1171	In-plane C-H bend, benzene v_9 mode
1298	1295	In-plane C-H and C-C-H
1369	1365	N-Phenyl ring stretch
1604	1584	Stretch and bend of in-plane ring
1621	1615	N-Phenyl ring and C-C stretch

The control of polyT-DNA AuNPs, however, displayed greater intensity once the polyT-DNA was attached. Although the exact reason for this is unknown, it could be possible that there was slight aggregation, which would result in an increase in the intensity of the vibrational fingerprint. There may have been exposed NP surface which would in turn result in aggregation upon the addition of salt. This is less likely with chol-DNA AuNPs as the cholesterol group is itself bulky which provides sufficient coverage of the surface. The SERRS of the control is provided in Figure 3.11.
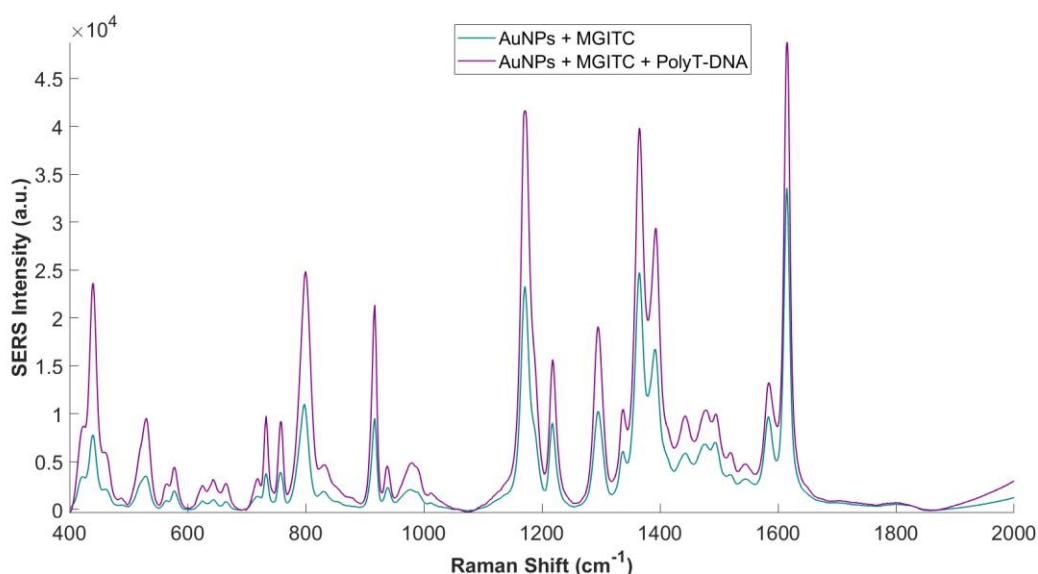
Figure 3.11: SERS spectrum displaying functionalisation of AuNPs and MGITC (Teal) and AuNPs, MGITC and polyT-DNA (Purple). Spectra were acquired on a Snowy Range Raman spectrometer using a 638 nm laser excitation wavelength. A 40 mW laser power was utilised with an integration time of 1 second. Data presented is an average of three replicates and all data was processed and averaged in MATLAB®.

3.1.3.3 Salt Stability Test

As previously mentioned, citrate-coated AuNPs undergo aggregation upon the addition of salt due to electrostatic screening of the negative surface charges by the salt cations (Na^+ ions).[172,173] Hence, without full surface coverage by DNA, aggregation would be induced, resulting in the SPR shifting to longer wavelengths, visible through a colour change from deep red to blue/purple, as shown in Figure 3.12. In this study bare AuNPs aggregated with the addition of salt, yet the AuNPs with monolayer coverage of chol-DNA and polyT-DNA retained their vibrant deep-red colour. This was also evidence of monolayer coverage, as otherwise, these conjugates would have also undergone aggregation. However, it was mentioned in the previous section (section 3.1.3.2.) that there may be little aggregation with the control (polyT-DNA AuNPs) as the SERRS after DNA

addition was enhanced. It can be proposed that although there is no visual aggregation, it may be on a smaller scale, which is not noticeable.

Figure 3.12: Image depicting effect of salt addition to bare AuNPs. Negative charges screened by Na^+ cations induce aggregation and result in a colour change from a deep red to blue/purple. Chol-DNA and PolyT-DNA coated AuNPs did not aggregate due to sufficient monolayer coverage.

3.1.3.4 Understanding the Long-Term Stability of Cholesterol Functionalised Nanoparticles

A major setback with working with cholesterol is its hydrophobicity, which greatly hinders its solubility. To overcome this challenge, a surfactant - Tween 20™ - was used with PBS buffer (PBST) to suspend the resulting conjugates. PBS buffer was used to allow the conjugates to equilibrate in ionic conditions and maintain them in physiological pH. Tween 20™ is a polyoxyethylene sorbitol ester belonging to the polysorbate family and is a non-ionic gentle surfactant.[174] Various concentrations of Tween 20™ were investigated to determine a safe concentration, i.e a concentration that would not cause cellular damage when *in vitro* studies were carried out. Like

most surfactants, Tween 20™ is also commonly known to permeabilise cells and high concentrations can result in cell lysis.[175] Experimental studies (section 6.1.3.7) carried out studying different concentrations with cells determined 0.05 % Tween 20™ in PBS as safe, as no visible damage to the cell membrane was observed when fixed cells were viewed under a bright light microscope.

Thereafter, stability studies of the cholesterol modified AuNPs were carried out to determine whether the cholesterol was stable in the PBST suspension or if it had started to form aggregates. In the first instance, a kinetic study was carried out for 15 hours after the functionalisation was completed, using extinction spectroscopy. The resulting spectra are shown in Figure 3.13(a). From the data, it was clear that the conjugates were stable. In the case where the conjugates had started to aggregate, this would be evident with the emergence of a peak ~650 nm. 15 hours was chosen as this was the maximum length of study on the instrument, however, this time frame was sufficient as it was more than the length of time the conjugates were incubated with cells. Hence, it could be concluded that they were stable for the duration of *in vitro* studies.

A second study was carried out to determine the period over which the conjugates remained stable. Analyses were carried out upon completion of functionalisation and intermittently over three weeks. The extinction spectra displayed neither a formation of an aggregation peak or any drastic changes to the LSPR. Visibly, the conjugates looked stable with no change in colour or aggregates settling at the bottom of the Eppendorf. The extinction spectra were taken initially and at the end of week 3 are given in Figure 3.13(b). Studies were not carried out for a greater length of time due to the likelihood of using the conjugates within the three weeks.
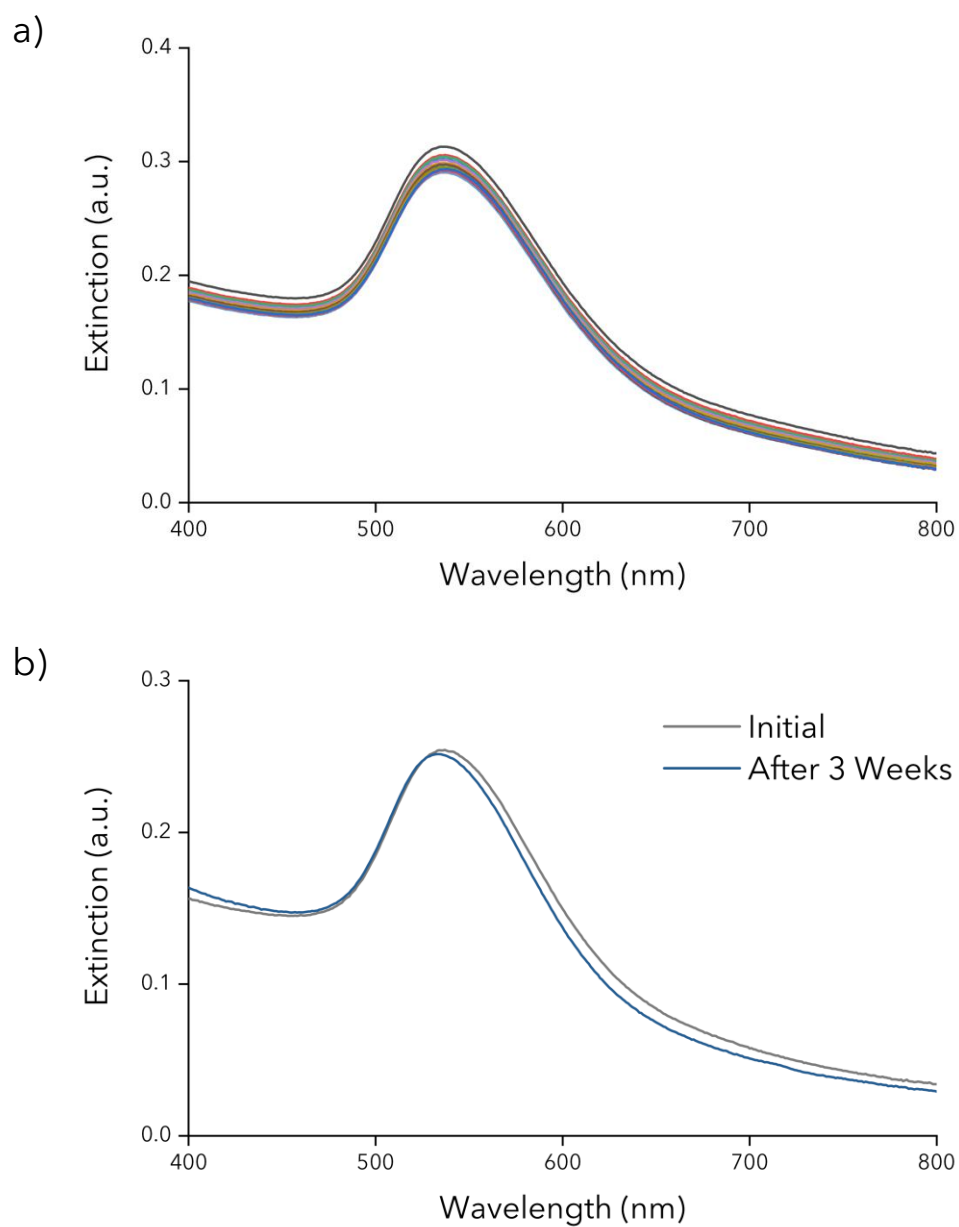
Figure 3.13: Extinction spectra taken from stability studies of chol-DNA conjugates. a) 15-hour kinetic study carried out upon completion of synthesis. b) comparison of initial extinction spectra versus spectra at three weeks. Studies show stability of conjugates. Spectra were acquired with a scan rate of 600 nm/min.

3.1.3.5 Concluding Remarks

With the need for non-cytotoxic nanoparticles, AuNPs were chosen as the 'core' for the building of 'fatty nanoparticles.' A stable, monodispersed colloidal suspension was synthesised using a modification of the Turkevich method, yielding nanoparticles which were ~40 nm as shown by the SEM data. The use of large AuNPs was seen as beneficiary with the enhanced SERRS, observed upon functionalisation of MGITC onto the AuNP surface. The choice of MGITC was attributed to its possession of an isothiocyanate group which is seen as a strong anchor to the AuNP surface, greatly increasing the ability for successful functionalisation. Previous to MGITC, other Raman reporters were also investigated, including: PYOT (5-(4-pyridyl)-1,3,4-oxadiazole-2-thiol), BPE (1,2-bis(4-pyridyl)ethylene) and PPY (polypyrrole). These did not provide an intense SERS signal which could be used for 2D and 3D mapping, hence studies were carried forward with MGITC.

Chol-DNA functionalisation was facile with the aid of pH-assisted salt addition, which minimised the electrostatic repulsion between the negatively capped AuNP surface and sugar-phosphate DNA backbone. With cholesterol being a hydrophobic group, the resuspending buffer had 0.05% Tween 20™ added to it to help with solubilisation and the concentration was low to not affect the cell membrane during *in vitro* studies. A 15-hour kinetic study determined the stability of the fresh conjugates and a comfortable shelf-life of three weeks was also determined through extinction spectroscopy.

Stable fatty nanoparticles, which have been synthesised can now be moved onto the next stage of determining their uptake in the cellular environment. Every effort was made to minimise their cytotoxic nature, which will be investigated through toxicology studies subsequently.

3.2 The *In Vitro* Study of Cholesterol Modified Nanoparticles

3.2.1 Sub-Chapter Introduction

3.2.1.1 Nanoparticles in Cells

Nanoparticles are increasingly being used for *in vitro* and *in vivo* studies. Research studies have aimed to deduce the optimum characteristics of a nanoparticle for cellular studies, yet a 'standard' does not exist. This is because each application is different. The intracellular uptake of nanoparticles are dependent upon several physicochemical properties such as size, shape, surface charge and chemistry.[140]

Multiple studies/reviews have endeavoured to understand the optimum shape for cellular uptake, as will be mentioned subsequently. The shape is a key parameter in the cellular uptake pathway and also trafficking of nanoparticles.[141] NPs exist in spheres,[48] rods,[176] cages,[177] triangles[178] etc, and the majority of them have been used for cellular uptake.[177,179-181] A study by Chithrani *et al.* suggested that spherical NPs had increased cellular uptake compared to their rod-like counterparts in studies with HeLa cells, potentially due to the longer membrane wrapping time for nanorods.[141,180] Another study by Jeong-Lee *et al.*, carried out in HepG2 cells reached a similar conclusion, in which chitosan capped nanostructures were studied.[182] Multiple studies have shown spheres to have enhanced uptake in comparison to their counterparts, however other structures are still studied.

A key factor in determining the efficiency of nanoparticles in cellular uptake is size. Chithrani *et al.* investigated the effect of size where nanoparticles were synthesised with diameters between 14 and 100 nm.[180] Subsequently, incubating these NPs with HeLa cells indicated 50 nm to have the greatest uptake, determined by TEM and ICP-AES (Figure 3.14(a)). Kinetic studies were also carried out which highlighted that nanoparticle uptake was

increased at earlier time points (0-2 hrs) and slowing thereafter, reaching a plateau at 5 hrs. (Figure 3.14(b)).
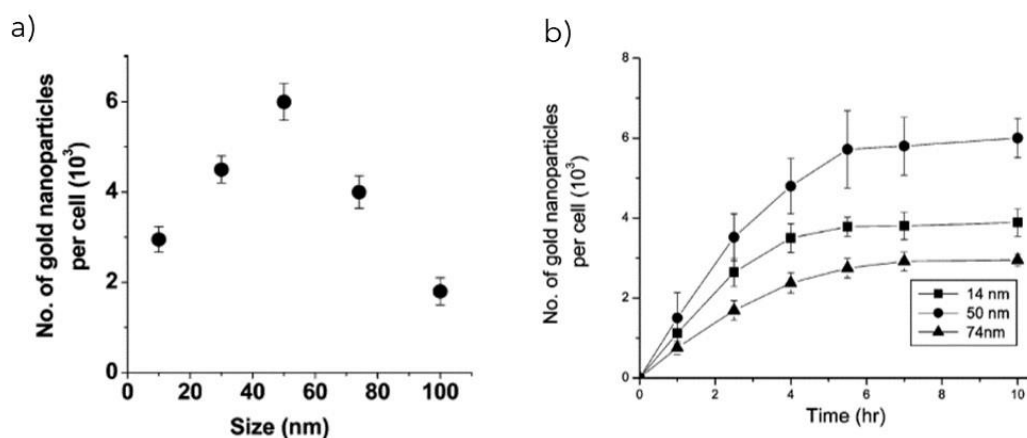
Figure 3.14: a) Size dependence of AuNPs in cellular uptake showing 50 nm to be the optimum size for cellular uptake. b) Kinetic studies of three different sized AuNPs (nanoparticle diameters 14, 50 and 74 nm), highlighting the increased uptake of 50 nm AuNPs in comparison to the other two. Image reprinted with permission from *B. D. Chithrani, A. A. Ghazani and W. C. W. Chan, Nano Lett., 2006, 6, 662–668.* Copyright © (2020) Americal Chemical Society.

Nanoparticles are known to predominantly enter cells via the mechanism of endocytosis,[140,183,184] where they interact with components of the plasma membrane and enter the cell.[185] They are engulfed in membrane invagination, followed by budding and "pinching off" to form endocytic vesicles. Endocytosis can further be classified as several types, as illustrated in Figure 3.15. Although these are the widely known processes, other entry mechanisms are less commonly proposed, including passive diffusion, direct microinjection and electroporation.[183,184] Osaki *et al.* correlated the size of NPs to the route of intracellular uptake, which indicated that 50 nm quantum dots enter via the endocytic route.[186]
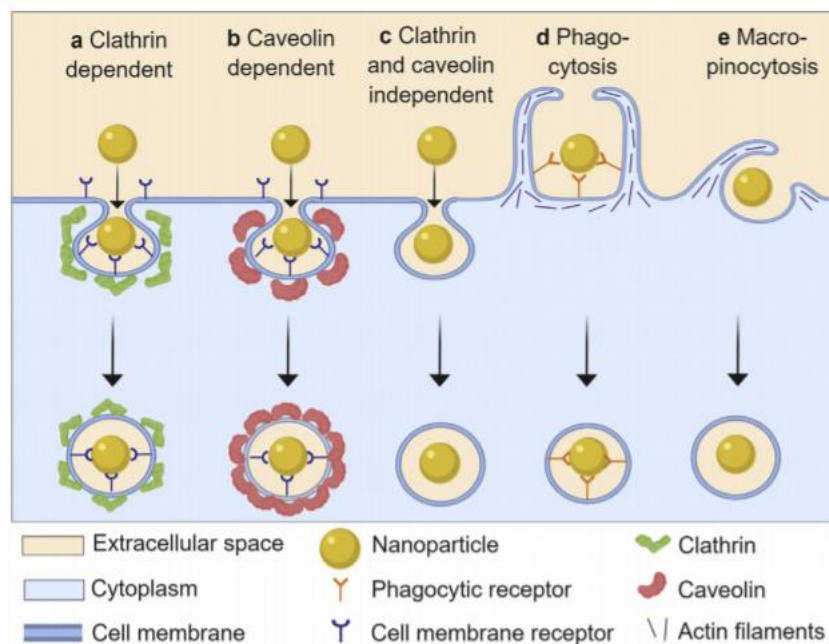
Figure 3.15: Schematic depicting the many endocytic nanoparticle uptake pathways: a) clathrin-dependent; b) caveolin-dependent; c) clathrin- and caveolin-independent; d) phagocytosis and e) macropinocytosis pathways. "Reprinted from Advanced Drug Delivery Reviews, Vol 143, Nathan D. Donahue, Handan Acar, Stefan Wilhelm, Concepts of nanoparticle cellular uptake, intracellular trafficking, and kinetics in nanomedicine, Pages 68-96., Copyright (2019), with permission from Elsevier.

The principal parameter which determines the interaction between the nanoparticle and the cell is the surface functionality of the former. By engineering the surfaces with various biomolecules such as antibodies, DNA, aptamers, these can guide the nanoparticles, acting as targeting and biorecognition probes for both *in vitro* and *in vivo* imaging. In this work, the effect of lipid modification on the NP surface was investigated. Lipids have been known to enhance cellular interactions, as mentioned in section 3.1.1. However, their role in cellular uptake is understudied, which was the aim herein.

3.2.1.2 The Importance of Cholesterol Modified Nanoparticles Within the Cellular Environment

Lipid modifications have been used for either membrane binding or internalisation into a cell. Predominantly, such studies have not investigated their performance when coupled with nanoparticles. Fatty biomolecules such as LDL-C and HDL-C have a pronounced presence in the body.[13] Exploiting their characteristics can be advantageous for many research interests. For example, LDL-C is known to be upregulated upon endothelial dysfunction, which leads to the progression of an atherosclerotic plaque.[6] In addition to this, fatty acids are also known to by-pass the endothelial barrier to enable tissue uptake in muscle and adipose. Fatty acids are known to induce the generation/secretion of various pro-inflammatory molecules in endothelial cells, which may be involved in the recruitment of macrophages and other biomolecules into atherosclerotic lesions.[187,188] Hence, understanding the uptake of lipid modified NPs can be advantageous as it is evident that various hydrophobic biomolecules present in the human body have enhanced uptake with endothelial cells. Creating lipid modified NPs essentially creates a hydrophobic NP, which may be able to imitate these biomolecules at the site of damage.

The work presented herein would aim to uncover the role of cholesterol in maximising uptake of NPs, and in parallel, would help in understanding whether these fatty nanoparticles could be used for targeting endothelial cells in the development of an atherosclerotic plaque.

3.2.1.3 Raman Analysis as a Tool for *In Vitro* Studies

Raman spectroscopy is rapidly evolving into a vital tool for *in vitro* and *in vivo* studies. In particular, the coupling of a confocal microscope and a CCD (charged-coupled device) to the Raman spectrometer, has allowed for cellular imaging, and in specific the determination of intracellular

components.[123] The first example was described in 1990 when it was used to study single cells and chromosomes with a high spacial resolution.[122] As time progressed, this technique became applicable for disease studies and diagnostics, as the cameras became faster and the CCD sensitivity increased, allowing for quicker data collection and better image resolution.[189] Techniques such as SORS (spatially offset Raman spectroscopy) and SESORS (surface enhanced spatially offset Raman spectroscopy) also evolved, which offered depth profiling for deeper layers of tissue, again contributing to the increasing interest in Raman imaging.[190,191]

Incorporating SERS *in vitro* was first demonstrated in the work of Nabiev *et al*., in which they reported the selective measuring of antitumor drugs in the nucleus and cytoplasm of a living cancer cell based on SERS.[192] In their study, cells were treated with doxorubicin – an anti-cancer drug – subsequently incubating with AgNPs to detect the location of a drug within the cellular environment.[192] Later, SERS became a viable route of directly detecting DNA, proteins and other cellular components.[193] Incorporating a Raman-active dye or a reporter molecule onto the surface of a nanoparticle, and carrying out Raman mapping could indicate the locality of the probes within the cellular environment. In addition to this, NPs increase the sensitivity and selectivity for areas of interest. In comparison to techniques such as TEM, Raman imaging is non-destructive and quicker.[194,195] This work saw a focus on 2D and 3D SERRS imaging. A Raman dye (MGITC) was incorporated onto the modified NP surface, which would allow for tracking its vibrational fingerprint through the cell. MGITC was resonant with the excitation laser, further intensifying the SERRS spectra. 2D SERRS mapping would determine if the modified NPs were successfully uptaken by cells, which would be further confirmed using 3D mapping. This would aid in identifying the cellular uptake capabilities of cholesterol modified NPs.

3.2.2 Chapter Aims

Moving forward from the successful conjugation of chol-DNA to AuNPs, the next stage involved a series of *in vitro* studies using 2D and 3D SERRS mapping techniques with the aid of an inVia Raman confocal microscope and DCLS false colour plots for analysis. The aim of the first *in vitro* study was to determine whether these conjugates were able to cross the cellular membrane or if they would retain in the cell membrane, as previously cholesterol modified nanostructures have known to insert into the lipid bilayer, due to cholesterol predominantly residing in the cell membrane.[133] For this particular study, RAW 264.7 murine macrophages were utilised as they are frequently used for *in vitro* studies in literature.[76,129,179,196] Firstly, 2D SERRS mapping was carried out to determine whether there was a response from the intracellular environment, subsequently carrying out 3D SERRS mapping to confirm signal from within the cell. For comparison purposes, a control of polyT-DNA AuNPs was used. In an attempt to 'semi-quantify' the relative SERRS response, the % area of SERRS response versus the total cell area was calculated using an approach whereby the false colour DCLS plots were converted to monochromatic red colour and quantified. Thereafter, live cell mapping was undertaken to outline any changes to the SERRS fingerprint upon fixation and finally, a multiplexing approach was used to in an attempt to highlight the increased localisation of chol-DNA AuNPs over polyT-DNA AuNPs.

Upon the successful intake of the chol-DNA AuNPs, the next study aimed to decipher if there was a pronounced uptake in endothelial cells (HUVECs), with a future aim that these probes could be used as photothermal agents to ablate such cells. This would be beneficial *in vivo* where LDL-C are taken up by endothelial cells, in the progression of atherosclerosis. Here, the control was switched to pegylated nanoparticles (PEG-AuNPs) as they are routinely used in cellular studies. 2D and 3D SERRS mapping was again carried out to determine HUVECs uptake with chol-DNA AuNPs and in the

latter, attempts were made to co-localise the SERRS response to cellular signals. Finally, cytotoxicity studies were also carried out, which would determine if the probes were toxic to cells, allowing an enhanced understanding if these probes could be used *in vivo*.

3.2.3 Determining Cellular Uptake of Cholesterol Modified Nanoparticles by RAW 264.7 Macrophages

3.2.3.1 2D SERRS Mapping of Cholesterol Modified Nanoparticles in RAWs

RAW macrophages are routinely used for *in vitro* studies of NP uptake.[76,129,179,196] Hence, prior to sourcing endothelial cells, it would help to decipher an outcome with the nanoparticles in focus. We aimed to compare the uptake of NPs in RAWs and endothelial cells to determine, if any, the differences in the distribution of chol-DNA AuNPs. It was hypothesised that a lipid modified NP may have enhanced uptake with endothelial cells, in efforts of imitating LDL-C and other fatty biomolecules within the human body, which have shown pronounced uptake with the endothelium. This would potentially mean that these cholesterol modified NPs could be used to target plaque sites (at the endothelium), subsequently irradiating them with a NIR laser, therefore ablating surrounding plaque. It should be noted that macrophages are known to phagocytise and therefore many debate that they predominantly engulf incoming biomolecules. However, several studies have shown that this is dependent upon size and only particles above a certain diameter (>500 nm)[197] are known to enter via phagocytosis.[140,183,197]

RAWs were plated at a concentration of 0.4×10^6 cell/mL and incubated for 24 hours on glass coverslips, prior to treating with the chol-DNA AuNPs (6 ρM). PolyT-DNA AuNPs, which were AuNPs functionalised with a poly-thymine (PolyT) chain, were used as the control. These would aid in

highlighting the specific role of the cholesterol, as the polyT-DNA did not contain a cholesterol moiety. The treated cells were incubated for 3 hours prior to fixation. Samples were analysed using a Renishaw inVia Raman confocal microscope. A 633 nm laser excitation was used, at 5 % laser power (0.18 mW) to avoid sample burning. A ×50 lens objective, 1800 mm^{-1} grating and 1 second accumulation times were also set. Data were acquired over a spectral range of 715 – 1829 cm^{-1}, with a step size of 2 μm in the *x* and *y* direction.

2D SERRS mapping would identify the distribution of the functionalised AuNPs in the cell. A reference spectrum of the Raman dye present on the surface was taken before mapping studies (Figure 3.16(e)). Post mapping, all spectra were pre-processed using the baseline subtraction and cosmic ray removal function in WiRE™ 4.2. Additional details of the pre-processing can be found in section 6.2.2.1 of the Experimental chapter. Subsequently, false colour images were generated using direct classical least squares (DCLS). This method of analysis is typically used when reference spectra are available of the components and allows fitting of the unknown data (collected during mapping) to a linear combination of the specified component spectra, which in this case was MGITC. Where there was a fit between the collected spectra from the cell and the reference spectrum, a gradient red false colour was applied, highlighting the intracellular location of the NPs. DCLS analysis from both the cholesterol and polyT-DNA functionalised AuNPs in cells are shown in Figure 3.16. These are presented as representatives of typical DCLS plots observed, as all samples had 10 biological repeats. This figure also displays a typical MGITC fingerprint taken from the cell and compared to the reference spectrum of MGITC, which shows there is good agreement between the two. A considerable fit is observed, which also highlights minimal changes to the peaks. Differences can occur due to either changes in the dye orientation or when the NP is in contact with cellular components. The scalebar was set at a minimum of 0.5

and a maximum of 0.85. These values correlated with the degree of spectral fit, with a value of 1 being a 100% spectral fit of the reference spectrum. This is impossible and typically the maximum is usually found to be 0.8/0.9. The minimum value was selected as 0.5 which had a 'good spectral' overlapping with the MGITC fingerprint such that it was possible to distinguish the spectra as a MGITC signal. Values below 0.5 were typically noise spectra.
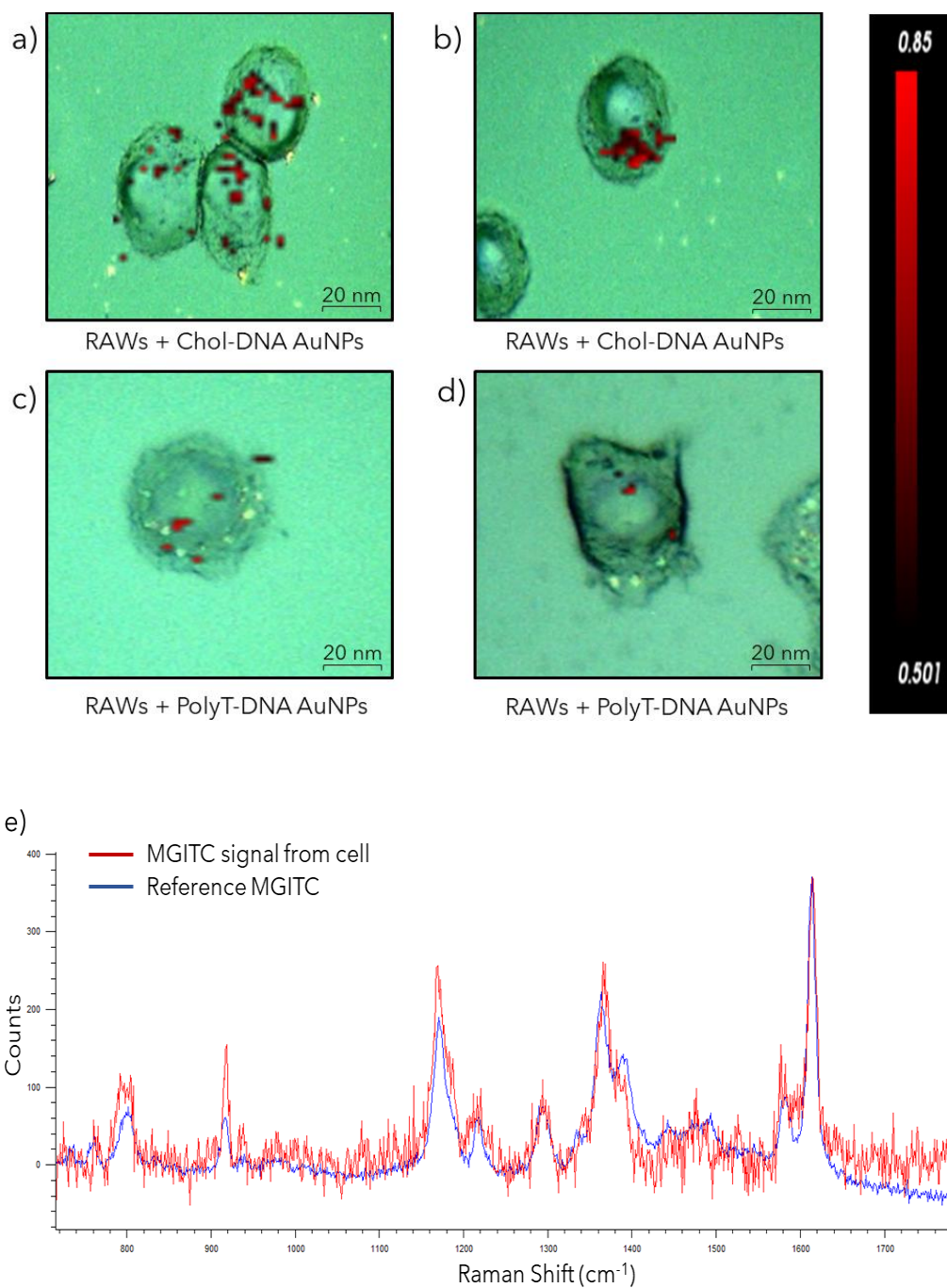
Figure 3.16: DCLS analysis of 2D SERRS mapping of functionalised AuNPs in RAWs. a/b) RAWs + chol-DNA AuNPs, c/d) RAWs + PolyT-DNA AuNPs. Cells mapped using a Renishaw inVia Raman confocal microscope and data processed using WiRE™ software. Maps were acquired using 1 second acquisition time and a 633 nm excitation, at a 5 % laser power. False colour images were generated post analysis using DCLS and show chol-DNA AuNPs having increased cellular uptake in comparison to the control of polyT-DNA AuNPs. e) Example spectrum of a MGITC signal observed from the cell (red), compared to the reference MGITC spectrum used for DCLS analysis (blue).

From the analysis in Figure 3.16, it was evident that there was increased uptake of the chol-DNA AuNPs, in comparison to the polyT-DNA AuNPs control, indicated by the increased area of false colour observed. It should be noted that the number of pixels did not correlate with the number of nanoparticles at the site, as at present this remains a challenge and nanoparticle quantification *in vitro* remains an area under study. Another point that can be mentioned is that the mapping step size was 2 μm so the signal was likely to be from many NPs together and not individual ones. A method was devised by Kapara *et al.* in which the pixel area corresponding to the functionalised AuNPs in cells was calculated versus the total cell area mapped, providing a 'semi-quantitative' method.[70,198] Such a procedure required converting the gradient false red DCLS plot to monochromatic red colour using WiRE™ 4.2 software. Thereafter, using ImageJ (image processing package by Fiji), the percentage of red pixel area versus the full cell area was calculated. The step-by-step process is presented in section 6.2.2.2 of the Experimental chapter. Although not a direct quantification, this route provided a relative value for the uptake of the nanoparticles per sample. Such an approach was quick and non-destructive in comparison to other techniques which can be used such as TEM (transmission electronic microscopy) which becomes time consuming and expensive. The % area of SERS responsive pixels from the two samples (10 cells per sample investigated) were averaged and plotted as shown in Figure 3.17.
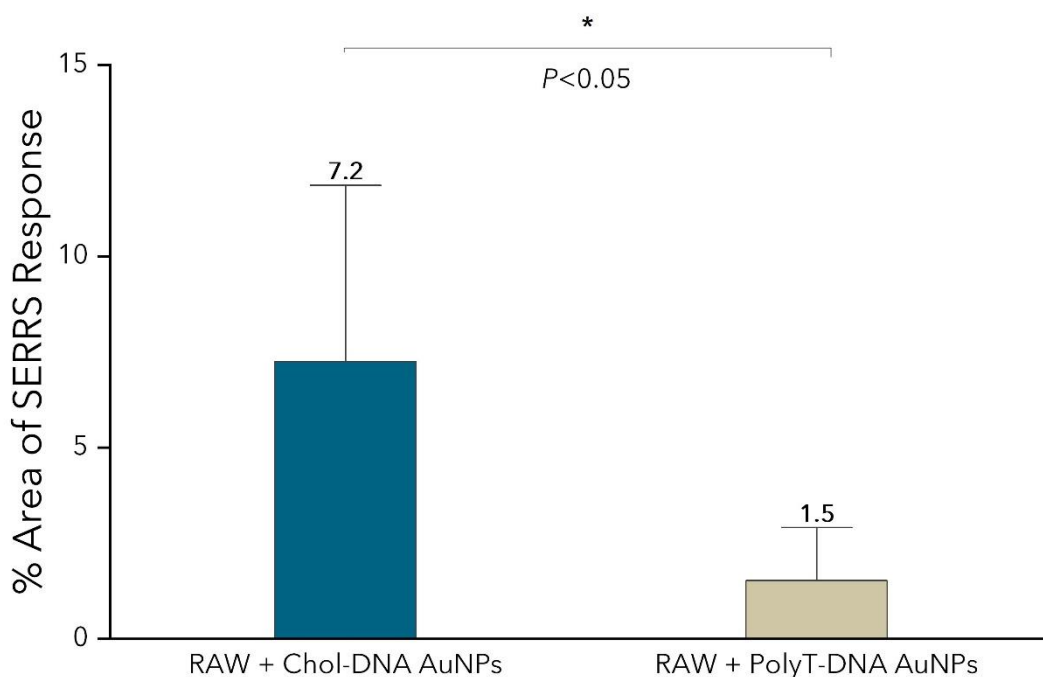
Figure 3.17: Bar chart showing the % area of relative SERRS response from chol-DNA and polyT-DNA AuNPs in RAWs. Data presented highlights the increased uptake of cholesterol modified AuNPs in comparison to the control. Data was analysed using WiRE™ software and ImageJ (from Fiji's image processing package). The error bars represent the standard deviation and the average % area for each sample is numerically presented above the error bar. Data presented is the average of 10 biological replicates each. * Statistical difference ($P<0.05$) in a Student's t-test.

Clear discrimination between the two samples again highlighted that there was considerable cellular uptake by the chol-DNA AuNPs. As previously mentioned, the only difference between this sample and the control was that the former had a cholesterol group at the end of the DNA chain. Hence, increased uptake could be attributed to this lipid group. Varying lipid moieties have been used in literature, in conjunction with other groups to increase cellular uptake. However, the efficiency alone of cholesterol has been understudied.[199,200] The results presented here reveal the efficiency of cholesterol without being anchored with other groups.

10 randomly selected cells were mapped, and the results suggest a significant increase in the uptake of chol-DNA AuNPs, compared to the

polyT-DNA AuNPs. Statistical analysis was carried out on the results to determine how significant the differences between the two samples were. Typically for biological samples, a p-value of <0.05 is statistically significant. The data obtained from the Student's t-test gave a p-value of 0.003, indicating that the data was statistically significant. Further information from the analysis and a histogram highlighting the spread in the % areas from the two samples is provided in Appendix 3.

The signals were distributed throughout the cell, however, it would be impossible to determine by 2D mapping alone where the particles were localising in the cell environment. Lee *et al.* studied a phenyl-diene cholesterol molecule in cells by stimulated Raman scattering (SRS) and determined that the molecules localised in lipid droplets (LDs), present in the cytoplasm.[201,202] This could potentially be the case here, however; further studies would need to be carried out to determine this.

The data presented by 2D mapping was successful in beginning to express the uptake of chol-DNA AuNPs. However, to confirm that the particles were ingested, 3D SERRS mapping was subsequently carried out.

3.2.3.2 3D SERRS Mapping of Cholesterol Modified Nanoparticles in RAWs

3D Raman imaging is increasingly being exploited due to its ability to output increased detailed information than a typical 2D map. The latter provides information in the x and y direction, whereas 3D mapping can acquire data in the z-direction also. Data acquisition over different focal planes (z-stacks), becomes more attractive as cells are 3D. 3D Raman and SERS mapping was first introduced by McAughtrie *et al.* who took a multiplexing approach and investigated multiple SERS nanotags simultaneously in cells.[195] Since their discovery, this technique has successfully been applied to biological samples as it not only provides confirmation of cellular uptake but can be

applied to investigate the cellular environment at a much deeper level with imaging of cellular components. Such an approach was also used by Huang *et al.* to track an AuNP through a macrophage cell to determine changes in the SERS signal as the AuNP moved through the cell. Observing certain cellular component peaks, such as the 1582 cm^{-1} peak attributed to phenylalanine and tyrosine, and the 1106 cm^{-1} peak highlighting C-N stretching, confirmed the proximity of the NP to these specific cellular components, highlighting some of the interactions the NP was making along its path.[203]

Although macrophage cells will vary in size, typically, they were found to be ~13 to 20 μm from literature.[204] Due to the difficulty in trying to determine the exact dimension of the cell in the *z*-direction, the cell was focussed and then mapped in the positive and negative *z*-direction. This would allow image sections to be acquired throughout the volume of the cell. The 3D map of a RAW cell which had ingested chol-DNA AuNPs is shown in Figure 3.18(a). Spectra obtained at various *z* planes are provided in Figure 3.18(b).

a)

b)
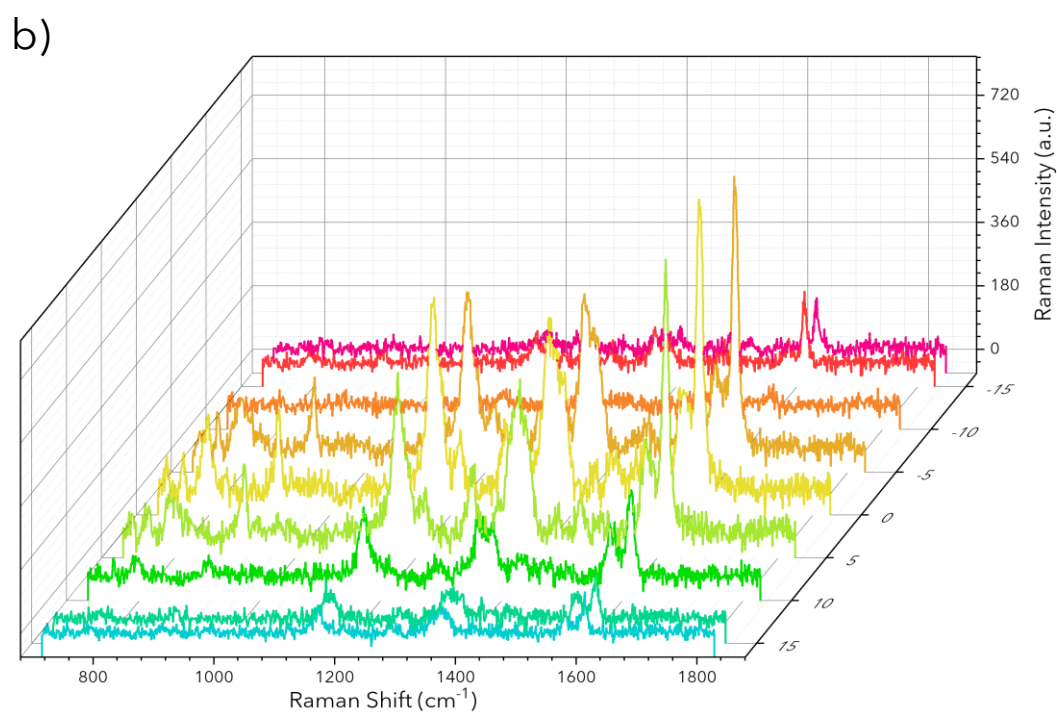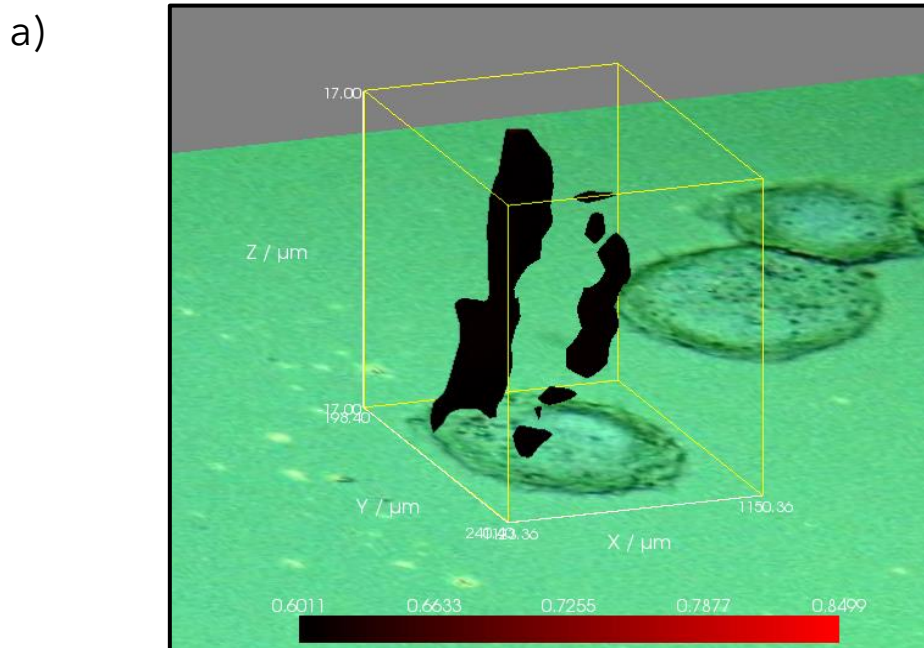
Figure 3.18: a) 3D SERRS mapping of cholesterol modified AuNPs in RAWs to confirm that MGITC signal was originating from within the cell. The yellow square box is representative of the cell in the x, y and z direction and the black false colour within the box represents the areas of MGITC signal. b) Spectra taken at various points from the depth profile and highlight signal from within the cell. All spectra were acquired at 1 second accumulation time, at 5 % laser power. Data was processed using WiRE™ software.

From the depth profile, there was MGITC signal detected at 0, 5 and -5 μm, and hence NP signal was detected from within the cell volume. The signal was considerably low because the nanoparticles were embedded within the cells, and it has been shown previously that the signal is reduced upon NP entry to the cell.[124] This was evident upon comparing the signal to the reference MGITC which was acquired on the spectrometer beforehand (Figure 3.19) It was observed that outside of the deeper depth planes, little MGITC signal was detected.

The 3D data was confirmation that the chol-DNA AuNPs were successfully ingested and by observing the area of false colour from the DCLS analysis. There was not a method of 'semi-quantifying' the signal as was done for the 2D map. Calculating the % area of SERRS response from the false colour plots would have to be carried out for each depth plane which would become tedious and time-consuming. This is another issue which needs further study to try and source a viable route for quantitation.
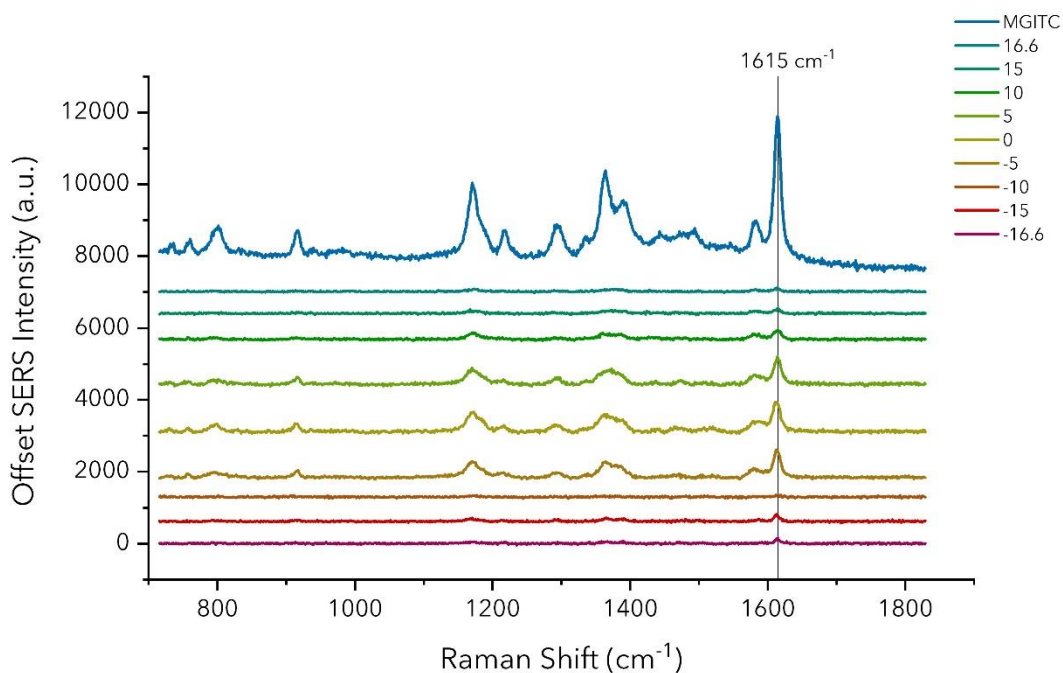
Figure 3.19: Spectra taken from various planes from the depth profile and compared to the MGITC reference spectrum. Data shows a considerable drop in signal once inside the cell. Data plotted in an offset *y*-stack using Origin®.

3.2.3.3 Investigating Spectral Changes Between Live & Fixed Cell Samples

During the fixation process, cells are immobilised in a way in which can be detrimental to their cellular molecular structure, and there is also evidence that fixing methods may alter the Raman spectra of cells in comparison to unfixed cells.[123] Kuzmin *et al.* investigated the changes to the cellular composition of HeLa cells by two fixatives; formaldehyde and chilled ethanol. Their studies highlighted that while ethanol fixation did enhance some biomolecular components, due to cell shrinkage, formaldehyde did not strongly affect the Raman spectra.[205] Live cell imaging is possible due to the weak Raman signal given by water, allowing cells to be examined within an aqueous environment, and given that cells are predominantly aqueous themselves. This proves extremely beneficial as cells can be imaged within

their normal physiological conditions, without the need for fixation, as fixing may disrupt cell membranes.

As Raman spectroscopy progresses towards becoming a diagnostic tool, developments have allowed live cell imaging to become slightly easier with the coupling of a cell incubator to the spectrometer. Allowing cells to remain in their optimum physiological conditions (37 °C and 5% carbon dioxide) also has simplified the live cell imaging process. Technically, the live cell mapping carried out here should be referred to as un-fixed cell mapping as the Raman microscope used for this work was not coupled to an incubator. However, for ease the term 'live cell mapping' will be used. To maintain cell integrity, data collection was kept to ~2 hours.

The reason for carrying out live cell imaging here, was because at first, the fixation process was drastically changing the morphology of the cell. Upon a series of optimisation steps such as changing the volume of PFA (paraformaldehyde) added, and the time this was left with the cells in the incubator, cells looked much healthier. Live cell imaging was carried out to determine that MGITC signal could still be observed from within the cell. If the cells had ablated, then no signal would be observed. Similarly, if cells had begun to shrink then enhancement of the MGITC may be observed with the significant clustering of probes. Hence, it was decided to carry out a short study in which the SERRS response would be compared to that from a spectrum acquired during 2D mapping. This would allow for a quick comparison of whether the MGITC fingerprint remained the same or if the fixation process had produced any changes. The typical signals seen from both live and fixed cells are compared in Figure 3.20. There were no changes observed in the Raman fingerprints when typical spectra from fixed and live cells were compared. Hence, it was concluded that the fixation process did not alter the MGITC fingerprint.
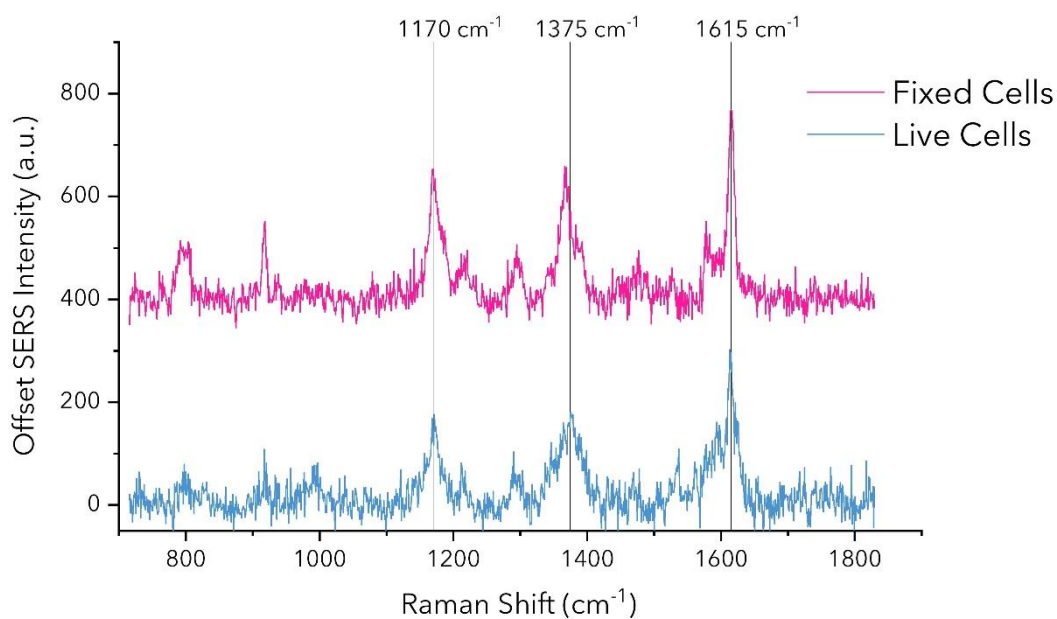
Figure 3.20: Comparison of SERRS response from fixed (pink) and live cells (blue). The peaks at 1615, 1375 and 1170 cm^{-1} were compared. All spectra were acquired at 1 second accumulation time, at 5 % laser power. Data was processed using WiRE™ software. Data plotted in an offset y-stack using Origin®.

3.2.3.4 Applying A Multiplexed Approach

An interesting review on multiplexing *in vitro* was published by Laing *et al.*, in which they outlined the simultaneous detection of varying biomolecules within a cell.[193] The 2D and 3D SERRS mapping was confirmation that the cholesterol DNA was enhancing the cellular uptake. However, it would also be interesting to observe the outcome when both chol-DNA and polyT-DNA modified AuNPs were added together. One of the main advantages with SERS is the ability to multiplex, which would allow the simultaneous detection of chol-DNA and polyT-DNA AuNPs. It was anticipated that the chol-DNA AuNPs would exhibit enhanced SERRS signal compared to its control of polyT-DNA AuNPs, in accordance with the 2D SERRS mapping results. Exploiting this characteristic would add evidence to the fact that the cholesterol modification enhanced cellular uptake. In such an attempt, a

study was carried out whereby both conjugates were added simultaneously to the same sample of plated cells. For this work, the Raman dye on the control was changed to a Raman reporter – MBA (4-mercaptobenzioc acid). This reporter was chosen as it had a Raman fingerprint distinctive to that of MGITC, and also MBA has previously been used for intracellular pH studies. In one such case, Jaworska *et al.* studied the intracellular pH of endothelial cells, in which they tagged MBA with NPs to create pH sensitive probes.[206] The chemical structure and Raman fingerprint of both MGITC and MBA are presented in Figure 3.21.
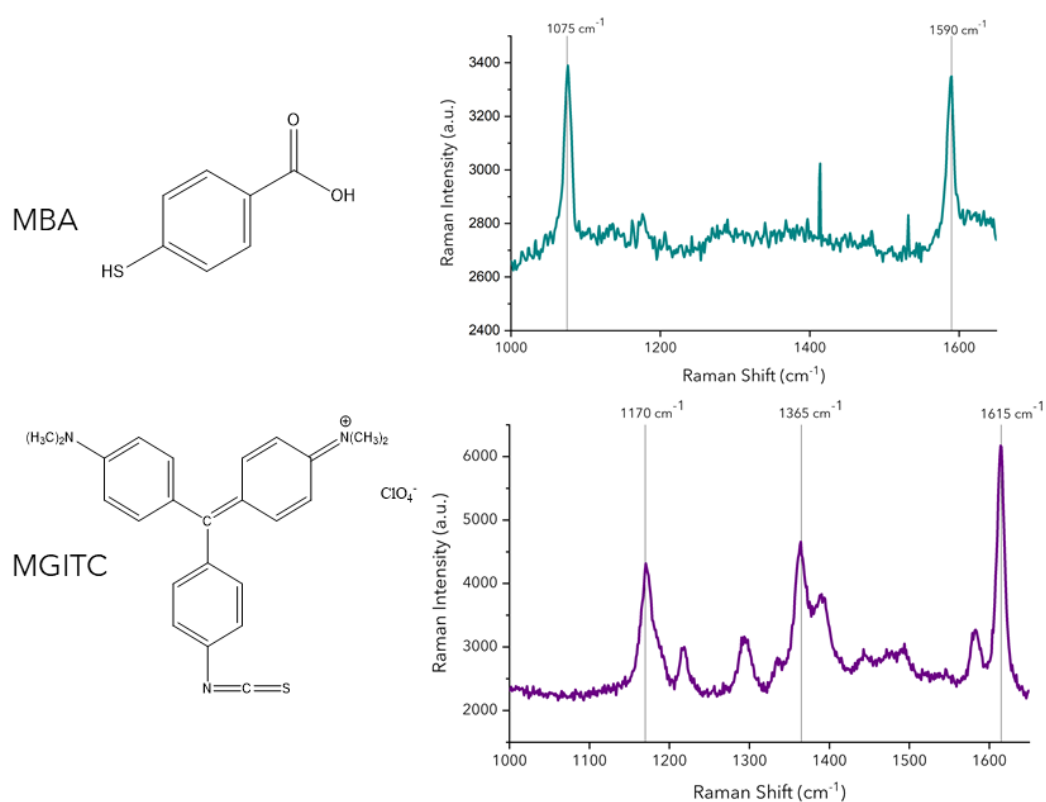
Figure 3.21: Chemical structure and fingerprints of MBA and MGITC respectively. Spectra were acquired using a Snowy Range (SnRI) Raman Spectrometer with a 638 nm laser excitation at 1 s acquisition times and 100% laser power (40mW).

With two distinctive spectra, the DCLS analysis would easily be able to differentiate between the two. MGITC has intense peaks at 1615, 1365 and 1170 cm^{-1}, which are distinctive to the peaks at 1590 and 1070 cm^{-1} for MBA. An effort was made to keep the functionalisation procedure between the two probes as similar as possible to allow the comparison to be made accurately, hence the only modification made to the control was the reporter. DNA loading and volume of salt added were kept the same. The functionalisation process is detailed in section 6.2.4 of the Experimental chapter. Optimisation studies were carried out to make sure an intense fingerprint would be observed. SERS analysis was carried out prior to 2D mapping to confirm that the signals were intense. The SERRS spectra are given in Figure 3.22.
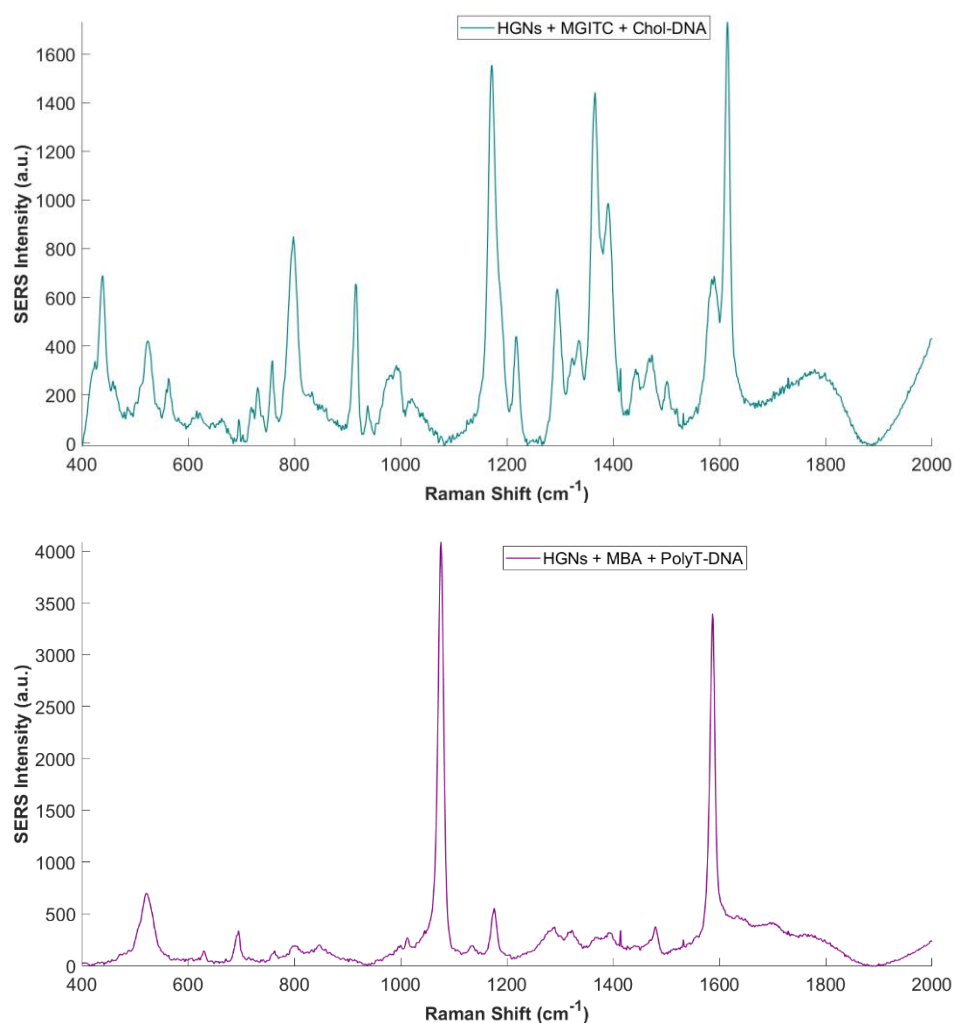
Figure 3.22: Spectra of MGITC (top) and MBA (bottom) obtained using a Snowy Range 638 nm laser excitation spectrometer prior to 2D SERRS mapping. Data collected with 1 second acquisition time and at 100% laser power (40mW). Data presented is an average of three measurement, processed using MATLAB®.

The results from the DCLS analysis were not consistent and indicated greater uptake of chol-DNA AuNPs and in some cells polyT-MBA AuNPs appeared to be dominant. At first, it was suggested that the results were potentially contradicting the previous study in which the uptake of chol-DNA AuNPs was substantially greater than its control. However, after much consideration and research, it was realised that the reporter was the issue. MBA has

extensively been used as a pH sensitive probe for intracellular studies.[206-209] In a study by Talley *et al.,* AgNPs were functionalised with MBA to investigate the changes in pH as the probes moved into the cellular environment. Their findings mentioned that these pH sensors were able to retain their robust signal when incorporated into a cell.[210] Generally, it is known that the dye/reporter intensity drops once inside the cellular space, however, if MBA can retain its intense signal then DCLS analysis would highlight a greater fit, generating a false colour plot depicting increased uptake. Another observation by this group was that these AgNP-MBA probes were forming aggregated particle clusters, again enhancing the SERS response. This corroborated with the results observed in this study as some cells exhibited considerable signal from the MBA functionalised conjugates. A typical DCLS plot is given in Figure 3.23. It should be noted that the relative intensity of the MBA spectra in Figure 3.22 and Figure 3.23 are different. Although the definite reason for this is unknown, it is thought that this may be because the spectra from Figure 3.22 was taken on the Snowy SnRI spectrometer which interrogates a larger sample volume so generally there will be more MBA-AuNPs, in comparison to a spectra taken of MBA-AuNPs from a cell sample.
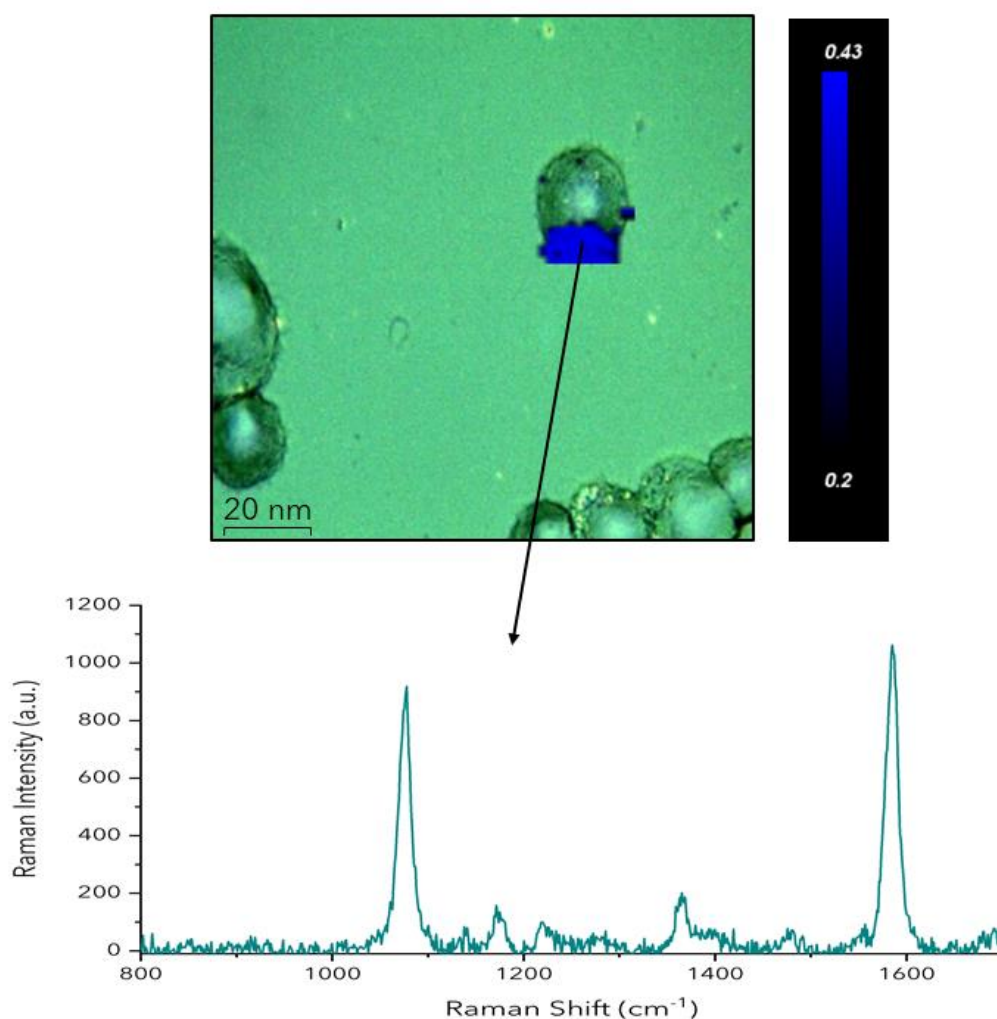
Figure 3.23: DCLS analysis of PolyT-MBA-AuNPs in RAWs, which outline aggregation within the cellular environment with the large clustering of signal observed. A typical MBA spectrum from the cell is also highlighted. All spectra were acquired at 1 second accumulation time, 5 % laser power. Data was processed using WiRE™ software.

The aforementioned pointers were attributed to the increased signal observed within the cell, and also outside the cell. The study was considered unreliable and would need to be repeated with another dye/reporter, for example, rhodamine 6G, TAMRA (tetremethylrhodamine) or Cy5 (cyanine5).[211] If the solitary issue was aggregation, then the nanoparticles could be silica-coated which would prevent aggregation. However, in this case, another Raman dye would need to be chosen and background studies

carried out to determine that it was acceptable, i.e. did not interfere or overlap with MGITC signal, for *in vitro* studies.

3.2.4 Determining Cellular Uptake of Cholesterol Modified Nanoparticles by HUVECs

The successful cellular uptake of cholesterol modified AuNPs with RAWs meant that the study could be moved forward to investigating their capabilities within HUVECs, which was another aim of this project. The process of atherosclerosis begins with the dysfunction of endothelial cell lining, where an influx of LDL-C occurs. Cholesterol modified AuNPs are essentially lipophilic and could mimic such biomolecules. However, to begin with, their interactions with these cells had to be investigated.

3.2.4.1 2D SERRS Mapping of Cholesterol Modified Nanoparticles in HUVECs

For this study, the control was changed to pegylated nanoparticles (PEG-AuNPs). These organic molecules are frequently used to coat the NP surface to provide stability and are known to be biocompatible.[212,213] As PEG-NPs have routinely been used for cell studies, it was thought to use the above as the control. This would also allow for a comparison of chol-DNA AuNPs to functionalised NPs already known in literature. The functionalisation procedure (outlined in section 6.1.3.5) was similar to that of chol-DNA AuNPs to allow comparisons to be made effectively. Analyses using extinction spectroscopy and DLS were carried out, similar to as mentioned in section 6.1.5.1. and 6.1.5.2. respectively. Data is provided in Figure 3.24 below.
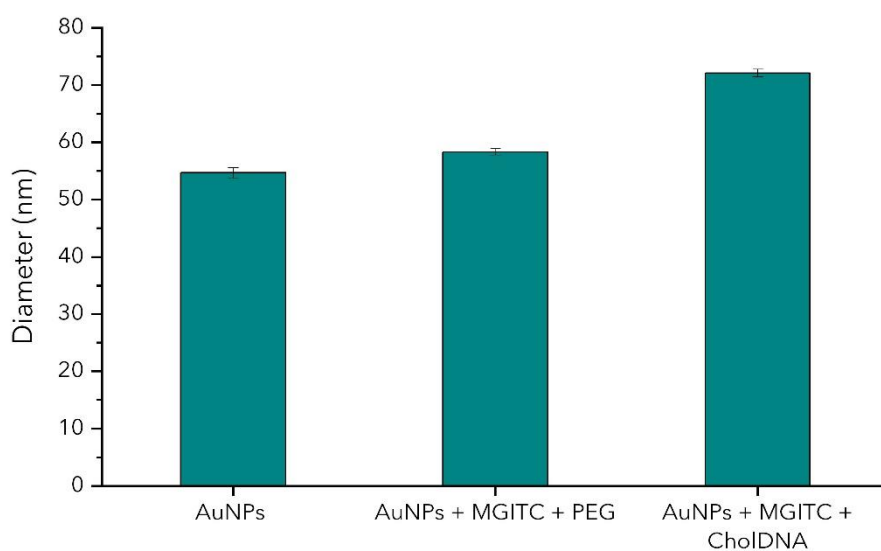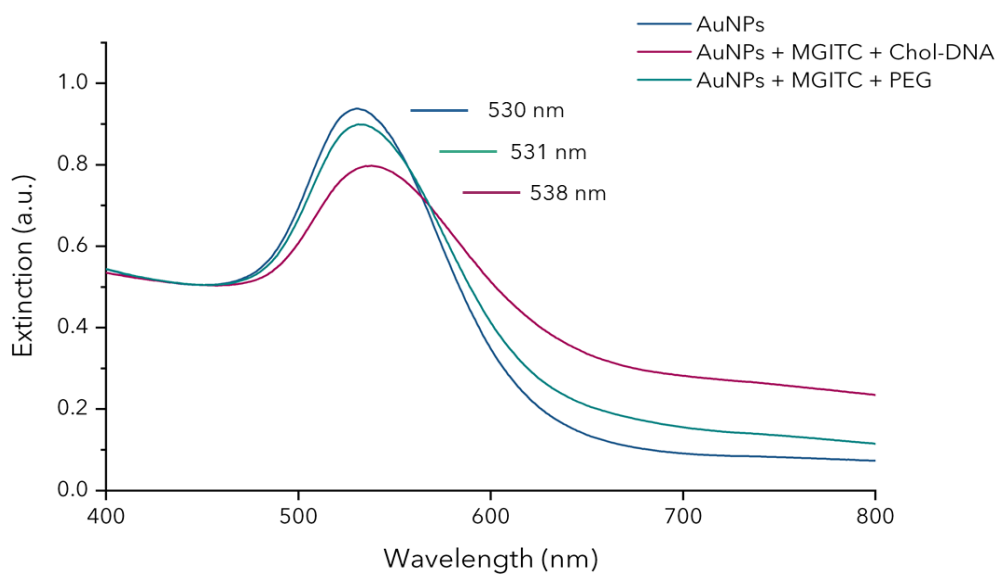
Figure 3.24: Results from extinction spectroscopy and DLS, which were used to characterise cholesterol and pegylated AuNPs and confirmed successful attachment of the PEG and DNA to the surface: (Top) Extinction spectra obtained using a scan rate of 600 nm/min and are an average of three spectra. Data normalised at 450 nm using Microsoft® Excel. (Bottom) Bar graph depicting the average diameters of the conjugates. Results presented are an average of three replicates and the standard deviation is given in the form of error bars.

The cells were initially plated at a concentration of 0.2×10^{-6} M as otherwise, they exceeded confluency after 24 hours. The method of preparing samples, mapping and analysis were kept the same as for RAWs. The only difference here was that the laser power was increased to 10% instead of 5% with the study of RAWs. This was human error, however, it was anticipated that the difference did not affect the results. This was confirmed by observing the intensities of the silica standard (Appendix 4), exhibiting negligible change to the peak intensity, hence it could be said that using the two different laser powers did not affect the results. The resulting DCLS analysis plots from chol-DNA AuNPs and PEG-AuNPs are given in Figure 3.25.
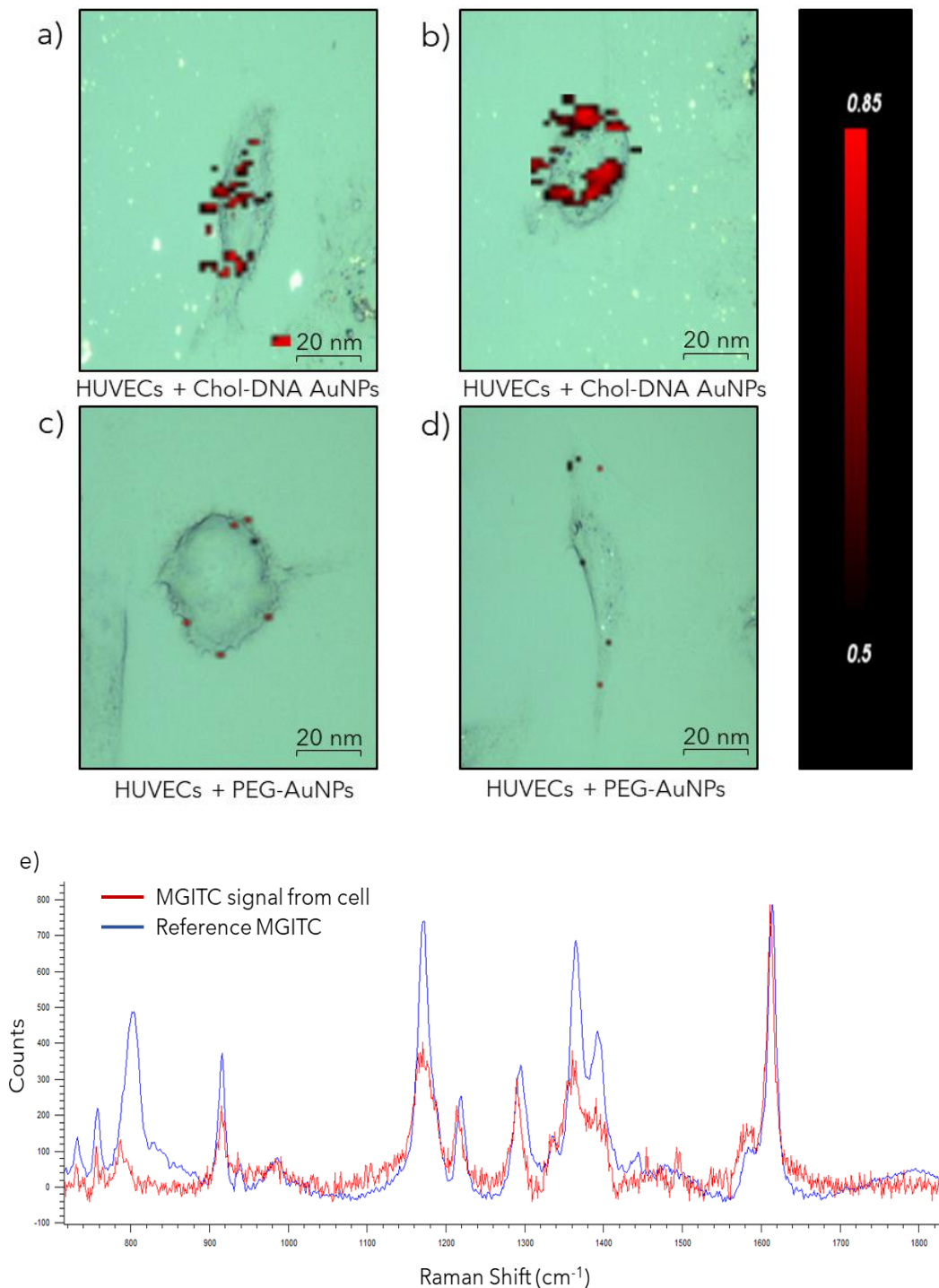
Figure 3.25: DCLS analysis of 2D SERRS mapping of functionalised AuNPs in HUVECs. a/b) HUVECs + chol-DNA AuNPs, c/d) HUVECs + PEG-DNA AuNPs. Cells mapped using a Renishaw inVia Raman confocal microscope and data processed using WiRE™ software. Maps were acquired using 1 second acquisition times and a 633 nm excitation, at a 10 % laser power. False colour images were generated post analysis using DCLS and show chol-DNA AuNPs having increased cellular uptake in comparison to the control of PEG-DNA AuNPs. e) Example spectrum of a MGITC signal observed from the cell (red), compared to the reference MGITC spectrum used for DCLS analysis (blue).

The DCLS analysis highlighted the significant uptake of chol-DNA AuNPs in HUVECs, in comparison to the control of PEG-AuNPs. It was inferred that the signal from the former was distributed throughout the cell and not localised within a specific area. Although the exact reason for the increased uptake cannot be confirmed, it can be mentioned that literature does mention the use of lipids for enhancing cellular uptake. Furthermore, lipid biomolecules such as LDL-C and fatty acids within the body have pronounced uptake with endothelial cells. The reason for the increased uptake of these biomolecules by the endothelial cells is still not entirely understood. A review by Goldberg *et al*. in which they detailed the relationship between lipids and the endothelium, mentioned that the "basic mechanism of lipid uptake and transport by the endothelium are not understood."[187] For the PEG-AuNPs, the negligible signal observed was predominantly at the boundaries of the cell and there was no localisation of signal from within the cellular environment. A study by Wang *et al*. investigated the impact of molecular weight (MW) of PEG molecules with the mechanism of cellular uptake.[214] Their research identified that PEG_{2000} and their lower MW counterparts entered the cells via passive diffusion, whereas those with higher MW, such as PEG_{5000} and $PEG_{20,000}$ enter via passive diffusion at low concentrations, and at higher concentrations via caveolae-mediated endocytosis. Despite the study not using PEG-NPs, their work confirmed that PEG_{5000} is cell penetrant. Here, we demonstrated that PEG-AuNPs were detected from within the cell volume, however, did not have a considerable uptake as the chol-DNA AuNPs.

As mentioned previously, nanoparticles in general, enter via the mechanism of endocytosis, so it was envisioned that the chol-DNA AuNPs also enter via this route.[140,183,197] Localisation cannot be determined from 2D SERRS mapping alone and would need further studies using 3D SERRS imaging.

The % area of SERRS response was also calculated for these samples, which confirmed that the chol-DNA AuNPs covered on average 16.2% area of the

cell, whereas it's control of PEG-AuNPs were only visible in 0.2% of the total cellular space (Figure 3.26). These results were collated from the 10 biological samples which were mapped at random. Analysis using a Student's t-test identified significance in the uptake, giving a *p*-value of 0.00095. The additional analyses and histogram depicting the spread of results from 10 biological samples are given in Appendix 5. Comparing the % area of SERRS response of the chol-DNA AuNPs from both the RAWs and HUVECs, it was observed that the signal within the latter was effectively doubled. HUVECs highlighted a 16.2 % area of signal in comparison to 7.2% observed from the RAWs. These results were consistent with the literature, which explained fatty biomolecules to have pronounced uptake with endothelial cells.
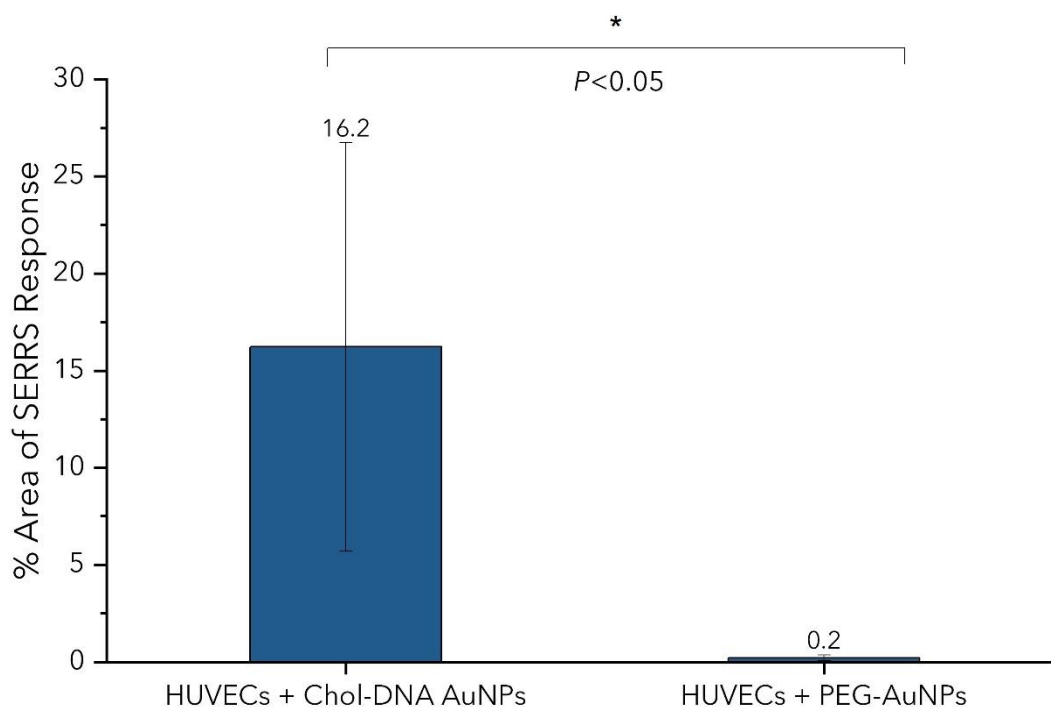
Figure 3.26: Bar chart showing the % area of relative SERRS response from chol-DNA and pegylated AuNPs in HUVECs. Data presented highlights the increased uptake of cholesterol modified AuNPs in comparison to the control. Data was analysed using WiRE™ software and ImageJ (from Fiji's image processing package). The error bars represent the standard deviation, and the % area average for each sample is numerically presented above the error bar. Presented data was the average of 10 biological replicates each. * Statistical difference ($P<0.05$) in a Student's t-test.

In Figure 3.25(e), which depicted a typical MGITC spectrum from within the cellular space, vibrational changes were observed. These included shifting of vibrations in the 700 – 800 cm^{-1} region and the 1295 cm^{-1} peak, additionally exhibiting the reduced intensity of the 1395 cm^{-1} peak. These were specific to this particular spectrum; however, changes were observed in the majority of the collected vibrational fingerprints. Although it is impossible to meticulously assign the reasoning for each change, a general statement regarding changes can be made. Once the chol-DNA has entered the intracellular environment, it may interact with other cellular components, for example with nucleic acids at ~788 cm^{-1}.[215] These interactions may change the orientation of the MGITC on the surface. Primarily, the MGITC is

attached to the surface of the NP via the thiol moiety, however, in some cases the dye may be electrostatically linked to the surface by interactions with the 6-membered rings and the NP surface, keeping the dye in close proximity. In such a case, interactions with other cellular components could result in orientational changes, potentially giving rise to spectral changes. Another reasoning may be attributed to changes in pH. However, this is unlikely. This is because a study was undertaken by Qian *et al,* in which they carried out pH-dependent studies with MGITC. By observing no SERS changes over a range of pH 2 to pH 13, they concluded that this molecule is not responsive to pH changes under acidic or basic conditions. They reasoned that the isothiocyanate group on the MGITC is irreversibly stabilised or 'locked' on the surface which is not sensitive to pH changes.[167]

In striving to enhance the understanding of the interactions between the chol-DNA AuNPs and cellular component's, one approach which could be taken is similar to that taken by Fujita's group. They used 3D SERS imaging to track AuNPs in a living cell, by combining a confocal Raman spectrometer with dual-focus dark field microscopy, which allowed them to simultaneously detect the motion of the probe and the SERS spectrum.[203] From their spectral outputs, they were able to show the interactions with differing intracellular components by observing peaks which correlated to them. In addition to this, as they possessed the nanoparticle trajectory and the molecular environment, they could assign the collected spectral information to the point it was collected from, and in return were able to display RGB (red green blue) colour maps of the molecular distribution on the course of the nanoparticle. If such an approach was applied here, it could enhance the understanding of the route these chol-DNA AuNPs take.

After the 2D SERRS mapping, 3D data was also acquired. These studies were important because there was extracellular signal observed from the chol-DNA AuNP samples, so it was vital to determine that the signal observed

within the cell (from the DCLS plot) was in fact inside the cell and not only from the surface of the cell.

3.2.4.2 3D SERRS Mapping of Cholesterol Modified Nanoparticles in HUVECs

Endothelial cells are generally known to be relatively thin and elongated. Their dimensions can be 50-70 µm long, 10-30 µm wide and have a depth of 0.1-10 µm.[216] Selecting the range of depth to map can become troublesome as it's not possible to determine the cell's boundaries. In saying that previous studies of mapping the Raman cellular response from HUVECs were carried out over a 4 µm range.[124] Hence, this was chosen as the depth range for these 3D studies also (-2 to +2 µm). Although, due to the software, mapping was recorded between +1.6 and -1.6 µm in the *z*-direction, hence the total depth plane mapped was 3.2 µm. The false colour plot from the DCLS analysis is given in Figure 3.27, in which the area mapped is shown and the location of the signal within. The yellow box represents the volume mapped. Figure 3.28 provides the cross-sections of the area mapped allowing an enhanced understanding of signal locality.
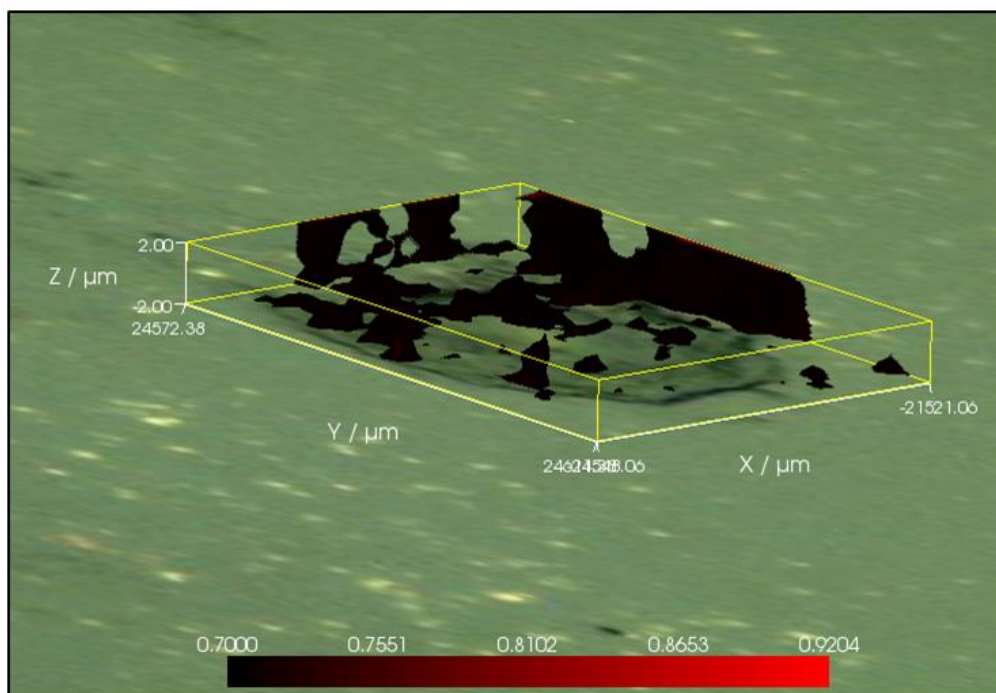
Figure 3.27: 3D SERRS mapping of cholesterol modified AuNPs in RAWs to confirm that MGITC signal located within the cell. The yellow square box is representative of the cell in the *x, y* and *z* direction, and the black false colour within the box represents the nanoparticles. The depth profile measured a total 3.2 µm. Mapping was carried out using an inVia Raman confocal spectrometer with a 633 nm laser excitation, at 10% laser power and 1 s acquisition times. Data was processed in WiRE™.
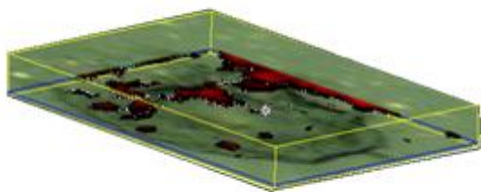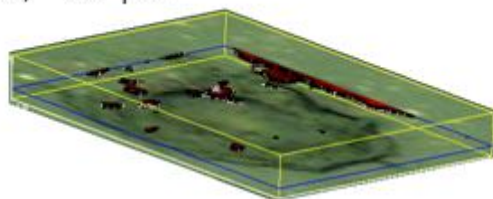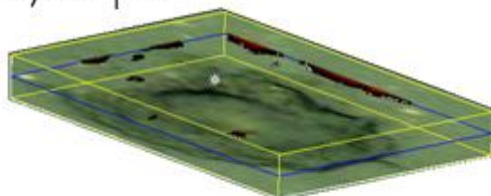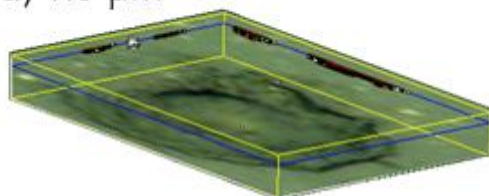
Figure 3.28: Cross-sections of the 3D map of chol-DNA AuNPs in HUVECs at multiple depth planes: a) -1.6, b) 1.0, c) 0.0, d) 1.0 and e)1.6 µm. The yellow square box is representative of the cell in the *x, y* and *z* direction, and the black false colour within the box represents the location of the MGITC signal. The depth profile measured a total 3.2 µm. Mapping was carried out using an inVia Raman confocal spectrometer with a 633 nm laser excitation, at 10% laser power and 1 s acquisition times. Data was processed in WiRE™.

The considerable signal observed from within the cell correlated well with the results obtained from the 2D mapping, which again highlighted that there was pronounced uptake of the chol-DNA AuNPs. There is evidence of intracellular NP signal in the -1.6 μm slice. As the focus was moved through the volume of the cell (-1.6 to +1.0) there is signal detected from within the cell. At +1.6 μm, a little signal is detected. MGITC signal was taken from each section (Figure 3.28) and plotted as shown in Figure 3.29.
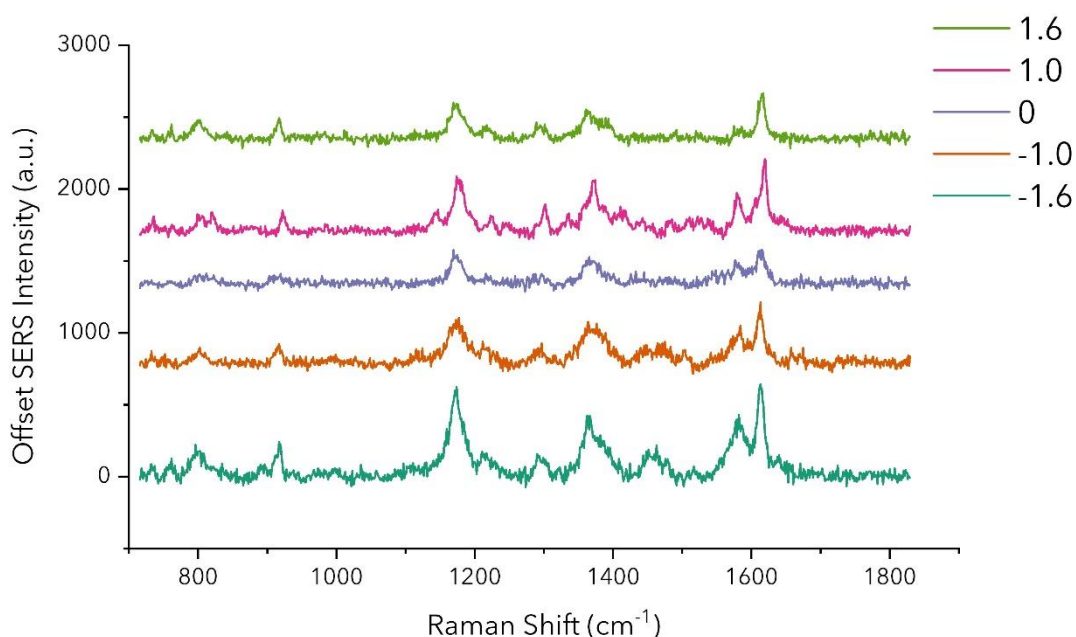
Figure 3.29: Spectra taken at various points from the depth profile. All spectra were acquired at 1 second accumulation time, at 10 % laser power. Data was processed using WiRE™ software and then plotted in an offset *y*-stack using Origin®.

MGITC signal was observed at each μm taken from the depth profile, which potentially confirms that the total area mapped was the cell itself. This conclusion is partly drawn from the fact that when the 3D mapping of chol-DNA AuNPs in RAWs was carried out (3.2.3.2), the mapping area was an overestimation of the total cellular space and there was no MGITC signal seen from certain depth planes. Another point to notice here is that the

signal from -1.6 μm was intense in comparison to the rest and it could be suggested that this specific probe may be close to the cell membrane.

As repeatedly mentioned in the sections of 3D mapping, in this chapter, a major limitation with 3D SERRS mapping is the inability to co-register the SERRS signal with the cell signal. An effort was made to overcome this limitation. It was thought that if the MGITC signal was co-localised with the cellular signal then this could determine that the SERRS response was definitely from within the cell. Raman mapping has been used to map cellular components, which typically include: nucleic acids at 788 cm^{-1}, phenylalanine at 1004 cm^{-1} and the CH_2 stretch of the lipids at 2850 and 2930 cm^{-1}.[217-219] Majzner *et al*. were able to illustrate the 3D distribution of the biochemical and structural components of a single endothelial cell, and also a cross-section of a vascular wall, in an attempt to explore their heterogeneity.[124] By exploiting both depth profiling and 3D projection, they were able to present distributions of cellular components within the intracellular space. This was done by taking spectra in the high and low wavenumber regions to outline the presence of components such as lipids and nucleic acids respectively. By integrating the Raman intensity in the 2800 – 3020 cm^{-1} region of the cell, they were able to show cell area and depth in a series of chemical images.

In an attempt to co-localise the SERRS signal with the cell signal, point spectra were taken to try and locate peaks attributing to nucleic acids and lipids. Under the same conditions as mapping (1s acquisition time and 10% laser power) no nucleic acid or lipid peaks were observed so the conditions were increased to 10 s and 50% (*ca. 2.66 mW*) respectively. Again, cellular component peaks could not be observed, and it became apparent that the reason for this was because the MGITC signal was much stronger due to being in resonance (Figure 3.30(a)). At 2900 cm^{-1} there was a broad peak, which may be the from the glass coverslip (Figure 3.30(b)). At these conditions, the cells burnt, likely due to the decomposition of the NPs at

elevated laser power. Co-localisation would be a viable solution however, it was not possible in this particular case due to the intense dye fingerprint.

a)

b)
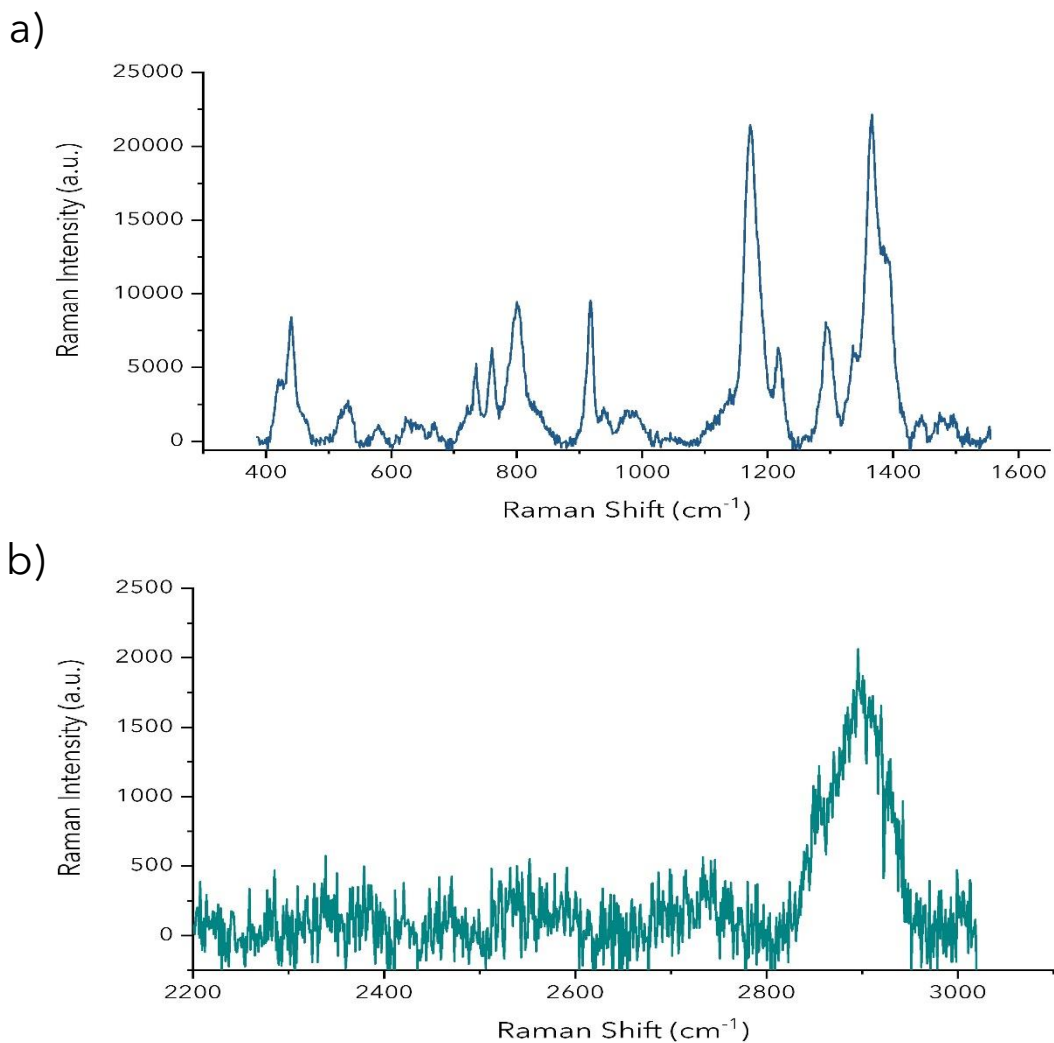
Figure 3.30: Point spectra taken over a range of wavelengths (400 – 3000 cm⁻¹) to observe vibrational outputs from cellular components. (a) Spectra of an intense MGITC fingerprint drowning typical nucleic acid peaks at 788 cm⁻¹. b) Spectra in the high wavenumber region, which would contain lipid peaks, yet only glass signal observed. Spectra taken on the inVia Raman confocal spectrometer, with a laser excitation of 633 nm, a 50% laser power and at a 10 s acquisition time.

As mentioned by Majzner *et al.,* 3D Raman imaging highlights great potential for applications in biomedical research and medical diagnostics.

However, there is a need in developing an appropriate methodology of this technique which also needs to be standardised.[124]

3.2.5 Cytotoxicity Evaluation of Cholesterol Modified Nanoparticles in HUVECs

It was pivotal to understand whether the chol-DNA AuNP probes displayed any toxicity effects, as this would be detrimental once in an *in vivo* setting. Trypan blue has been routinely used as a cell stain to assess cell viability. It acts by staining dead cells with a blue colour, as these cells have a porous membrane through which the dye can penetrate through. Cells were plated routinely in 6-well plates, and the conjugates were added as they would for mapping studies. Thereafter, in place of the fixation process, cells were detached from the plates and added to Trypan blue solution in a ratio of 1:5 respectively and counted to determine the cell viability. Data is presented in a bar chart below (Figure 3.31), highlighting the cell viabilities of both chol-DNA and PEG AuNPs. Correlating cell counts are provided in Figure 3.31(b).
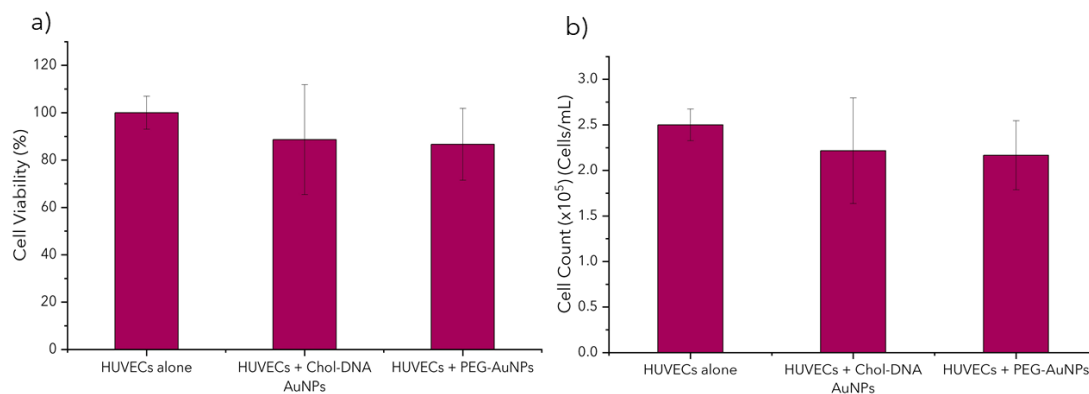
Figure 3.31: a) Cell viability studies of chol-DNA AuNPs and PEG-AuNPs in HUVECs, which show the non-toxic nature of both conjugates to cells. Viability studies were carried out using the Trypan blue staining and counting method. Experiment was carried out in triplicate with three replicates of each sample taken. The standard deviation is given as error bars. b) presents the cell counts from each study. b) respective cell counts from the studies.

The cell viabilities were constant to within experimental error. PEG-AuNPs displayed no signs of toxic behaviour with an 87% cell viability. The chol-DNA AuNPs had an 89% cell viability, which again displays a non-toxic nature. The reason for the decrease in viability may be due to pipetting errors. The only route to overcoming this issue would be to increase the number of samples.

Another approach which was used to measure the level of toxicity is a live/dead® staining assay. Briefly, cells are incubated with their nanotags. Subsequently, cells are stained with green- fluorescent Calcein AM and red-fluorescent ethidium homodimer-1 (EthD-1) stains. Calcein AM indicates intracellular esterase activity and EthD-1 indicates loss of plasma membrane integrity.[220] Using fluorescence microscopy, observing a green colour would highlight cell viability in comparison to a red colour, which would correspond to non-viable cells. From this study (Figure 3.32) it was observed that both chol-DNA AuNPs and PEG-AuNPs exhibited good biocompatibility as they maintained a green colour, conveying cell viability.

Positive and negative controls were also used. In the positive control, bare HUVECs, upon staining outlined cell viability. For a negative control, cells were exposed to 4% PFA (fixing solution) and 0.01% Triton-X (permeabilising solution). These cells were non-viable upon staining red in colour.
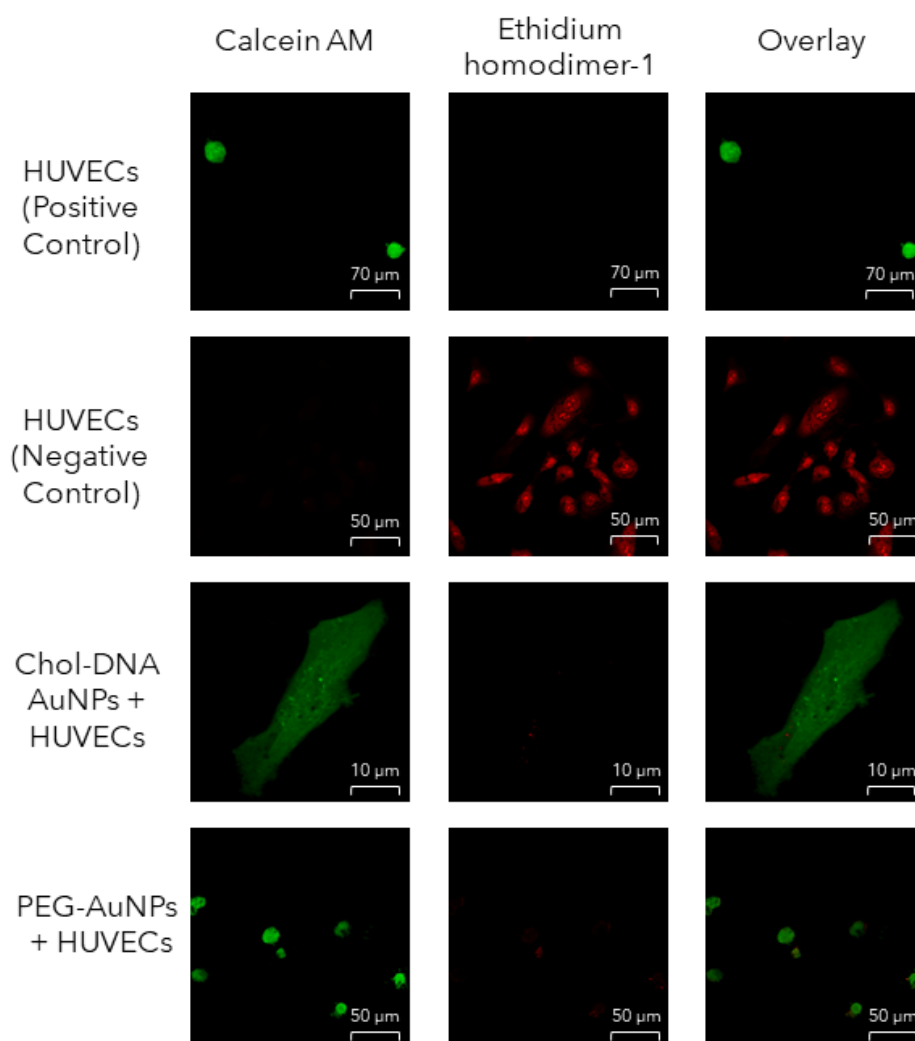
Figure 3.32: Live/Dead® viability assay kit used to carry out cell viability studies, in which the Calcein AM dye stained live cells green, and the EthD-1 dye-stained dead cells red. Study exhibited non-toxic nature of chol-DNA and PEG AuNPs. Positive and negative controls were also carried out. Study is representative of three repeats.

3.2.6 Concluding Remarks

Functionalised AuNPs from section 3.1.3.2 have been investigated in RAW and HUVEC cells using SERRS. The first study saw the successful uptake of these chol-DNA AuNPs in RAWs with an average of 7.2% SERRS response from the cellular volume when compared to 1.5% observed from the control of polyT-DNA AuNPs. Statistical analysis was carried out in the form of a Student's t-test which typically outlines statistical significance between two data sets. 3D SERRS mapping was then carried out to determine that the SERRS response was from within the cell and not from the cell's surface. The depth profile exhibited both intracellular and extracellular MGITC signal. Live cell mapping was also carried out to determine that the fixation process was not changing the morphology of the cell, ablating or shrinking it, which could potentially alter the vibrational fingerprint. This study outlined no changes to the vibrational spectra. Studies were concluded with attempts to multiplex using both conjugates in the same sample of cells. This study was unsuccessful as the reporter used on the control was pH sensitive and also aggregated within the intracellular environment, which resulted in a considerable signal being observed from the DCLS plot. It would be interesting to carry out multiplexing using another Raman dye/reporter, which may pose for future studies.

The second set of *in vitro* studies investigated the uptake of these fatty AuNPs within endothelial cells to gain an enhanced understanding prior to moving forward with photothermal experiments. A similar approach was taken as with RAWs in that 2D SERRS mapping was carried out first which exhibited increased uptake of the chol-DNA functionalised NPs vs. control NPs. The average % area of SERRS response from the cells was found to be 16% in comparison to a negligible 0.2% from the PEG-AuNPs, which served as the control. The cholesterol conjugates also exhibited enhanced uptake in comparison to the RAWs. This correlated with literature, where it was found that fatty biomolecules had enhanced uptake in endothelial cells. 3D

studies also highlighted the increased MGITC response from within the cell. During this study, an attempt was made to try and overcome the limitations of 3D depth profiling. Typically, it is impossible to select the exact area of the cell. The probability that extracellular space is selected is high. It was thought that by co-localising the SERRS response to that of the cellular fingerprint could determine that the area mapped was indeed the cell. However, point spectra were taken in attempts to observe the nucleic acid and lipid peaks at 788 and 2930 cm^{-1} respectively highlighted that it was impossible to do so. This was because at low laser power the cell signals could not be observed and when the laser power and acquisition time were increased, the MGITC signal was intense so no cellular component peaks could be observed. Similarly, the lipid peak was potentially masked by the glass background. To overcome the issue with glass interferences, CaF$_2$ slides can be used, which in the future can be utilised. Lastly, cytotoxicity studies carried out using a Trypan blue staining method and a live/dead® staining assay declared these conjugates to be non-toxic.

Although slight modifications were made between mapping in RAWs and HUVECs, a general statement could be mentioned in terms of their results. Chol-DNA AuNPs had pronounced uptake in endothelial cells, in comparison to the macrophages. This is in line with the literature, in which it's stated that fatty biomolecules are readily up taken into endothelial cells.

Moving forward, it would be interesting to determine where the chol-DNA AuNPs reside within the cellular space. Also, at present, the technique is limited because it is not as yet possible to co-register the cell signal with the SERRS signal from the NPs. Another limitation is the quantification of nanoparticles within the cell. At present, this is not possible to do so. Although this work saw a 'semi-quantitative' approach being used, much work needs to be done in trying to define a pathway for quantifying nanoparticles in cells, especially for 3D mapping.

4. Cholesterol Modified Nanoshells as Photothermal Agents for CVD

4.1 Chapter Introduction

In an effort to understand whether cholesterol modified nanoparticles could be utilised as photothermal agents, the core (nanoparticle itself) would need to have a LSPR in the NIR region (biological window), as they would be anticipated for *in vivo* studies.[221,222] Hollow gold nanoparticles (HGNs) were chosen as their LSPR can be tuned to the NIR region, and have also shown pronounced photothermal capabilities, as will be subsequently discussed.[223,224]

One of the first nanoshell fabrication methods was pioneered by Halas and co-workers in 1998,[225,226] which involved a dielectric core particle being decorated with gold-binding ligands, followed by the covalent linkage of AuNPs acting as nucleation sites. Finally, additional gold reduction in solution at these sites completed the shell. Over the years several additional synthesis methods were devised. And today, sacrificial galvanic replacement of cobalt NPs or the templated galvanic replacement reaction of silver for gold methods are predominantly used.[227]

The templated galvanic replacement reaction involving silver and gold was first reported by Sun *et al.*, who were one of the first groups to synthesise metallic HGNs via this simple, versatile route.[226,228,229] In essence, AgNPs are used as the precursor and when gold salt is added, the difference in redox potential between the gold salt and silver results in reduction and oxidation of the two respectively. Typically, this method synthesised nanoshells in the range of 20 to 50 nm and the LSPR can be tuned to 800 nm.[227] Sun *et al.* also highlighted that the morphology of the precursor (AgNPs), dictates the

shape of the hollow nanostructure and hence, they demonstrated the preparation of hollow tubes, cubic boxes, and triangular rings, etc. Interestingly, they mentioned that this method would be applicable for the preparation of other metallic shells using platinum and palladium instead of gold salt.

Although the aforementioned method was probably the most widely used route, the sacrificial galvanic replacement of cobalt NPs also became popular. This alternative approach was introduced by Liang *et al.,* whereby cobalt NPs were used as the sacrificial core, and by tuning the stoichiometric ratio of chloroauric acid (HAuCl$_4$) and reducing agent sodium borohydride (NaBH$_4$), the LSPR could be shifted in the region of 526 to 628 nm.[230] Later, Schwartzberg *et al.* added that the particle size and thickness of the shell could be adjusted with modifications to the cobalt template and the amount of HAuCl$_4$ added, effectively tailoring the LSPR from 550 to 820 nm (Figure 4.1).[231] In another study carried out by Xie *et al.,* it was demonstrated that the LSPR could be tuned up to 1320 nm, again highlighting the versatility of such nanostructures.[59]
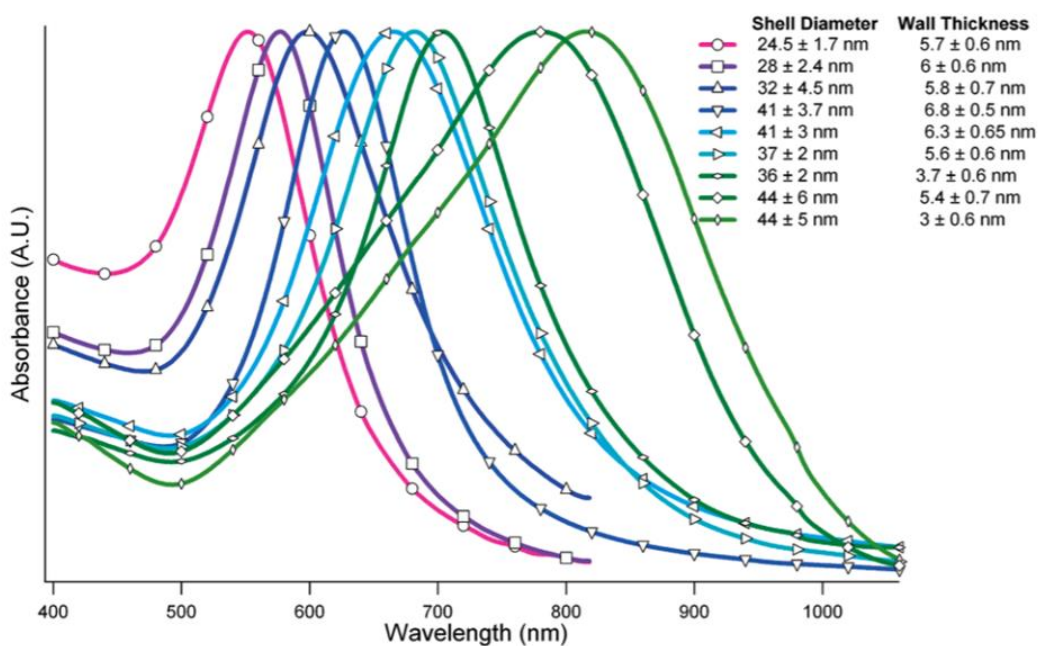
Figure 4.1: The work of Schwartzberg *et al.* depicting the extinction spectra of nine HGN samples with varying shell diameters and wall thicknesses. In this work the LSPR was tuned in the region of 550 to 820 nm. Reprinted (adapted) with permission from *A. M. Schwartzberg, T. Y. Olson, C. E. Talley and J. Z. Zhang, J. Phys. Chem. B, 2006, 110, 19935–19944.* Copyright © (2020) Americal Chemical Society.

Since their discovery, HGNs have been applied in biomedical imaging,[232] photothermal therapy (PTT),[233] and drug delivery[234] (Figure 4.2). The optical properties of HGNs hold significant biological importance because of their ability to tune the LSPR into the NIR region (~700-1100 nm), which is referred to as the 'biological window.'[221,222] The depth penetration of photons is limited in biological tissue due to the inherent absorption and scattering by inhabitants such as water and blood. These fluids, however, have reduced scattering and absorption in the near-infrared region, providing a relatively transparent optical window for bioimaging.[59,235]

As mentioned, another remarkable capability of HGNs is their photothermal abilities, which allows them to act as photothermal agents in a profusion of studies. This is attributed to the fact that the shell has a low thermal mass

meaning its ability to absorb and retain heat energy is low, consequently enabling them to quickly dissipate heat to their surroundings.[223,224] This propensity of theirs has allowed them to be utilised in tumour ablation studies. Lu *et al.* conjugated HGNs with NDP-MSH, a potent agonist of melanocortin type-1 receptor (MC1R) overexpressed in many melanoma cells.[233] Thereafter, they successfully exhibited their potential to mediate targeted photothermal ablation of melanoma. In another study by Hirsch *et al.,* HGNs were incubated with human breast carcinoma cells, which upon irradiation were ablated; evident through fluorescent viability staining.[236]

In drug delivery, HGNs have been used as drug carriers owing to their cavity structure. Encapsulating drugs within the hollow core of the HGN allows for targeted delivery and good biocompatibility.[227] Additionally, they are used to transport genes. In one such case, Lu *et al.* delivered small interfering RNA (siRNA) to tumour cells by coupling these together with folic acid to HGNs. At the site of interest, the heat was used to detach these from the nanoshells.[237]

Preceding examples highlight the immeasurable proficiency of HGNs. Their positive contributions to varying areas of interest enable them to be utilised in forthcoming studies, in particular with PTT for various diseases. However, an area that is minimally linked with HGNs is that of CVD, envisioning that their bright future will see this gap being reduced also.
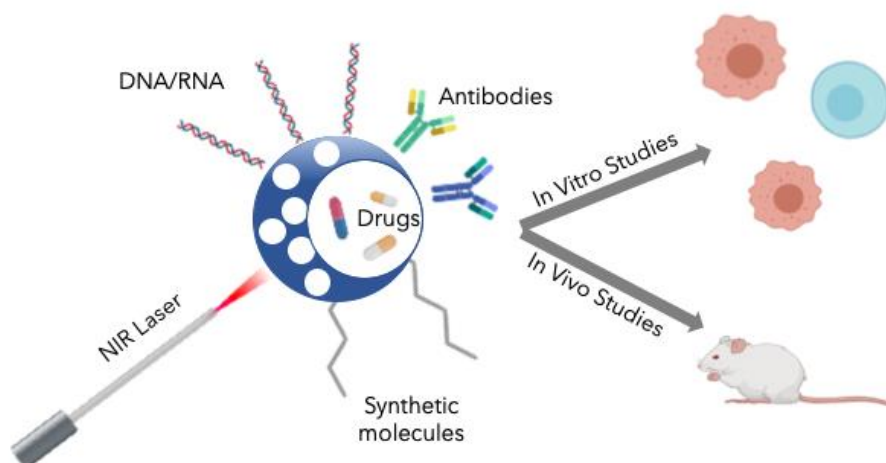
Figure 4.2: Schematic depicting the plethora of roles of HGNs. These can be functionalised with various moieties on the surface, acting as drug carriers and photothermal agents, for *in vitro* and *in vivo* studies. Schematic is not drawn to scale.

4.2 Chapter Aims

With the pronounced uptake of chol-DNA AuNPs in endothelial cells, it was thought they would be able to mimic LDL-C and hence be used as photothermal agents for targeting atherosclerotic plaques. Moving forward in investigating the use of cholesterol modified nanoparticles as photothermal agents, the core (the nanoparticle itself) was required to be optically active in the NIR region. This chapter aimed to investigate hollow gold nanoparticles (HGNs) as the 'core' for these photothermal agents and to deduce whether cholesterol modified HGNs (chol-DNA HGNs) were able to show enhanced cellular ablation in comparison to bare HGNs. HGNs were chosen due to their facile synthesis and ability to shift the LSPR, as well as being desirable nanostructures for PTT. Due to their thin shells having a low thermal mass, HGNs can efficiently dissipate heat to the surrounding

tissues.[223,224] It was equally important to tune the LSPR to the excitation wavelength of the irradiating laser, maximising the heating.

Once HGNs with the desired LSPR were synthesised, they were functionalised with MGITC and chol-DNA and incubated with cells. Thereafter, photothermal ablation studies were conducted using an in-house set-up, subsequently determining cell death by Trypan Blue staining studies. These studies compared the heating capabilities of bare AuNP to HGNs, and also bare HGNs to functionalised HGNs. 2D SERRS mapping was also carried out to determine the uptake of the functionalised HGNs in HUVECs and the % SERRS response per cell area was also calculated using DCLS plots.

4.3 Results and Discussion

4.3.1 Hollow Gold Nanoparticles

4.3.1.1 Synthesis of Hollow Gold Nanoparticles

The method of HGN synthesis used herein was different from the traditional approach of using a Schlenk line. A method of silver template replacement was first introduced by Xia's group in which a wide range of morphologies of AgNPs were exploited to synthesise gold nanoshells.[238] In this chapter, the HGNs were synthesised using an adapted protocol from that previously reported by Goodman *et al.*[224] The synthesis is a facile, benchtop reaction, which involves a galvanic replacement reaction between a metal salt solution and a colloidal metal solution. The AgNPs have a lower reduction potential in comparison to the higher reduction potential of the gold salt, hence a redox reaction occurs, resulting in the formation of the HGNs; 0.99 V for $[AuCl_4]^-$/Au and 0.80 V for Ag^+/Ag compared to the standard hydrogen electrode (SHE).[224] The redox half equations and the overall balanced redox equation are given in Figure 4.3 below:

$$\text{Anodic Reaction: } Ag \rightarrow Ag^+(aq) + e^-$$

$$\text{Cathodic Reation: } AuCl_4^-(aq) + 3e^- \rightarrow Au(s) + 4Cl^-(aq)$$

$$3Ag(s) + AuCl_4^-(aq) \rightarrow Au(s) + 3Ag^+(aq) + 4Cl^-(aq)$$
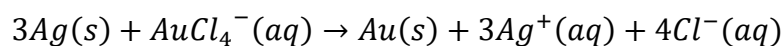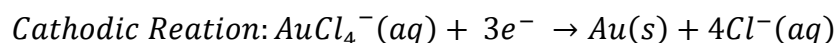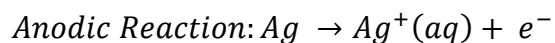
Figure 4.3: The redox half equations and the overall balanced equation for the galvanic replacement synthesis between Au and Ag.

Upon reduction of the gold salt on to the AgNPs, the latter begins to oxidise, creating pinholes in the alloy shell (Au) resulting in a hollow structure, known as the Kirkendall effect.[239,240] Thereafter, through the Ostwald ripening process, the shell reshapes, moving towards the dealloying stage, in which the Au ions are reduced to atoms, forming the gold shell around the template. At this point, the Ag is completely oxidised, and only pure Au remains.[224] A schematic depicting the stages of HGN formation is given in Figure 4.4.
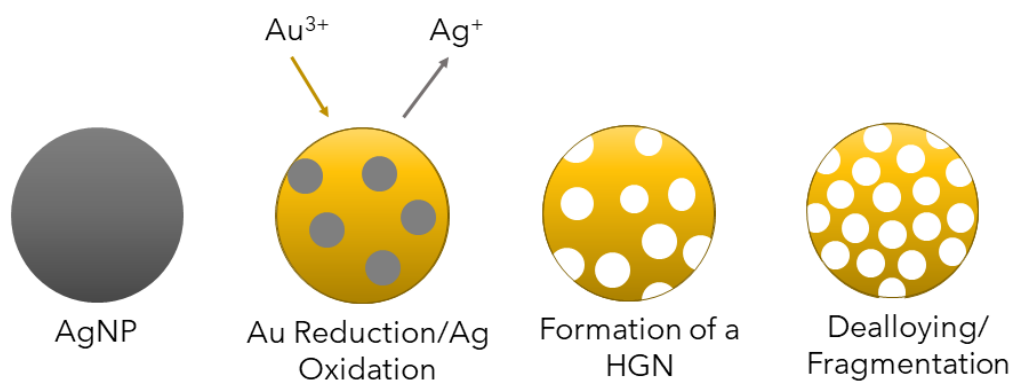
Figure 4.4: Schematic illustrating the stages of HGN synthesis by galvanic replacement. As gold salt is added to the AgNP, Au^{3+} is reduced and Ag^+ is oxidised. Mass flows from the central region via the process of Ostwald Ripening and the HGN begins to take shape. As the Ag^+ is completely oxidised, only pure Au fragments remain. Schematic is not drawn to scale.

For the sacrificial core, hydroxylamine AgNPs were used. A facile method reported by *Leopold et al.*[241] was adapted to achieve these stable AgNPs. The synthesis was a rapid, benchtop reaction involving the addition of sodium hydroxide and hydroxylamine hydrochloride, followed by silver nitrate, under constant stirring. Figure 4.5 provides the extinction spectrum of AgNPs synthesised with a λ_{max} of 401 nm and a narrow FWHM of 73 nm, indicating the monodispersity of the nanoparticles. The DLS data indicated an average diameter of 73.5 ± 2.4 nm. The zeta potential, as mentioned previously, provides information on the NP surface charge, which indicates the stability of the colloid. AgNPs exhibited a surface charge of – 39.3 ± 1.1 mV, which was greater than the proposed stability value of ± 30 mV,[155] hence confirming the stability of the core template.
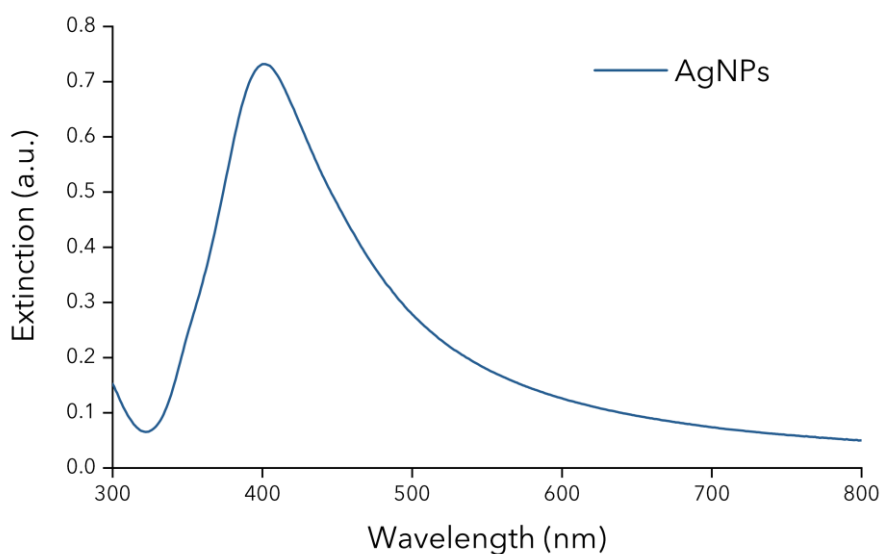
Figure 4.5: Extinction spectrum of hydroxylamine AgNPs used for the synthesis of HGNs. Spectrum acquired using a 1 in 10 dilution, at a scan rate of 600 nm/min.

4.3.1.2 Tuning the LSPR of Hollow Gold Nanoparticles

HGNs are preferential nanostructures due to their tunable LSPR, which can be shifted for a specific application. Tuning the LSPR to a particular wavelength in the biological window (700 - 1100 nm) or shifting to resonate with a specific laser excitation source is most often beneficial for the application.

The shift in LSPR is attributed to the change in the ratio between the NP core diameter and the shell thickness.[228,242,243] An increase in the core: shell aspect ratio would increase the nanoshell diameter, resulting in a bathochromic shift (red shift) of the plasmon resonance, evident with a colour change from a vibrant blue to a grey-blue. Similarly, decreasing the ratio would result in a hypsochromic shift (blue shift), which would yield HGNs of red/purple colour.[231] In an effort to shift the LSPR further into the biological region, the core: shell aspect ratio was adjusted to push the LSPR to longer wavelengths. Various ratios were investigated and batches of HGNs ranging in LSPR's from 718 – 850 nm were synthesised, as shown by their extinction spectra in Figure 4.6.
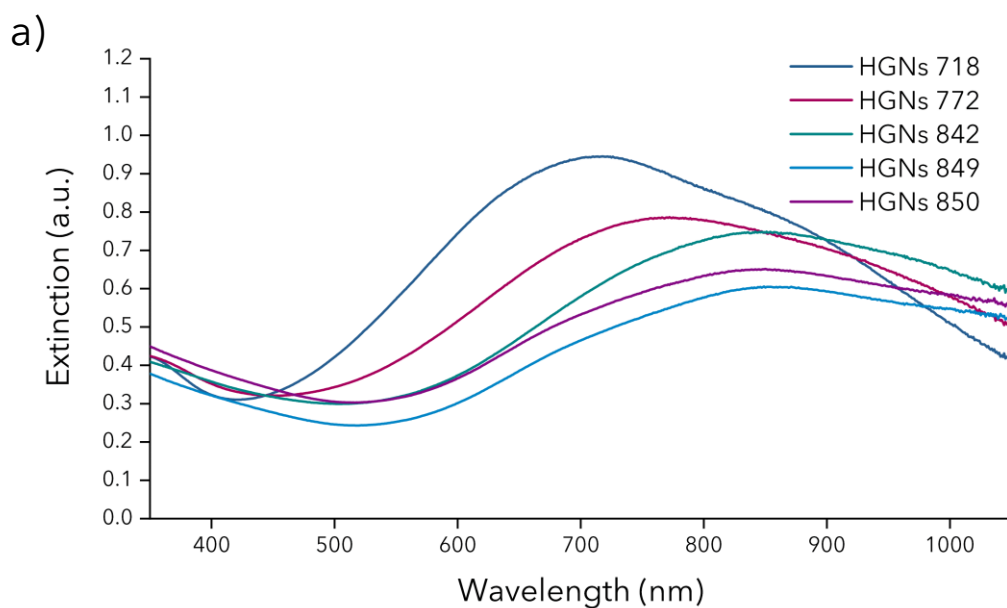
Figure 4.6: a) Extinction spectra showing batches of HGNs synthesised with varying LSPR from 718 – 850 nm, with the LSPR of each spectrum given in the key of the figure. The ratio of Ag:Au investigated for each batch are provided in section 6.3.2 of the Experimental chapter. The spectra were taken at a scan rate of 600 nm/min. b) Image of batches of HGNs with their respective LSPR's showing the colour gradient observed upon a bathochromic shift.

As predicted, and mentioned in the literature, the LSPR for the HGNs shifted to higher wavelengths with increasing Au^{3+}.[244,245] This was evident from the colour gradient which was observed with increasing wavelength. These nanoshells were blue in appearance and the intensity of the colour decreased as they tended towards longer wavelengths. As HGNs shift towards longer wavelengths, the intense blue colour begins to drop, and they develop grey tones.[226,231] The extinction spectra in Figure 4.6(a) were broad highlighting a size distribution within each batch of prepared HGNs.

This could be attributed to the synthesis, as it is impossible to get the same amount of gold onto each AgNP, therefore resulting in particles with varied diameters.

In this particular study, the sacrificial template (AgNPs) was kept constant between the batches, hence, with the Au^{3+} concentration increasing, it would allow for the extra Au to deposit on the outer surface, resulting in a thicker shell. This resulted in the average diameter of the HGN increasing as shown by the DLS data provided in Figure 4.7.
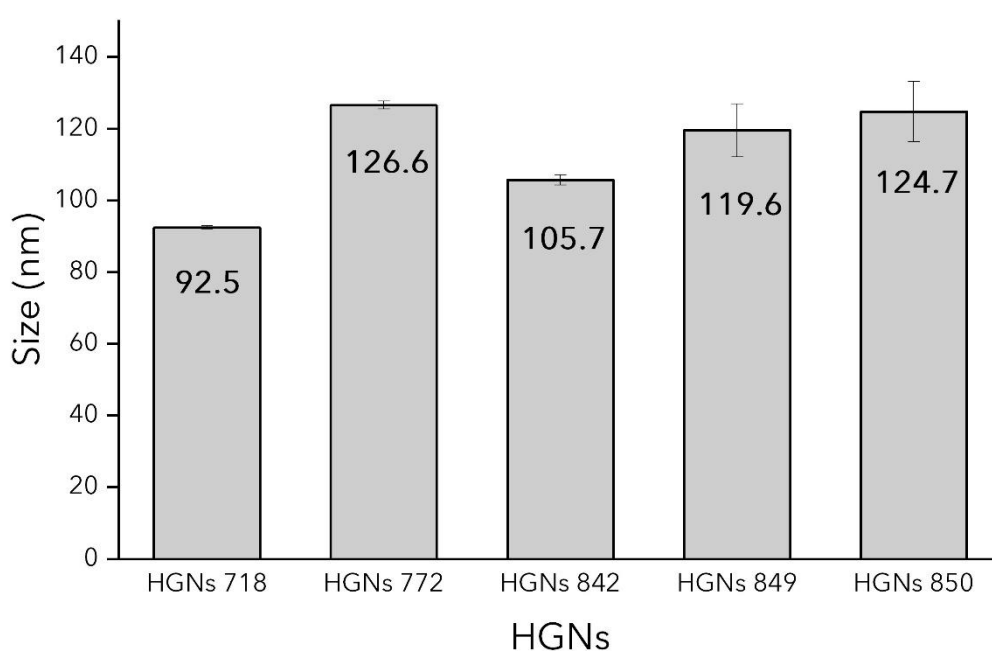
Figure 4.7: Bar chart with DLS data of various batches of HGNs with varying Ag:Au ratio. The error bars show the standard deviation of each batch. Measurements were carried out in triplicate. The title of each sample is their respective LSPR.

Although the average diameter increased with increasing Au^{3+} concentration, there was a slight deviation from the general trend with the second batch (HGNs 772). As the size data was considerably larger than anticipated, this was thought to be an experimental error. The study was not

repeated as the aim here was to outline the general correlation between LSPR and average diameter. The correlation between increasing diameter and increasing LSPR is also exhibited in several studies in literature, further strengthening the fact that this was an experimental error.[226,231,242] As a more definitive measurement, SEM or TEM (Transition emission microscopy) could be carried out to determine the exact dimensions of the particles.

Another point that can be mentioned is that the DLS data correlated very well with the extinction spectroscopy data. It has been previously reported that a shift in LSPR is indicative of a change in NP shape, size, and/or aggregation. The size data confirmed that as the Au: Ag was adjusted to increase the shell thickness, hence the size of the HGNs, the LSPR also increased. The LSPR also affects the plasmonic properties of the HGNs, which is indicated through a change in the colour of the colloidal solution.[166]

From this study, the chosen ratio of Ag: Au was 3:2.5, as the resulting LSPR of those HGNs (772 nm) was in close proximity to the excitation wavelength of the heating laser (785 nm). It was known that the exact wavelength would not be reproducible with a repeat synthesis, however, would be in close proximation. The synthesis was scaled up and this gave HGNs with an LSPR of 748 nm, and this batch was used for subsequent studies mentioned in the remainder of this chapter. The extinction profile of this particular batch is given in Appendix 6. SEM data was also acquired which determined the diameter of the nanoshells to be predominantly ~60 nm (Figure 4.8), although a range of sizes were observed. This can be correlated with the broad LSPR, which highlighted the polydispersity of HGNs. In literature HGNs, with an LSPR of ~740 nm were shown to have a diameter of 50 nm, hence it was understood that a dimeter of ~60 nm would be typical of HGNs with an LSPR of 748 nm.[226] The difference in size between the nanoshells and their template (AgNPs) is attributed to the different analysis techniques used. The latter were analysed by DLS which, typically, is an overestimation of the average diameter. From the literature, AgNPs with a similar LSPR is

known to be ~30-35 nm. The resolution of the microscope used was not high enough to detail the pinholes/cavities in the nanoshell, which occur on the surface of the nanoshell, yet the hollow centre was evident. TEM would be better at detailing the pinholes/cavities in the nanoshell. This would also be essential for determining the shell thickness, as SEM could not provide this. The zeta potential, as mentioned previously, provides information on the NP surface charge, which indicates the stability of the nanostructures. HGNs were found to have a zeta potential of -49.6 ± 5.1 mV, an expected net negative charge due to the citrate ions present on the surface of the HGNs. As the value was greater than the proposed value of 30 mV, the HGNs were considered stable.[155]

In summary, a successful synthesis could be confirmed. Comparing the starting (AgNPs) and final products (HGNs), an increase in LSPR and size was observed, as well as observing a hollow centre in the SEM for the final product. It would have been interesting to obtain an SEM of the AgNPs to highlight the change in solid AgNPs versus hollow HGNs, however, this was not acquired. An example is presented in the work of Sun *et al.*, who outlines the gradual galvanic replacement reaction through TEM images.[239]
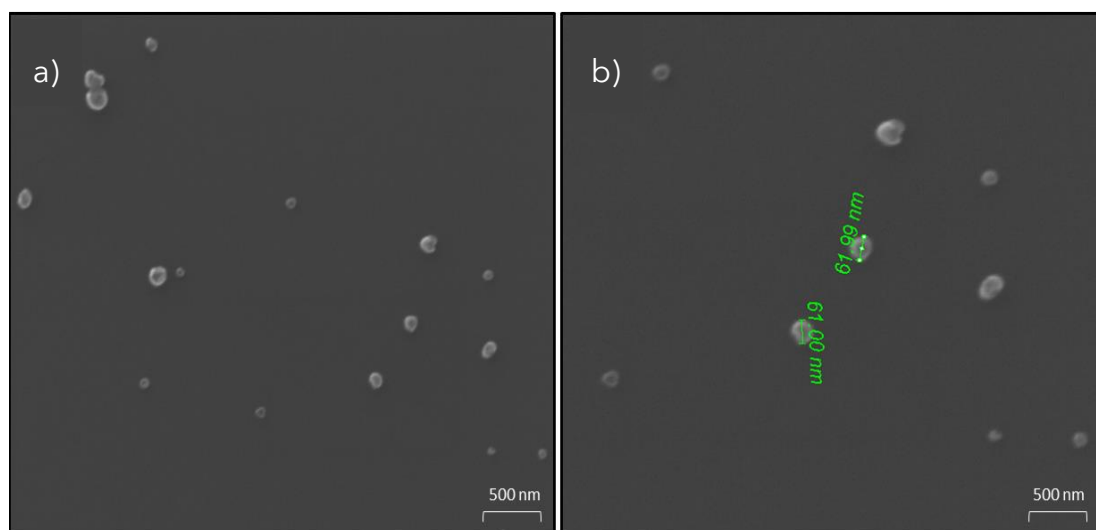
Figure 4.8: a) SEM of batch HGNs with a LSPR of 748 nm. Image was taken using a field-emission environmental SEM. b) Zoomed in image (a) to display the sizing.

4.3.1.3 Functionalisation of Hollow Gold Nanoparticles

There are many bio/molecules and linker molecules that can be used for surface modification of HGNs. Amongst them is PEG (polyethylene glycol), a linker molecule, which can prevent the nanoparticles from being cleared by the RES (reticuloendothelial system), hence the nanoparticles have longer circulation time in the body.[227] Biomolecules such as antibodies,[246] aptamers[247], and polypeptide chains,[248] have been used for tumour targeting. An example of this can be seen in the work of Melancon *et al.* who attached monoclonal antibodies to HGNs intending to target and ablate epidermal growth factor receptor (EGFR)-positive cancer cells *in vitro,* a receptor overexpressed in a variety of solid tumours such as cancers of the brain, pancreas, and lungs.[249] Likewise, there are numerous other cases where HGNs are functionalised with biomolecules for tumour targeting, however, the literature is deficient in using HGNs as agents for CVD systems. Therefore, partly the focus of this research was to contribute and strengthen the bridge between HGNs and CVD.

Essentially here, the aim was to 'transfer' the entire functionalisation process of the cholesterol modified nanoparticles to HGNs, by keeping the same method of adding a Raman active dye and then the chol-DNA. However, modifications were made knowing that HGNs had an overall larger surface area.

In the first instance, MGITC was functionalised on to the HGNs at a final concentration of 0.1 µM. MGITC was the dye previously used in the work with spherical AuNPs and it was decided, for consistency, that the same dye would be used for these studies. The reason for this chosen concentration was because it was again used for spherical AuNPs, hence it was initially trialled with HGNs to see if a signal could be identified. Upon an intense signal being seen, this was chosen as the concentration to move forward with. SERRS was carried out prior and post DNA functionalisation and it was

observed that the signal remained intense (Figure 4.9). The slight drop in the intensity after adding the DNA was attributed to the unbound dye being removed in the centrifugation step and potentially, the DNA removing some dye whilst attaching to the surface of the HGN.
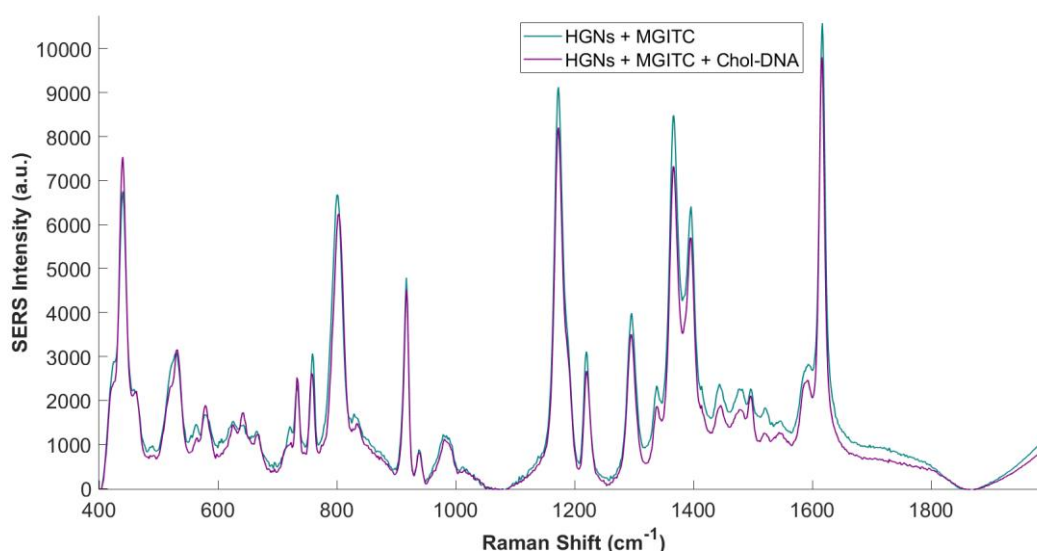
Figure 4.9: SERRS spectrum displaying functionalisation of HGNs + MGITC (Teal) and HGNs + MGITC + chol-DNA (Purple). Spectra was acquired using a Snowy Range Raman spectrometer with a 638 nm laser excitation wavelength. A 40 mW laser power was utilised with an integration time of 1 second. Data presented is an average of three replicates, and all data was processed and averaged in MATLAB®.

The DNA functionalisation step proved to be slightly more problematic. Firstly, it was difficult to estimate the ratio of DNA: HGN to add as this could not be worked out solely using the size data from the DLS. The concentration of the HGNs could also not be calculated due to instrument limitations. Hence, it was decided that the best route was DNA loading using the volume of DNA, and from this, the concentration of the added DNA could be calculated. The final aim was to get a full coverage of chol-DNA so this was thought to be a viable route. 50 µL of DNA was added which gave a final

concentration of 0.75 µM in solution. This was conclusive from the extinction spectra, Figure 4.10, which were used to characterise the conjugates.
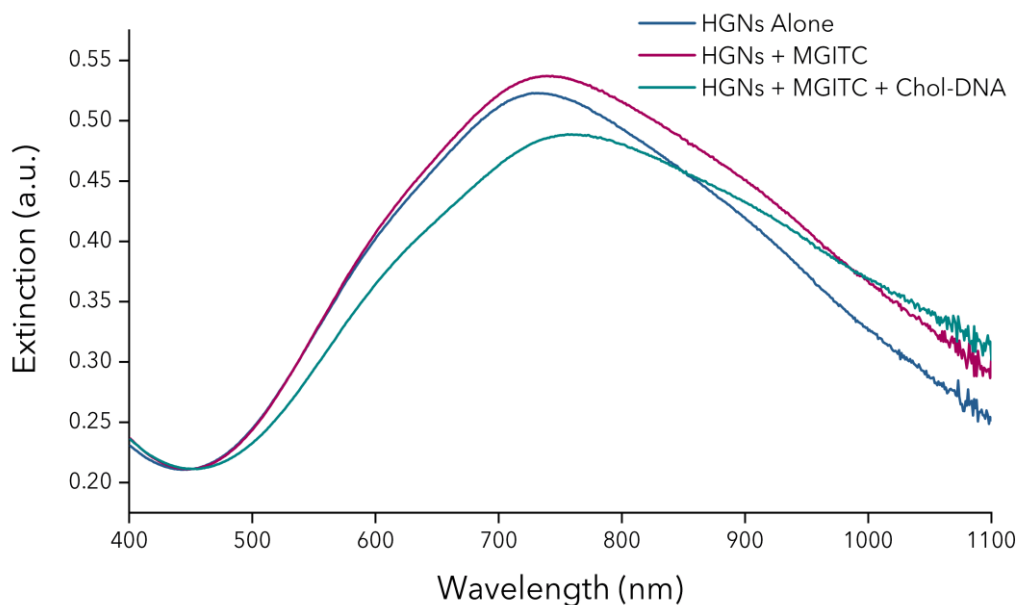
Figure 4.10: Extinction spectra from the HGN functionalisation experiment showing HGNs alone (blue), HGNs + MGITC (purple), HGNs + MGITC + Chol-DNA (Teal). Spectra were acquired at a baselined scan rate of 600 nm/min, with three replicates. Spectra were averaged and normalised (at 450 nm) using Microsoft® Excel and Origin®. The un-normalised spectra are given in Appendix 7.

From the above results, it was observed that the chol-DNA functionalised HGNs had undergone a bathochromic (red) shift from that of the bulk HGN solution (HGN 748 - before any modifications and centrifugation steps). However, the MGITC functionalised HGNs and bare HGNs, in an opposing manner, had a hypsochromic (blue) shift. The results correlated with a successful functionalisation because when a shift in the LSPR and/or broadening of the peak is observed, it is indicative of a change in the size, shape, or surface environment of the nanostructure.[61] As there was peak

broadening and shifting observed, the functionalisation was successful.[166] Other reasons also contributed to this conclusion. Firstly, with the attachment of the bulky chol-DNA, this increased the overall diameter of the HGN, therefore shifting the LSPR to a longer wavelength of 757 nm. A similar trend was also observed when chol-DNA had successfully attached to spherical AuNPs. Secondly, the controls (Bare HGNs and MGITC-HGNs) did not have a full monolayer coverage due to the absence of DNA, which meant they did not have a protective layer, and thus when they underwent the centrifugation step, they started to degrade. With the slight deterioration of the shell, the diameter decreased resulting in a hypsochromic shift. It should be noted that the MGITC functionalised HGNs had the same concentration of dye added as to that of the DNA functionalised HGNs, as the aim was to highlight the free surface available for DNA attachment. The MGITC coated HGNs shifted to 741 nm and the bare HGNs to 728 nm. A similar case was mentioned by Kearns *et al.* in their work, in which they discussed the heating of PNIPAM (poly(*N* - isopropyl acrylamide)) coated HGNs.[250] The control of citrate capped HGNs, post-heating, were analysed by extinction spectroscopy to highlight aggregation, evidently seen from the considerable peak broadening and dampening. They reasoned that the bare HGNs, due to the absence of a protective coating, were not stable during photothermal experimentation. Here, however, the control peaks did not undergo such excessive changes as the functionalisation process did not change the morphology of the HGNs as much as heating had for the bare HGNs in Kearns work. A quick comparison between the original extinction spectra of the colloidal HGNs and the control bare HGNs was made, which displayed considerable peak dampening and broadening of the latter (spectra provided in Appendix 8). This again highlighted that the control bare HGNs from the experiment were tending towards aggregation. A study by Chandra *et al.* also highlighted that the blue shift in HGNs LSPR was as a result of aggregation, with the extent of the shift dependent upon the shell thickness.[251] A kinetic study or timed-extinction studies could be carried out

to track the aggregation process however due to time constraints these could not be conducted.

The average LSPR's from the extinction spectroscopy data were plotted in a scatter graph against the original LSPR of the batch HGNs, as shown below in Figure 4.11. Here, 'HGNs' referred to the control sample from the functionalisation experiment and 'HGNs (original LSPR)' refers to the LSPR of the batch HGNs. Displaying the LSPR in this manner allowed for a clearer visual understanding of the shifting observed.
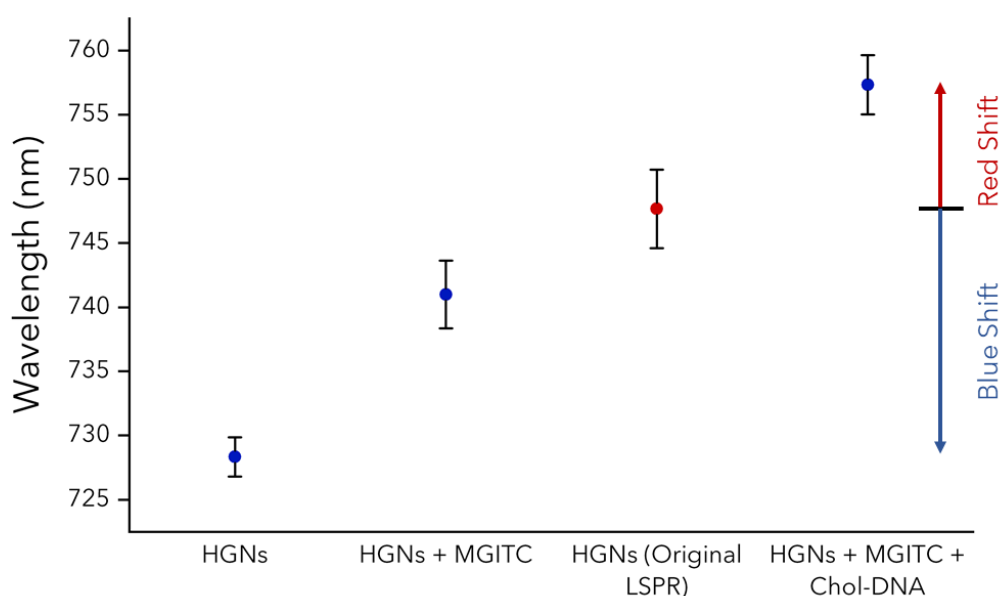
Figure 4.11: Scatter graph of LSPR's highlighting the bathochromic and hypsochromic shifts from the original HGN LSPR, upon modification of HGNs. The LSPR's were taken from the extinction spectroscopy data and each sample was analysed in triplicate. The data was averaged and plotted using Microsoft® Excel and Origin®.

The cholesterol functionalised HGNs were also analysed by DLS to determine their average diameter, which was found to be 132 ± 4.1 nm. The diameter of the original bare HGNs was previously found to be 109 ± 6.8

nm. With a considerable increase in the average diameter, this was further confirmation that the surface had been modified and was consistent with the extinction spectroscopy data. As mentioned previously, the chol-DNA is a bulky moiety, hence it was expected that the diameter would increase. These DLS results were also consistent with a study carried out by Mackanic *et al.* in which they functionalised ssDNA onto HGNs and witnessed an increase in the hydrodynamic diameter of the particles due to oligonucleotide attachment.[252] The two controls of 'MGITC-HGNs' and 'HGNs Alone' from the functionalisation study were not DLS analysed as they had degraded. A bar graph exhibiting the size difference with the associated error is given in Figure 4.12 below.
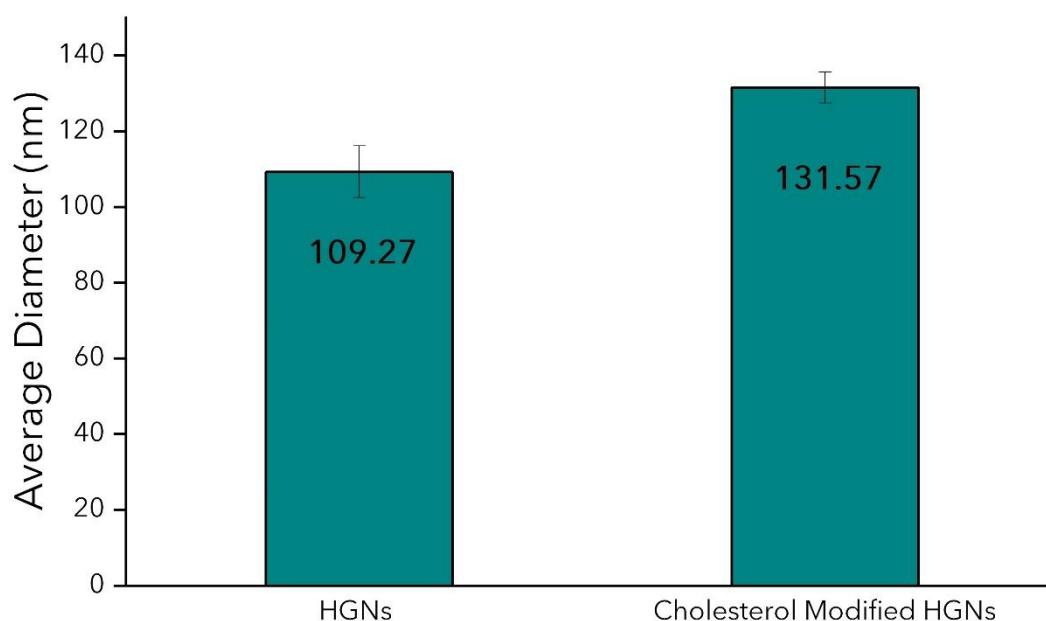
Figure 4.12: Bar graph illustrating the increase in average diameter of HGNs once the cholesterol is functionalised onto the surface. Data was obtained using DLS with three measurements taken of each sample. The error bars represent the standard deviation associated with the sample data. Data was averaged using Origin®.

4.3.1.4 Investigating the Stability of Functionalised Hollow Gold Nanoparticles

The long-term stability is important for functionalised HGNs, especially if progressing towards *in vitro* studies. Modified HGNs have been known to maintain colloidal stability when conjugated with varying biomolecules such as antibodies[247] and aptamers[253] for various selective targeting studies, highlighting the fact that they do remain stable for the duration of their cellular uptake work. In the work of Grabowska-Jadach *et al*., in which HGNs were functionalised with a selective aptamer towards targeting tumour cells, it was mentioned that they left their conjugates in the fridge for up to two weeks and only upon noticing precipitation were they deemed unusable.[253] This gave an insight into the shelf life of HGN conjugates.

Here, the conjugates did not show any visible aggregation for many days after functionalisation and being left in cool surroundings (Appendix 9), however, it was thought that a comparison of their extinction spectra post synthesis and then after a duration of time would determine if there were any changes. For this reason, extinction spectra were taken after one week of functionalisation and compared to the initial spectra, as shown in Figure 4.13.
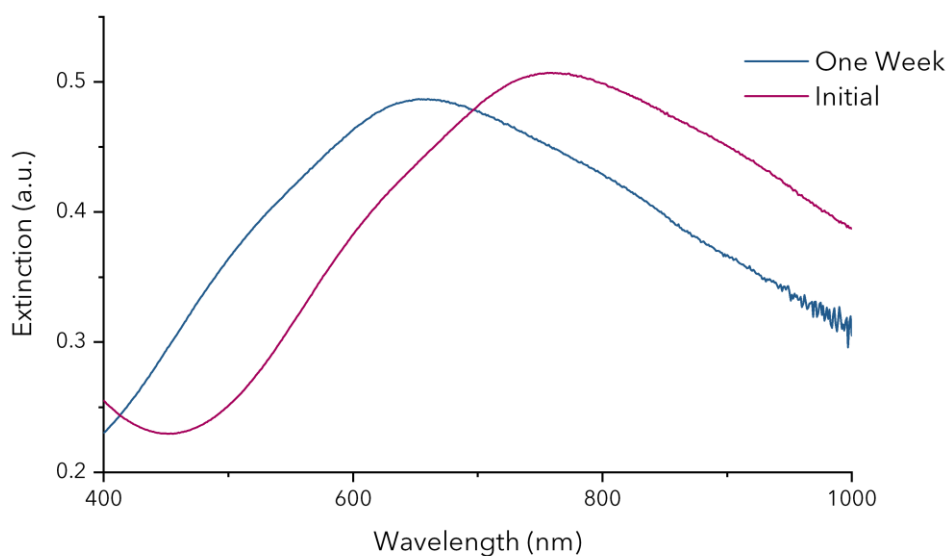
Figure 4.13: Stability study of chol-DNA HGNs in which the conjugates were analysed after one week and data compared to the initial extinction spectra. Spectra were taken at a scan rate of 600 nm/min and are an average of three replicates.

The blue shifting of the LSPR after one week concluded that the particles were changing over this period. The hypsochromic shift was evidence that potentially the gold shell was beginning to collapse in on itself and this reduction in the diameter was resulting in such a change. The reason for this change could be that the entire surface was not covered with DNA, exposing it to slow degradation. The HGNs have pinholes that enable the inside of the hollow shell to allow attachment of biomolecules also. It may be that some of this surface is left exposed so although the outer surface is covered, the inside surface may have some exposed area. Time permitting, it would have been interesting to track their stability daily which would highlight whether the changes were instant or after some time. It should be noted that all studies were carried out with fresh batches of conjugates, hence no interference in results from stability issues are anticipated and these studies were only carried out to determine their shelf life.

4.3.2 Photothermal Studies Using an In-House Setup

The photothermal properties of metallic nanostructures are advantageous in a clinical setting. These 'agents' can be directed to areas of interest and when the heat is applied to them, their internalised heat can dissipate to the surroundings resulting in damage to the nearby cells. This therapy method has been widely used in cancer therapy as cancerous cells have a lower thermal tolerance in comparison to healthy cells.[78]

Recently, this approach was extended to CVD, and the first-in-man trial utilising plasmonic photothermal therapy (PPTT) for the regression of atherosclerosis was carried out. The Plasmonic Nanophotothermal Therapy of Atherosclerosis (NANOM-FIM) trial looked at two approaches to NP delivery.[26] One set of patients received a bio-engineered on-artery patch of silica-gold NPs, which was implanted using a minimally invasive cardiac surgery, and the other group had silica-gold iron NPs delivered to the artery via a micro-catheter. The control group received stent implantations. The therapy, carried out with either an intravascular or transcutaneous NIR laser, resulted in a reduction of the atherosclerotic plaque with both of the nanoparticle treatments. The greatest results, however, were obtained from the treatment via the on-artery patch of silica-gold NPs. This trial highlighted that PPTT does contribute to the minimisation of atherosclerotic plaque development and has the potential to be utilised as a therapy method for CVD.

HGNs in particular, have shown pronounced heating capabilities due to being efficient at converting light energy into heat.[254] In an effort to understand whether modifying HGNs with chol-DNA could result in enhanced thermal destruction *in vitro*, an in-house heating setup was used. In general, this setup comprised of a CW 785 nm laser excitation source directed at a small glass vial (1.75 mL) which contained the sample. A K-type thermocouple probe inserted into the glass vial was used to record the temperature reading, which was visual on a connected Picologger. The

probe was kept out with the path of the laser, as otherwise, this would increase the temperature reading. An image and schematic of the in-house setup can be seen in Figure 4.14 below.
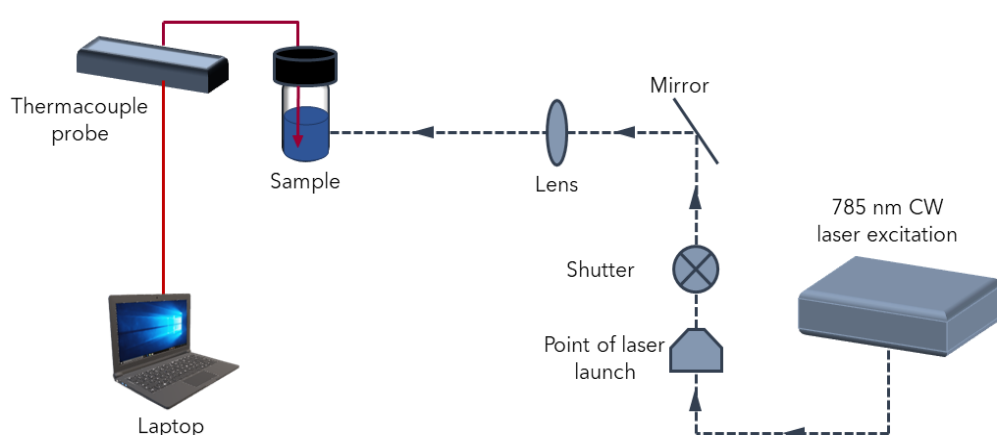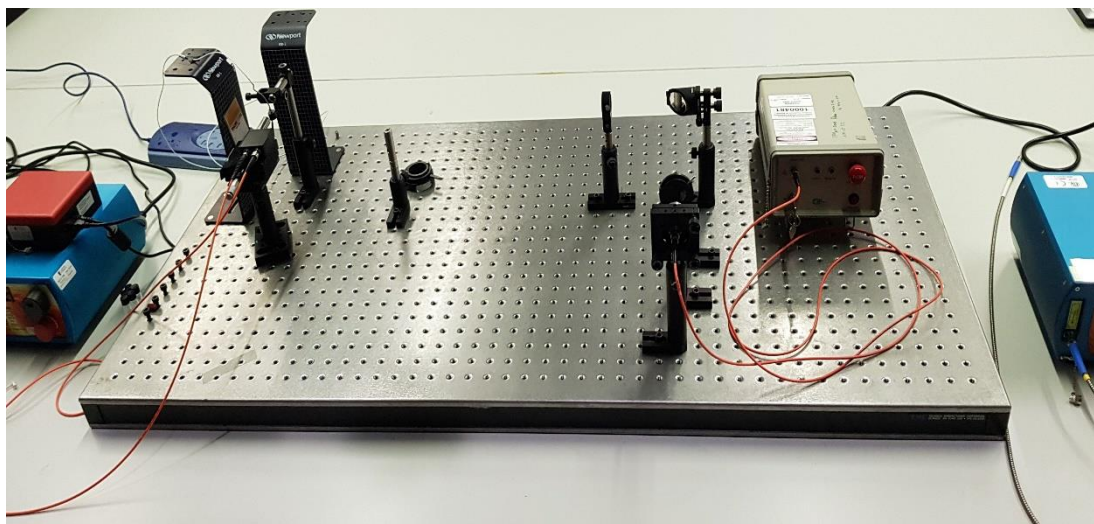
Figure 4.14: (top) Image of the in-house setup. (bottom) Schematic of the in-house setup detailing the parts within the setup. Arrows direct the laser direction from a 785 nm CW laser excitation source. The image is not drawn to scale.

4.3.2.1 Heating of Bare Hollow Gold Nanoparticles

Initial studies carried out investigated the heating profiles of bare HGNs (Figure 4.15). Upon irradiating the sample of bulk HGNs using the CW 785 nm laser excitation source, the temperature saw a sharp incline that started

to plateau after ~10 minutes of heating, once the maximum bulk temperature had been reached. Thereafter, the temperature remained constant until the end of the heating cycle, which was 30 minutes. Temperature recordings were taken using a K-type thermocouple probe, which was inserted into the HGN solution through an opening made in the cap of the glass vial, with real-time data being collected on the Picolog 6 data logging software. A maximum laser power of 330 mW was used to heat the sample, which saw the HGNs increase in temperature by just over 20 ºC. This was a result of the multi-step light to heat conversion process as described in section 1.3.2 of this thesis. In summary, the surface electrons on the HGNs become excited, after which a series of electron-electron, electron-phonon, and phonon-phonon processes occur, and the thermal energy is transferred to the bulk solution, increasing its temperature. The HGNs had an LSPR of 748 nm, which was in resonance with the laser excitation (785 nm), also contributing to the heating efficiency.
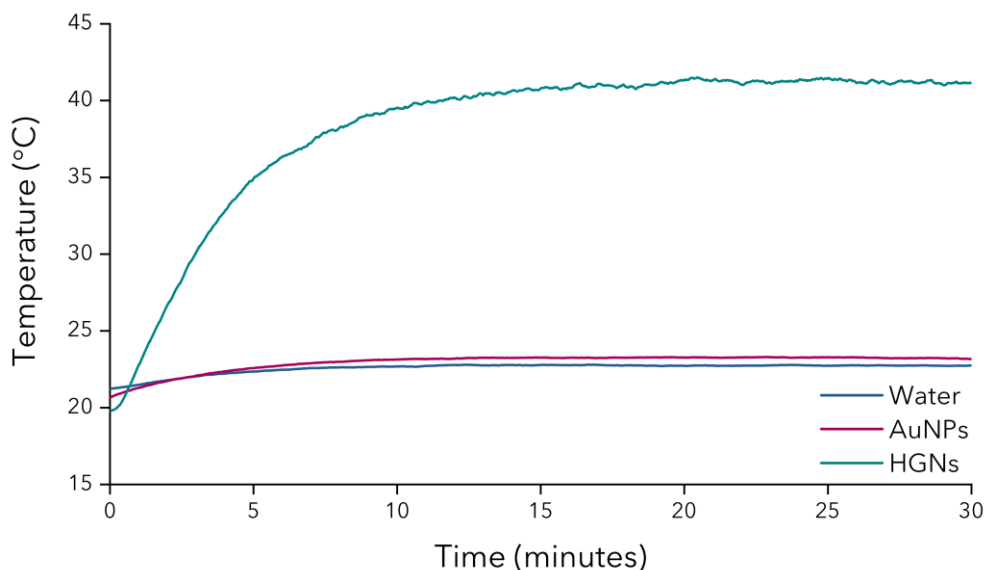
Figure 4.15: Heating profiles of HGNs and AuNPs. Profile shows a 20 °C increase in bulk temperature of HGNs in comparison to only a couple of degrees increase in the bulk temperature of AuNPs. Heating studies were carried out using a laser with a 785 nm CW laser excitation source at full power (330 mW). Studies were carried out over a 30 minute time period.

From the heating profiles, there was clear discrimination between the profiles of HGNs and AuNPs. Whilst there was a sharp increase in the temperature of the bulk HGNs, the latter had a profile very similar to that of water, which was the control, and both displayed very little bulk thermal change. This was due to several factors: firstly, the LSPR of HGNs closely matched that of the laser excitation wavelength, and secondly, HGNs are known as highly efficient light to heat converters.[254] The reason being that the conversion of electromagnetic energy into thermal energy is higher in porous nanostructures in comparison to their solid counterparts.[255] The results outlined above were consistent with a similar study carried out by Xie *et al*. in which they looked at the heating profiles of 775 nm HGNs and spherical AuNPs.[59]

Upon cycled heating of the same sample of HGNs, it was noticed that the maximum temperature of the bulk solution decreased with each cycle of

heating. This was thought to be degradation of the HGNs, through repeated heating resulting in them not being able to heat as efficiently as the first cycle. This was also consistent with previous findings.[250] It is for this reason that subsequent studies did not have replicates from the same HGNs sample. The cycled heating profile of a batch of HGNs is given in Figure 4.16, where heating was carried out for 30 minutes followed by a 15 minutes cooling period to allow the bulk temperature to return to its initial starting temperature. The cooling periods are highlighted between the dashed blue lines.
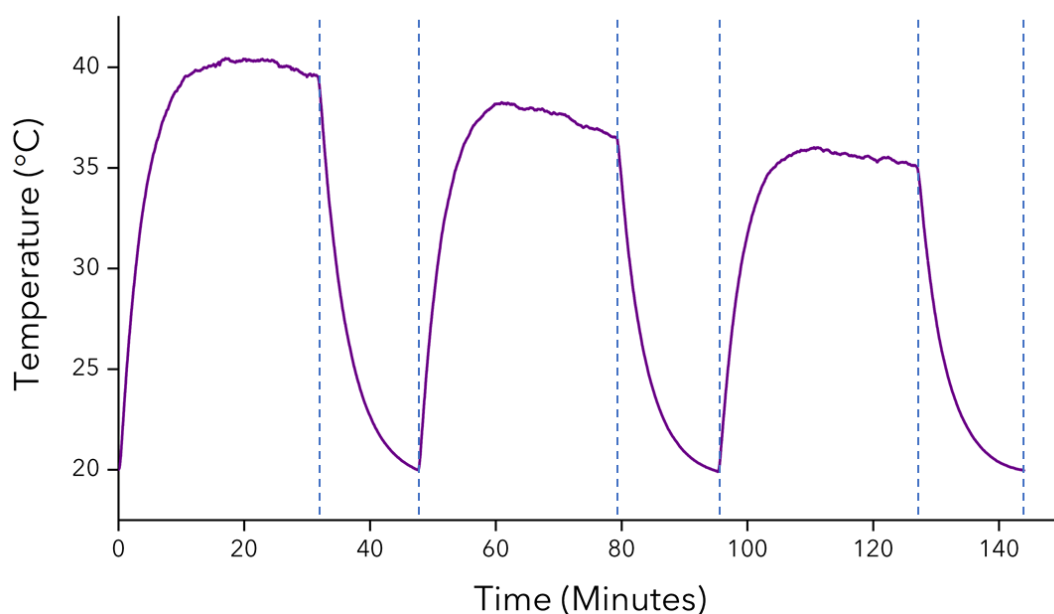
Figure 4.16: Cycled heating and cooling of HGNs. Heating was carried out over a 30 minute period followed by a 15 minute cooling period, which is highlighted between the dashed blue line. A CW 785 nm laser source was used at maximum power (330 mW).

A maximum laser power of 330 mW was initially used for all heating studies. Due to time constraints, studies varying the laser powers could not be carried out however, it is generally known that with increasing laser intensity, increased heating is observed, especially at the surface of the nanoshell.

Hatef *et al.* studied the surface temperature of HGNs with a 40 nm diameter and 3 nm shell thickness against laser intensity.[256] Using a CW laser excitation, results exhibited that surface temperature increased linearly as the laser intensified. Furthermore, investigating the temperature in and around the nanoshell itself, confirmed that the heat affected zone was in close proximity to the surface and a temperature drop was observed as the distance from the nanoshell surface increased. At a 200 nm distance, the temperature was ~10% of its maximum value. This study also highlighted that the temperature at the surface of the HGNs would be exceedingly high compared to that of the bulk solution.

Hatef *et al.* also compared the three types of laser light irradiations: CW (continuous-wave), short (nanosecond), and ultrashort (femtosecond) pulse laser. Their ideology was that a CW laser is best suited for applications that require an enduring, moderate increase in temperature heating such as the photothermal release of molecules and hyperthermia. This is the reason why this study primarily focused on the use of CW laser instead of a pulsed laser.

4.3.2.2 Photothermal Studies of Bare Hollow Gold Nanoparticles *In Vitro*

With the efficient heating profile of bare HGNs, the next step involved investigating their role as photothermal agents in cells. Their ability to promote thermal destruction in the cellular environment would then allow for studies with cholesterol modified HGNs in determining whether the latter have enhanced performance in thermal destruction, due to their increased cellular uptake.

Due to instrument limitations, the HGN concentration was calculated after photothermal studies, and hence all photothermal studies were carried out by volumes. The concentration of HGNs was worked out after the study to be 26.7 pM and was three-fold lower than that of AuNPs, which were 96.5

ρM. Although the HGNs were of a lower concentration, they were more efficient at heating than their spherical counterparts, as will be observed. A procedure was devised whereby 30 μL of HGNs were added to cells which had a concentration of 1.5×10^6 cells/mL. HUVECs were the chosen cell line as these were the primary focus of this research work. The nanoshells were incubated with the cells for 3 hours. Thereafter, the cells were counted, and samples were made up in small glass vials. These were kept in the incubator during the heating studies to minimise cell death by exposing the cells to undesirable surroundings. Each sample was heated for 30 minutes to allow comparability between results. Again, the resonant CW 785 nm laser excitation source with a maximum power of 330 mW, was used to ensure maximum heating of the samples. The temperature of the bulk solution could not be measured as it was not possible to insert the K-type thermocouple probe into the sample. This would contaminate the probe with cells, meaning one probe would have to be used per sample and as this was not feasible, temperature recordings were avoided.

Succeeding heat exposure, the remaining cells were counted using the traditional Trypan blue staining method, as stated previously in section 3.2.5. Each sample was counted three times in a quick, yet efficient manner and the results were combined into a bar graph as shown in Figure 4.17. As controls, HUVECs alone, followed by bare AuNPs in HUVECs were heated.
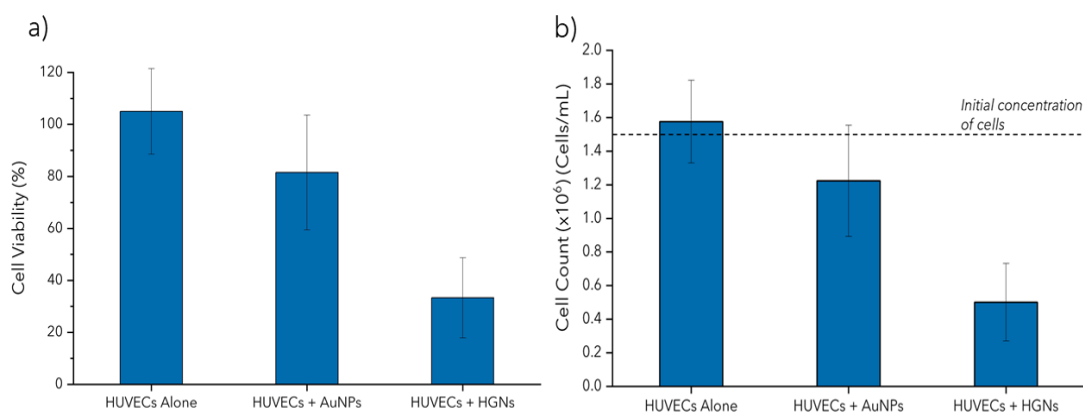
Figure 4.17: Bar charts depicting: a)cell viability, b) cell counts post heating of bare HGNs in HUVECs. The data confirmed HGNs to have a pronounced thermal effect in the cellular environment. Each sample was heated for a period of 30 minutes, using a 785 nm laser excitation source at full power (330 mW). Cell counts were carried out in triplicates for each sample and three replicates of the study were carried out to calculate an average cell count as shown in the chart. The standard deviation is given in the form of error bars.

From the initial heating studies carried out *in vitro*, it was distinctly evident that HGNs, through their remarkable heating capabilities had increased cellular death. The cell viability was considerably lower in comparison to the controls. It should be noted that the contribution from the surrounding media was negligible and this could be stated by the results from the controls as they displayed minimum change to cell count, therefore confirming that the media itself was not a contributor. The other point to mention is that the laser light was directed towards the solution and every effort was made to avoid it being directed at the glass vial sides, as this would increase the temperature of the bulk solution considerably. Hence, the results suggest that the HGNs were primarily the reason for cellular destruction. The respective cell count for each sample is provided in Figure 4.17(b).

4.3.2.3 Photothermal Studies of Cholesterol Modified Nanoshells *In Vitro*

The next step involved the heating of chol-DNA HGNs in HUVECs (Figure 4.18). It was expected that with the modification of cholesterol onto the HGNs, there would be increased cellular uptake of these nanoshells, resulting in increased cellular ablation. Bare and functionalised HGNs were incubated with cells for three hours before detaching and counting. Samples with an initial cell concentration of 1 x 10^6 cell/mL were prepared in small glass vials and left in the incubator during heating studies.
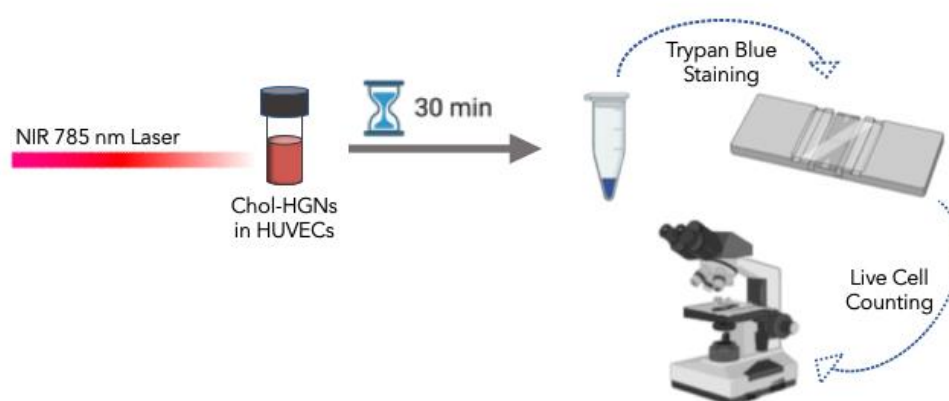
Figure 4.18: Schematic illustrating the heating of chol-DNA HGNs in HUVECs using a NIR 785 nm laser, subsequently being stained with Trypan Blue, and a live cell count being carried out using a microscope. Schematic is not drawn to scale.

Analysing the results from the study (Figure 4.19), the cholesterol modified HGNs seemed to show greater penetration into the cells. This was attributed to the fact that the cell viability was lower (61%) than for the bare HGNs (76%), hence there would have been more HGNs internalising resulting in increased heating. Another point to mention is that although each study was carried out with 30 μL of bare/functionalised HGNs, the concentration of the two may have slightly differed. This is because as the functionalised HGNs

underwent a centrifugation step during the functionalisation process, they would potentially have lost some nanoparticles, thus resulting in a slightly lower bulk concentration. In saying that, showing greater heating capabilities again highlighted that the cholesterol did have pronounced effects on cellular ingestion.

It was also thought to investigate whether having the cells outwith their optimum conditions (37 °C and 5% CO_2) contributed to cell death. Hence, samples (chol-DNA HGNs in HUVECs) were also left out at room temperature next to the heating setup. These samples gave an average cell viability of 62%, showing very similar effects to their heated counterparts. Although this could suggest that the heating may not necessarily have been the cause of cell death, and in fact, it was the removal of the cells from their optimum conditions. In defence, it could be argued that when the samples are subjected to laser irradiation, they are exposed to high temperatures and the temperature at the surface of the nanoparticle will be much higher. Therefore, it may be the case that for each sample the reason permitting cell death is varied. This was an initial study with only two repeats, hence the potential of experimental error and the variability in cell counts has to be taken into consideration. This is because, with each sample preparation for counting, the pipetting error can contribute drastically to the variance in cell numbers. The respective cell count for each sample is provided in Figure 4.19(b).
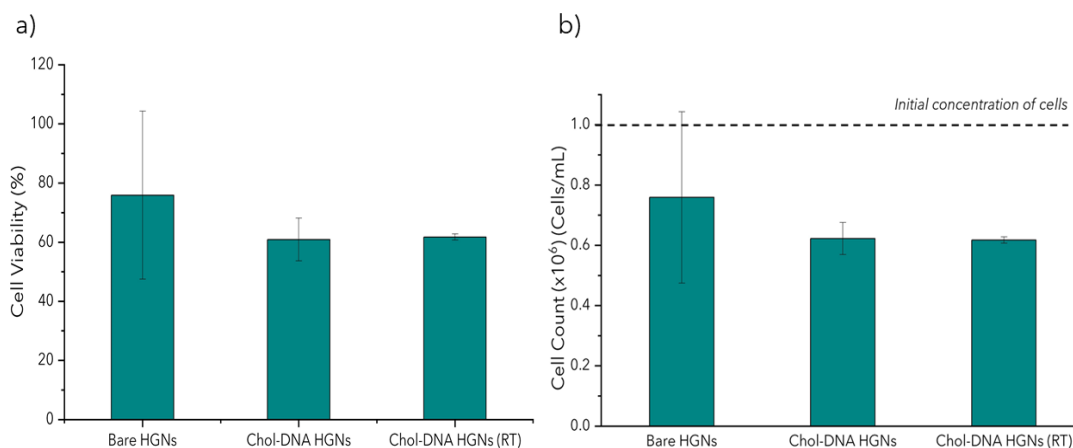
Figure 4.19: Bar charts illustrating: a) cell viability, b) cell counts post heating of bare HGNs and chol-DNA HGNs in HUVECs. The data confirmed chol-DNA HGNs to have a pronounced thermal effect in the cellular environment. Each sample was heated for a period of 30 minutes, using a 785 nm laser excitation source at full power (330 mW). Cell counts were carried out in triplicates for each sample and two replicates of the study were carried out to calculate an average cell count as shown in the chart. The standard deviation is given in the form of error bars.

To understand if the currently used laser output is viable in an *in vivo* setting, the laser intensity was compared to that used in previous clinical trials and also literature. In the NANOM-FIM trial, which was mentioned in section 4.3.2, a mW NIR laser was utilised for a 7-minute exposure time (35-44 W/cm^2).[26] In comparison to that, the laser used in this study used a mW laser irradiation for a 30-minute exposure time, with a power density of 0.825 W/cm^2. In other studies, a 50 mW/cm^2 laser power was used for 1 minute of heating,[237] and another used a 32 W/cm^2 laser power for 3 minutes.[233] The variations in intensities and timings concluded that a 'standard' for laser powers and heating times does not exist. The NANOM-FIM trial mentioned that the characteristics of the laser were personalised in their case, taking into consideration the body-mass index, thickness of skin, amongst other factors, which can be expected as tissue depth and severity of tumour will be case dependent.[26] These comparisons were used as a general guideline to help decipher whether such parameters used in this study were

comparable to those used *in vivo* or if major adjustments needed to be made to obtain results accordingly. Future work would involve trying to vary the laser intensity and observing the cell viability in such a case.

4.3.3 2D SERRS Mapping of Cholesterol Modified Nanoshells *In Vitro*

2D mapping was carried on HGNs in HUVECs to confirm that these nanostructures were successful in cellular uptake, although this was anticipated to be the case. HUVECs were plated 24 hours prior to HGNs addition, after which they were incubated for 3 hours. The cells were then washed and fixed down before mapping. All mapping was carried out using a 633 nm laser excitation source at 10% laser power, with a 1 second acquisition time and a 2 µm step size. Data were processed using WiRE 4.2 software and DCLS plots were used to analyse the data, which are given in Figure 4.20.
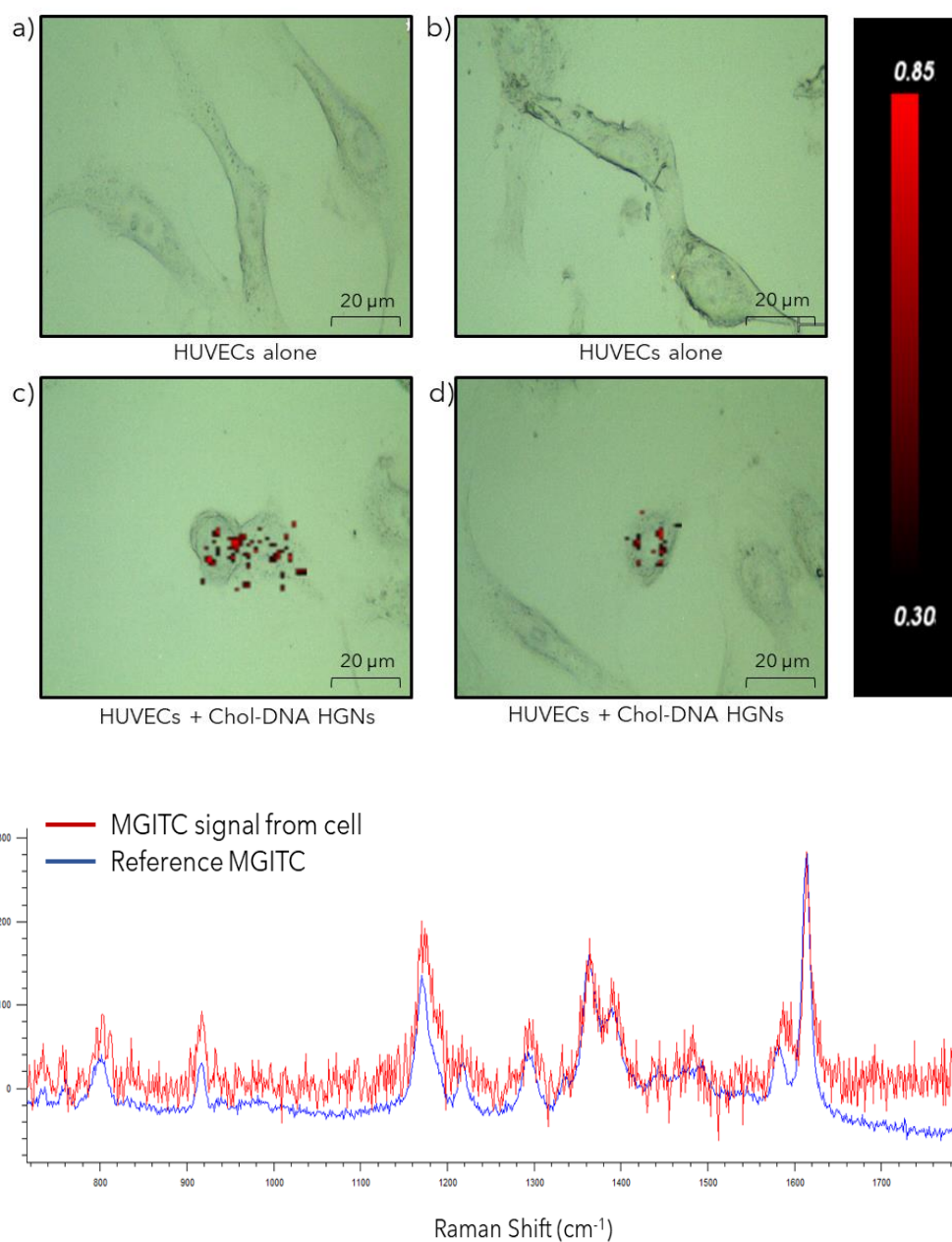
Figure 4.20: DCLS of 2D SERRS mapping of functionalised HGNs in HUVECs. a/b) HUVECs alone, c/d) Chol-DNA HGNs in HUVECs. Cells mapped using a Renishaw inVia Raman confocal microscope and data processed using WiRE software. Maps acquired using a 633 nm laser excitation with 1 second acquisition times, at 10% laser power. False colour images were generated using DLCS analysis and show the successful uptake of functionalised HGNs in cells. e) A typical MGITC signal observed from the cellular environment (red) compared to the reference MGITC spectrum, used for DCLS analysis (blue).

The maps indicated that there was considerable uptake of the functionalised HGNs. Although the majority of the signal came from within the cell, there was also a signal from the extracellular space. This was thought to be the nanoparticles that were close to being ingested, as they are close to the cell membrane. It may also be the case that HGNs need a little longer in incubation with the HUVECs. As previous cell studies were conducted with three hour incubation times, the conditions were kept consistent here, hence future studies would look to optimising the incubation times. The % SERRS response per cell area was calculated using ImageJ, as described in section 6.2.2.2. From 10 biological samples, the average % area of SERRS response was found to be 2.6 %. It should be highlighted that the cellular uptake was not as high as for spherical nanoparticles functionalised with cholesterol DNA (16.2 %) because here, 30 μL of functionalised nanoparticles were added in keeping consistent with other studies carried out in this chapter. Spherical cholesterol modified particles were added at a concentration of 6 ρM previously. This experiment was carried out merely to confirm that there was successful ingestion of nanoshells. Further experimentation would need to be carried out to optimise the concentration of HGNs for *in vitro* studies, and in line with previous *in vitro* studies, comparing controls of pegylated or polyT-DNA HGNs, which would, in turn, allow a better understanding of their uptake. 3D SERRS mapping is also proposed, which would confirm the MGITC signal from within the intracellular space.

4.3.4 Cytotoxicity Evaluation of Cholesterol Modified Nanoshells *In Vitro*

It was important to understand the toxicity of HGNs and whether the prime contribution towards cell death was either the HGNs themselves or the heating. Bare AuNPs are non-toxic, however bare AgNPs are cytotoxic. The synthesis of HGNs involved AgNPs as a sacrificial core and hence there was

the possibility of the remainder of traces. A study was prepared whereby cells were incubated with both, HGNs and chol-DNA HGNs, and subsequently stained with Trypan blue for counting to determine cell viability. The results presented in Figure 4.21 determine that HGNs do not have a significant effect on cell viability and in fact, have good biocompatibility with the cells. The cell viabilities for both samples were 86%, and the slight reduction in the cell count was attributed to unreacted AgNPs, which may have a cytotoxic nature. If HGNs themselves were cytotoxic then the cell viability would have been much lower. These results were concordant with the work of Grabowska-Jadach *et al,* who confirmed HGNs to be non-toxic when they incubated aptamer-functionalised HGNs with tumorous (A375) and normal cells (HaCaT). Using an MTT assay they deduced that their functionalised HGNs did not have a detrimental effect *in vitro*.[253] The cell count for each sample is provided in Figure 4.21(b).
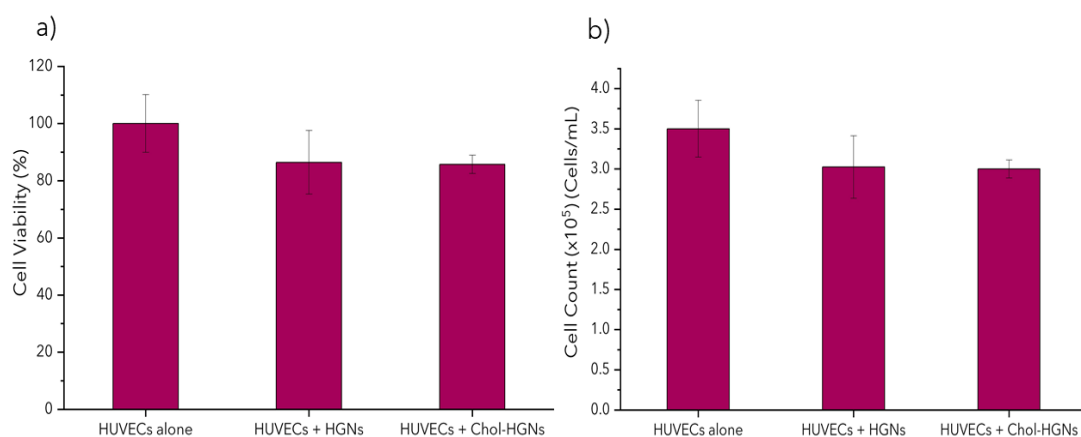
Figure 4.21: a) Cell viability and b) cell counts from the studies of bare and functionalised HGNs in HUVECs, which show the non-toxic nature of HGNs to cells. Viability studies were carried out using the Trypan blue staining and counting method. Experiment was carried out in duplicate with three replicates of each sample taken. The standard deviation is given as error bars.

Another vital question poses as the excretion of HGNs *in vivo*. Their non-cytotoxic nature is witnessed, however, if they are not easily excreted from

the human body, this could potentially be harmful. Recently, Zhang *et al.* published a study in which they synthesised biodegradable HGNs for IPT-BT (photothermal-brachy-therapy). Their remarkable study outlined the decomposition of HGNs into less than 5 nm within 24 hours, subsequently allowing renal clearance. They were able to reach this understanding by trialing the HGNs in various simulated physiological environments using a biological simulation system.[257] This study provides an insight into the clearance ability of HGNs from the human body. In addition to this, many other research groups have investigated the clearance abilities of differing nanostructures from the body and conclude that these can efficiently clear from the system if they are optimised for renal clearance.[258,259]

Although a general statement can be made concerning the toxicity of HGNs or any other nanostructures, it is important to remember the sensitivity of such research as it involves risk to health. As quoted by Gad et al., "..it is important to treat each nanoparticle application individually to determine the potential benefits and hazards to public health".[260]

4.3.5 Concluding Remarks

HGNs are demonstrated as biologically applicable nanostructures due to their ability to navigate their LSPR in the NIR region, attracting many biological and medical applications. The HGNs were synthesised to have an LSPR as close as possible to the heating laser, which in this case was 785 nm. Successful synthesis yielded HGNs with an LSPR of 748 nm and size data obtained from the SEM indicated the nanostructures to have an average diameter of 60 nm. Thereafter, HGNs were successfully functionalised with chol-DNA and MGITC, a monolayer coverage sufficiently stabilising the nanoshells. Extinction spectroscopy and DLS data confirmed successful functionalisation, shown by an increase in diameter size and an

bathochromic shift in the LSPR, in comparison to a hypsochromic shift seen by the bare HGNs, due to aggregation.

Photothermal studies of bare and functionalised HGNs were carried out using a NIR 785 nm laser excitation source. In the first study of comparing HGNs to spherical AuNPs, the former displayed remarkable heating, in line with a similar study in literature.[59] And again during *in vitro* studies, the HGNs successfully ablated surrounding cells as seen by the considerably reduced cell viability. As the PTT studies moved forward to compare bare and functionalised HGNs, the latter did have a pronounced effect in cell death, even though they had a lower concentration than the control. However, the cell viability of chol-DNA HGNs left at room temperature was very similar to its heated counterpart. This study was preliminary and would require further work to investigate whether the reason for cell death was the heating or the cells being outside their optimum surroundings. All photothermal studies were carried out using volumes instead of concentrations as at the time SEM data was not acquired. The concentration of HGNs was worked out after the study to be 26.7 pM and was three-fold lower than that of AuNPs which were 96.5 pM. Although the HGNs were of a lower concentration, they were more efficient at heating than their spherical counterparts.

Due to laboratory closures and time constraints, planned optimisation studies of the heating experiments could not be carried out. These studies were to include optimising the laser power, heating times, and concentrations of HGNs. It would be interesting to investigate the minimum concentration of HGNs required to provide an effective response in cell ablation. Optimising concentration of HGNs with a reduced laser power would help reduce the potential risk of any thermal damage *in vivo*. In addition to this, it would be important to understand the 'minimum dose' of HGNs which would provide an effective response. Further to this, the laser intensity also requires much attention to understand the minimum amount of light required to efficiently heat and kill cells simultaneously. These

studies would be important in trying to minimise potential risks when moving forward to *in vivo* studies. Although this study requires much more attention before moving it to the *in vivo* study stage, it is important to try and understand the majority of these details beforehand, which will also ease things as they move forward.

Experimental studies would also need to determine whether heating of the functionalised HGNs affects the DNA attachment onto the HGNs. A previous study by Mackanic *et al.* discussed the release of ssDNA from the NP surface upon irradiation using a 785 nm excitation source.[252] In another study by Borzenkov *et al.,* the temperature related stability of the thiol bond was investigated, in which it was found that increasing the temperature decreased the stability of the thiol bond.[261] Hence, the potentiality exists that during the photothermal experiments, the DNA may start to destabilise. However, further experimentation would need to clarify this.

2D SERRS mapping was successfully carried out to show that the modified HGNs were internalised by the cells, although, the average % SERRS response per cell area was low and would require optimisation of probe concentrations. Comparisons between chol-DNA HGNs and AuNPs could not be investigated by 2D mapping. Hence, this should be considered for future work along with studies where both types of modified nanoparticles are added to the same cell samples to determine if one has an increased uptake over the other. 3D mapping would also need to be carried out to determine successful uptake.

It is also vital to understand the photothermal efficiency of these HGNs. This is the ability of the nanoparticles to convert an absorbed photon into heat. It would be an important study to allow comparisons between different batches of HGNs, and then to also compare their values with those already reported in the literature.[59,254]   This would be very interesting and necessary when moving forward.

5. Concluding Remarks & Future Perspectives

The research presented herein successfully demonstrated the pronounced cellular uptake of cholesterol modified nanoparticles, subsequently exhibiting their bright future as photothermal agents for targeting atherosclerotic plaques.

The first set of experiments saw the successful functionalisation of cholesterol onto spherical AuNPs, using a DNA functionalisation method. This was due to the ease in attaching cholesterol to single-stranded DNA and the facile attachment of this to AuNPs, using thiol as the anchoring body. Analyses included extinction spectroscopy and DLS to determine that cholesterol was on the surface. Kinetic studies also confirmed the stability of these probes, especially for the duration of *in vitro* studies. Time permitting, it would have been interesting to study the conformation of cholesterol once on the surface using computational modelling studies to determine its packing, and this would help in understanding the interactions with cells, which allow it to have enhanced uptake.

The next study highlighted the enhanced uptake of these probes within the cellular environment. The study began with the investigation of these probes in RAWs and using 2D/3D SERRS mapping, highlighting the enhanced uptake in comparison to their control (polyT-DNA AuNPs), evident from the calculated % relative SERRS response. Thereafter, an attempt was made at multiplexing in which both chol-DNA AuNPs and polyT-DNA AuNPs were added simultaneously. This study was unsuccessful due to the Raman reporter on the control. MBA was found to retain its robust signal within the cell and also aggregated within the cellular environment. Future work

should look at using another Raman active dye or reporter with the control. This would be interesting to carry out as it would again highlight the pronounced effect of having cholesterol on the nanoparticle surface. The study with RAWs was used as a 'proof of concept' and also used as a comparison for the study of HUVECs.

Chol-DNA AuNPs in HUVECs again showcased their remarkable characteristic of increased cellular uptake. This work saw a control of pegylated nanoparticles being used, which have routinely been used in literature for cellular studies, and the uptake from them was negligible compared to chol-DNA AuNPs. The % SERRS response from the cholesterol probes was much greater in HUVECs compared to in RAWs. This potentially highlighted the specificity of these fatty nanoparticles with endothelial cells, as also mentioned in the literature, which meant that there was the potential of these being used to specifically target plaque sites *in vivo*. 2D and 3D SERRS mapping were again the modes of analysis here. Reasoning was given for the changes in the vibrational fingerprint from within the cell as possible orientational changes of the MGITC and the attachment of these probes to cellular components. 3D further tried to co-localise the MGITC signal with cellular responses. However, it was found that the MGITC drowned any cellular peaks. It was mentioned that issues with depth profiling remain. This needs further thought and also a route for quantifying the signal. With the 2D mapping, a 'semi-quantitative' approach was utilised. However, extending this approach to 3D would be tedious and very time-consuming. Cell viability studies highlighted the non-toxic ability of these cholesterol conjugates.

With the favourable results, the final results chapter exhibited the potential of using cholesterol modified HGNs as photothermal agents. HGNs exhibited their tuneable LSPR and proficient heating capabilities. They were successfully functionalised with MGITC and chol-DNA. Functionalised HGNs displayed excellent photothermal ablation of HUVECs in comparison to their

bare counterparts, excellently showcasing their ability to be used as photothermal agents in these preliminary studies. However, much work still needs to be carried forward. This approach needs to be optimised with concentrations of probes, laser powers, etc. Attempts have to be made to retain the stability of these modified HGNs as stability studies highlighted the deterioration of the shell.

A greater, in-depth study is needed before these cholesterol modified HGNs can be moved forward as photothermal agents *in vivo*. This work was provided as an initial study into their potential, which was successful.

The attempt to bridge the gap between PTT and CVD was victorious and the research presented within is evidence of that.

6. Experimental

6.1 Functionalisation of Cholesterol Modified Nanoparticles

6.1.1 Materials

Cholesterol-DNA and poly-thymine DNA were purchased from ATDBio. MGITC was purchased from Thermo Fisher Scientific and all other chemicals were purchased from Merck.

6.1.2 Preparation of Buffers

6.1.2.1 Sodium Citrate Buffer

A stock solution of sodium citrate (250 mM, 250 mL) was prepared by dissolving 18.4 g of sodium citrate in Milli-Q water. The pH was adjusted using a Jenway 3510 pH meter, which was calibrated prior to use. Concentrated HCl was used to adjust the pH to 3.

6.1.2.2 Phosphate Buffer Saline with Tween 20™

A resuspending buffer of 0.05% PBST was prepared by first preparing a PBS buffer (0.1 M, 250 mL) by dissolving 1.5 g of sodium chloride and 0.43 g of phosphate buffer in Milli-Q water. The pH of the buffer was checked to make sure it was in the range of 7.2 – 7.4.

A stock of PBST (0.5%, 10 mL) was prepared by adding 50 µL of Tween 20™ to 9.95 mL of PBS and thoroughly shaken. Thereafter, a 0.05% PBST was prepared by adding 1 mL of the prepared 0.5% PBST to 9 mL of PBS. Tween

20™ was too viscous to be pipetted in extremely small volumes, hence the required concentration was made up using serial dilution.

6.1.3 Nanoparticle Synthesis and Functionalisation

6.1.3.1 Preparation of Glassware

Prior to all experiments, glassware was cleaned using a multi-step procedure. This started with a 3 to 4-hour soak in Hellmanex™, followed by rinsing's with ethanol, acetone, and isopropanol. Glassware was then left to soak in *aqua regia* for 4 to 6 hours, which was prepared in-house using nitric (HNO_3) and hydrochloric (HCl) acid, in a ratio of 1:3 respectively. Subsequently, the glassware was rinsed several times with deionised water (d.H_2O) prior to use, and the rinsing's neutralised with sodium carbonate.

6.1.3.2 Colloid Synthesis

A colloidal solution of Au citrate reduced nanoparticles was prepared using a modification of the Turkevich method. Sodium tetrachloroauate (III) dihydrate was added to d.H_2O (60.5 mg, 500 mL) and stirred rapidly. Once boiling, an aqueous solution of sodium citrate (57.5 mg, 7.5 mL) was added quickly to the flask and left to boil for a further 15 minutes in which the solution turned from colourless to a wine-red. After this time, the heat was turned off and the solution cooled, maintaining constant stirring.

6.1.3.3 Optimising the Functionalisation of DNA and Dye to Gold Nanoparticles

In an attempt to deduce the optimum route of functionalising cholesterol DNA and MGITC to AuNPs, two route were studied. In the first study, DNA

in the ratio of 4000:1 (DNA:AuNP) was added and left to shake for one hour. Thereafter, two additions of sodium citrate buffer (250 mM, 30 µL) were made with an interval of 15 minutes between the two, leaving the sample to shake for a further 30 minutes. MGITC (1 µM, 100 µL) was then added prior to centrifuging at 3400 rpm for 10 minutes.

The second route reversed the steps: MGITC (1 µM, 100 µL) being added prior to cholesterol DNA (4000:1), followed by two citrate buffer additions, and a centrifugation step. The second route was chosen as the first route highlighted minimum MGITC on the surface due to the bulky DNA moiety blocking the surface.

6.1.3.4 Conjugation of Cholesterol DNA to Gold Nanoparticles

For all conjugations, AuNPs with a concentration of 96.5 pM were used. To the synthesised citrate AuNps (900 µL), MGITC (1 µM, 100 µL) was added and left to shake for 30 minutes. Cholesterol DNA was added in the ratio of 4000:1 and left to shake for one hour. Thereafter, two additions of sodium citrate buffer (250 mM, 30 µL) were made with an interval of 15 minutes between the two, leaving the sample to shake for a further 30 minutes. The sample was then centrifuged at 3400 rpm for 10 minutes. The resulting pellet was resuspended in PBST (0.05%, 1 mL).

6.1.3.5 Conjugation of PolyT-DNA to Gold Nanoparticles

The protocol described in Section 6.1.3.3 was followed for the functionalisation of PolyT-DNA to AuNPs, which were used as the control. The only difference was the centrifugation step, with these conjugates undergoing a cycle at 4000 rpm for 15 minutes.

6.1.3.6 Conjugation of HS-PEG-5000 to Gold Nanoparticles

Firstly, MGITC (1 µM, 100 µL) was added to AuNPs (900 µL) and left on the shaker for 30 minutes. HS-PEG-5000 (10 µM, 100 µL) was added and left to shake for one hour. Thereafter, two additions of sodium citrate buffer (250 mM, 30 µL) were made with a shaking time of 15 minutes in between and then left again for 30 minutes to shake prior to centrifuging at 4000 rpm for 15 minutes. The conjugates were resuspended in PBST (0.05%, 1 mL).

6.1.3.7 Overcoming the Issue of Solubility with Cholesterol DNA

To overcome the issue of cholesterol and its solubility, a surfactant was added to the resuspending PBS buffer. Different concentrations of Tween 20™ were investigated to determine which would not allow cellular damage and also maintain the solubility of the conjugates. 0.5, 0.1 and 0.05% Tween 20™ were added separately to PBS (0.1 M) and sused to resuspend the prepared conjugates. Subsequently, these were added to cells and using bright field microscopy, determined that 0.05% Tween 20™ in PBS was sufficient to maintain the solubility of the conjugates, with no damage to the cell membrane.

6.1.4 Characterisation Methods

6.1.4.1 Extinction Spectroscopy

Extinction spectra were collected using an Agilent Cary 60 UV-Visible Spectrophotometer with a scan rate of 600 nm/min. Samples were analysed using disposable plastic poly (methyl methacrylate) (PMMA) cuvettes, with a pathlength of 1 cm. Sample were scanned between wavelengths of 400 and 800 nm.

6.1.4.2 Dynamic Light Scattering

A Malvern Zetasizer Nano ZS system was used to collect size data on the bare and functionalised AuNPs. Analysis was carried out in PMMA cuvettes in triplicate. Data were averaged and the standard deviation was calculated using Microsoft® Excel.

6.1.4.3 Zeta-potential Measurements

In order to determine the surface charge of the AuNPs, a Malvern Zetasizer Nano ZS system was used. A 'dip cell' electrode was used to measure the charge of the bare AuNPs, and measurements were obtained in triplicate.

6.1.4.4 Surface Enhanced Raman Spectroscopy Analysis

A Snowy Range (SnRI) Raman spectrometer, with a 638 nm laser excitation, was used to collect SERS spectra. The instrument was calibrated using an ethanol standard prior to data collection. Data was acquired at an integration time of 1 second with a 100% laser power (40 mW) in 4 mL clear glass vials. Analysis was carried out in triplicate and data was processed using MATLAB® software.

6.1.4.5 Scanning Electron Microscopy

For the imaging of nanoparticles, samples were spotted (1 µL) onto a silicon wafer and left to air-dry. They were imaged using a FEI Quanta 250 FEG-ESEM, a field-emission environmental SEM, using an acceleration voltage of 30 kW to capture the images.

6.2 *In Vitro* Studies of Cholesterol Modified Nanoparticles

6.2.1 Cell Culture and Sample Preparation

6.2.1.1 Culturing RAW 264.7 Macrophages

Cells were cultured using Dulbecco's Modified Eagle's Medium (DMEM) (low glucose), supplemented with 1% penicillin/streptomycin, 1% fungizone, and 10% fetal bovine serum (FBS), and were subjected to an atmosphere of 37 ºC and 5% CO_2, in an incubator. Upon reaching *ca.* 90% confluency in a 175 cm^2 flask, the cells were washed with PBS and 6 mL of DMEM was added to the same flask. Cells were lifted by the simple method of scraping and were counted using Trypan Blue. For sample preparation, cells were plated in 6-well plates, containing 22 mm glass slides, at a concentration of 0.4 x 10^6 cells/mL and incubated further for a period of 24 hours. Fresh media and conjugates (6 ρM) were then added to the cells and incubated for a further 3 hours. The cells were then washed with PBS twice, fixed using 500 μL of 4% paraformaldehyde in PBS for 15 minutes before washing with PBS and sterile H_2O twice. Once dried, the coverslips were mounted onto standard glass microscope slides for SERRS mapping.

6.2.1.2 Culturing Human Umbilical Vein Endothelial Cells

Human umbilical vein endothelial cells (HUVECs) were obtained from The University of Glasgow. The cells were cultured in endothelial cell growth medium MV supplied by PromoCell®. The media was supplemented with 1% penicillin/streptomycin and 1% fungizone. The cells were subjected to an atmosphere of 37 ºC and 5% CO_2 in an incubator. At reaching *ca.* 90% confluency in a 175 cm^2 flask, the cells were lifted using the HUVEC cell detach-kit, counted using Trypan Blue, and resuspended in 4 mL of HUVEC

cell growth medium. Cells were plated in 6-well plates, which contained 22 mm glass sides, at a concentration of 0.2×10^6 cell/mL and incubated further for a period of 24 hours. Fresh media and AuNP conjugates (6 ρM) were then added to the cells and incubated for 3 hours in the incubator. Thereafter, cells were washed with PBS twice, fixed using 500 μL of 4% paraformaldehyde in PBS for 10 minutes before washes with PBS and sterile H_2O twice. Once dried, the coverslips were mounted onto standard glass microscope slides for SERRS mapping.

6.2.2 2D and 3D SERRS Mapping of Cells

The fixed cells were mapped using a Renishaw InVia Raman confocal microscope to determine the intracellular uptake of the conjugates. A HeNe 633 nm excitation source with laser powers of 5% (*ca.* 0.2 mW) and 10% (*ca.* 1.2 mW), at 1 second acquisition time per point, an 1800 l/mm grating, and a spectral centre of 1300 cm^{-1} were used to acquire the maps. A N PLAN EPI 50x/0.75 BD magnification objective was also used. The maps were collected in the edge Streamline HR high confocality mode at a 2 μm resolution in the *x* and *y* directions. For the 3D SERRS maps, the volume Streamline high confocality mode was used with a 3 μm resolution in the *x*, *y* and *z* directions.

The data was processed using the Windows-based Raman Environment (WiRE™-Renishaw plc) 4.2 software package. Pre-processing included baseline subtraction and cosmic ray removal. False colour images were generated using direct classical least squares (DCLS) based on the MGITC reference spectrum. Each sample consisted of mapping 10 cells, otherwise stated.

6.2.2.1 Pre-Processing of Collected Maps

Upon data collection, all maps were pre-processed prior to plotting DCLS images. This included baseline correction and cosmic ray removal using the default settings within the WiRE™ 4.2 software. Firstly, every spectra underwent baseline correction which applied the 11th order polynomial fitting. Thereafter cosmic ray removal was carried out which used a near neighbour algorithm to remove sharp spikes in the collected fingerprints. Thereafter, the data was plotted using the DCLS plotting function within the 'Mapping Analysis' function.

6.2.2.2 Calculating the Relative SERRS Response

Due to the challenge in quantifying the number of nanoparticles within a cell, a method was used whereby the % area of SERRS response was calculated using ImageJ from Fiji's image processing package. This would allow for an estimation of the SERRS response per cell area, however, would not be a quantification of the nanoparticles within the cell. This method took into consideration the number of pixels correlating to the SERRS response from the conjugates, referred to as the % relative SERRS response per cell, allowing for comparisons to be made across different samples.

Once each data set was pre-processed, the DCLS plots were generated using WiRE™ 4.2 software, based on the MGITC reference spectrum. The data collected during mapping was fitted to this reference spectrum and according to the degree of spectral fit, a gradient red false colour was assigned. Associated with each data set was a look up table (LUT), which had maximum and minimum values corresponding to the degree of spectral fit. The minimum value was assigned where the spectra indicated a good overlapping with the MGITC reference spectrum. The gradient false colour was converted to monochromatic red colour using WiRE™ 4.2 software package. The subsequent steps were carried out in ImageJ. Using the

snipping tool, the cellular area was selected, which masked everything outside this area. The image was then split into red, blue, and green channels, selecting the monochromatic red channel, where only the red pixels were present. A threshold was set to count the pixels corresponding to the SERRS response only and in this case was set to 150. The percentage of the red pixel area (corresponding to the SERRS response) in relation to the full cell area was then calculated (Figure 6.1).
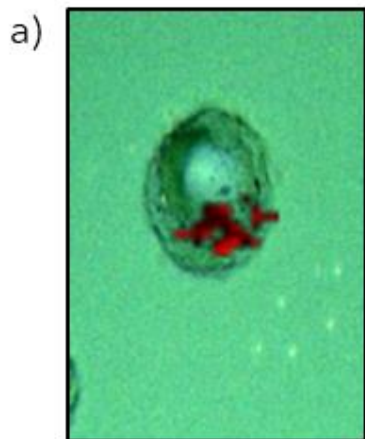
a) DCLS analysis of chol-DNA AuNPs in RAWs, using WiRE™
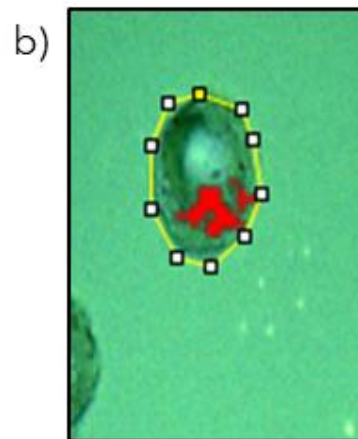
b) False red colour changed to monochromatic red in WiRE™
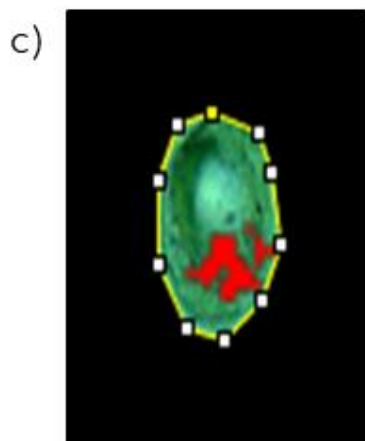
c) Cell area selected in ImageJ
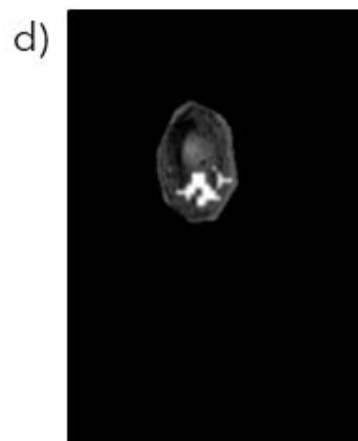
d) Image split into the monochromatic red channel
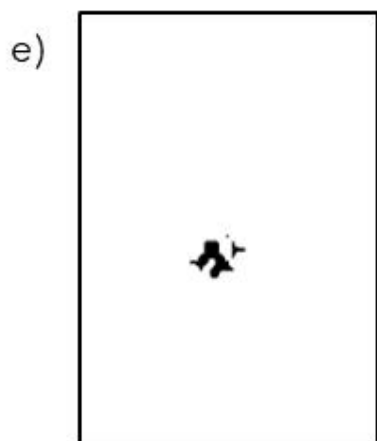
e) Threshold set to 150 so only area correlating to the signal would be counted

f)

Total Area	Average Size	%Area	Mean
300	100	5.783	255

% area of signal calculated

Figure 6.1: Schematic detailing step by step process of calculating the % area of SERRS response: (a) DCLS plots were generated using WiRE™ 4.2 software, (b) the signal was converted to monochromatic red colour using the LUT (look up table), (c) The image was imported into ImageJ (Fiji's image processing software) and the cell area was selected, clearing everything outside the selected area, (d) the image was split to the monochromatic red channel where the red pixels appeared as white spots, (e) the threshold was set to 150 which highlighted the area from the signal as black, (f) the % area of SERRS response versus the cell area was calculated. The data was further statistically analysed using a student's t-test. It should be noted that the cell appears different in size due to cropping, which has displayed the cell as varying in size. However, the cell was the same size during the entire process.

6.2.3 Live Cell Imaging

Cells were plated at a concentration of 0.4 x 10^6 cell/mL in 35 mm glass-bottom dishes purchased from Ibidi®. After a 24-hour incubation period, the chol-DNA AuNPs (6 ρM) were added, subsequently incubating for 3 hours. Thereafter, the cells were washed with PBS twice and fresh media was added. Mapping was carried out as detailed in section 6.2.2. The objective was a Nikon NIR Apo 60x/1.0 w (water immersion).

6.2.4 Multiplexing Using MBA-PolyT-DNA AuNPs

MBA (10 µM, 100 µL) was added to AuNPs (900 µL) and left to shake for 30 minutes. Subsequent steps were carried out as they were for the functionalisation of polyT-DNA AuNPs (sections 6.1.3.3. and 6.1.3.4.). Thereafter, samples for mapping were prepared as detailed in section 6.2.1.1. Chol-DNA and polyT-DNA AuNPs were simultaneously added (3 µM each), and mapping was carried out as described in section 6.2.2.

6.2.5 Cell Viability Studies

6.2.5.1 Trypan Blue Staining Assay

Cells were plated directly in 6-well plates at a concentration of 0.2×10^6 cell/mL and incubated for 24 hours. Thereafter, conjugates were added (6 pM) the cells incubated for a further 3 hours. These were detached from the plates using the HUVEC detach-kit, purchased from PromoCell®. A volume of 10 μL of cells was added to 40 μL of Trypan blue staining solution. Cells were counted using a haemocytometer in duplicate. Each experiment was repeated thrice with three replicates of each sample.

6.2.5.2 Live/Dead® Cell Staining Assay

Cells were plated at a concentration of 0.2×10^6 cell/mL on 22mm glass slides and incubated for 24 hours. Thereafter, cells were subjected to 6 pM of each conjugates (chol-DNA and PEG AuNPs) and incubated for a further 3 hours. Prior to the assay, the cells were washed with PBS twice. A solution of Calcein AM (20 μL, 2mM) and EthD-1 (20 μL, 2mM) were diluted in 10 mL of PBS. The fluorescent staining solution (1 mL) was added to the cells and left at room temperature for 30 minutes. The cover slips were affixed to glass microscope slides with a staining solution layer between the glass layers.

Confocal fluorescence images were acquired using a Leica Microsystems TCS SP8 microscope equipped with a 63x N.A 1.2 HC PL water immersion objective lens. To minimise or eliminate artefacts associated with simultaneous dual wavelength excitation, all dual labelled samples were scanned sequentially in a frame-by-frame format. Firstly, Calcein-AM was imaged using a 488nm argon ion laser (5% laser power) and emission wavelengths were detected using a photonmultiplier tube detector with a gain setting of 650V. Ethd-homodimer was imaged using a 514 nm argon ion laser (5% power) and emission wavelengths were detected using a

second PMT with a gain setting of 650V. All images were acquired across a 512 x 512 frame in 12-bit format. Images were prepared using ImageJ software with scale bars added.

6.3 Hollow Gold Nanoparticles

6.3.1 Hollow Gold Nanoparticle Synthesis

Firstly, the AgNPs were synthesised, which were used as the sacrificial core for HGNs. To a large conical flask, sodium hydroxide (47 mg in 360 mL of d.H_2O) was added along with hydroxylamine hydrochloride (42 mg in 4 mL of d.H_2O). Under rapid stirring, silver nitrate (67 mg in 40 mL of d.H_2O) was added. This was left to stir for 15 minutes under constant stirring and the solution turned yellow-green in colour.

Prior to HGN synthesis, the stock solution of gold was prepared, which comprised of Au and K_2CO_3. Hydrogen tetrachloroaurate (III) (10 mg in 1 mL of d.H_2O) and potassium carbonate (12.5 mg in 50 mL of d. H_2O) were added to a volumetric flask and left for 30 minutes. During this duration, the solution turned from yellow to colourless.

The citrate solution was also prepared which was used as the capping agent. A 50 mg/mL solution was prepared by mixing 1 g of sodium citrate tribasic dihydrate with 20 mL of d.H_2O.

In general, the HGN synthesis involved AgNPs, d.H_2O and Au/K_2CO_3 being added in parts. In the first instance, AgNPs and d.H_2O were magnetically stirred before the Au/K_2CO_3 was added. The resulting solution was left to stir for 5 minutes, after which, the capping agent was added and left stirring for a further 5 minutes. The 'standard' ratio for the HGNs used in the majority of the experimental was 3: 5.5: 1.5, which was 30 mL of AgNPs, 55 mL of d.H_2O and 15 mL of Au/K_2CO_3, together with 2 mL of citrate capping agent. For

some experiments, the ratios varied, and the experiments also scaled. These have been stated accordingly.

6.3.2 Tuning the LSPR of Hollow Gold Nanoparticles

The LSPR of the HGNs could be controlled by adjusting the ratio of the three main components of the synthesis: AgNPs, Au/K_2CO_3 and water. By increasing the Au to Ag ratio, a bathochromic shift in the LSPR could be observed. The following table details the varying ratios which were investigated to obtain the desired LSPR for photothermal studies. The batches are named according to their LSPR as mentioned in section 4.3.1.2.

Batch (nm)	AgNPs (mL)	Water (mL)	Au/K_2CO_3 Solution (mL) Au (0.196 mg/mL) K_2CO_3 (0.245 mg/mL)
718	3	6	1
772	3	5.5	1.5
842	3	5	2
849	3	4	3
850	3	3	4

6.3.3 Characterisation of Hollow Gold Nanoparticles

Primarily, HGNs were characterised using extinction spectroscopy, as mentioned in section 6.1.5.1. The only difference was that samples were analysed between wavelengths of 400 nm and 1100 nm.

Size data was collected using DLS and SEM, as detailed in section 6.1.5.2 and 6.1.5.5 respectively.

6.3.4 Functionalisation of Hollow Gold Nanoparticles

MGITC (1 µM, 100 µM) was added to the synthesised HGNs and left to shake for 30 minutes. Thereafter, DNA (15.8 µM, 40 µL) was added to the MGITC-HGNs and left to shake for one hour. Two subsequent additions of sodium citrate buffer (250 mM, 5 µL) were added with a 15-minute interval for shaking in between. The conjugates were left shaking for another 30 minutes prior to centrifuging at 4000 rpm for 15 minutes and re-suspending in PBST (0.05%, 1 mL).

6.3.5 In-House Photothermal Setup

All photothermal studies were carried out on an in-house built setup which comprised of a CW 785 nm laser excitation source, directed at the sample contained in a glass vial, through a series of mirrors and lens. Temperature recordings were obtained through a K-type thermocouple probe which was inserted into the glass vial and connected to a Picologger for visual readings. All heating studies were carried out at maximum laser power (330 mW) with 30-minute irradiation time.

6.3.6 Photothermal Studies of Hollow Gold Nanoparticles

To determine the heating profile of HGNs and AuNPs, 600 µL of colloidal solution was irradiated in a 1.75 µL glass vial for 30 minutes For cycled heating, the same procedure was carried out, however after 30 minutes of heating, the sample was cooled whilst on the setup for ~15 minutes to allow the sample reach its starting temperature. Thereafter repeating this another 2 times to obtain three replicates. The heating profiles obtained were plotted using Microsoft® Excel and Origin®.

6.3.7 Photothermal Studies of Hollow Gold Nanoparticles *In Vitro*

HUVECs were cultured as mentioned in section 6.2.1.2. These were initially plated at a concentration of 1 x 10^6 cells/mL and incubated for 24 hours. 30 µL of chol-DNA HGNs/HGNs were added to the cells and further incubated for 3 hours. Thereafter, the cells were detached from the plates and counted to prepare samples with an initial cell concentration of 1.5 x 10^6 cells/mL or 1.0 x 10^6 cells/mL in 500 µL aliquots. Where either concentration have been used, this has been stated accordingly. All samples were kept in the incubator until heating. Each sample was irradiated for 30 minutes at a 330 mW laser power. Immediately upon completion of heating, the cells were counted using Trypan Blue staining to determine the remaining cell count. Each sample was counted three times and two/three replicates of each sample were also obtained to allow for an average and standard deviation to be calculated.

6.3.8 2D SERRS Mapping of Cholesterol Modified Nanoshells *In Vitro*

HUVECs were cultured and plated as described in section 6.2.1.2. After a 24-hour incubation period, 30 µL of chol-DNA HGNs were added to the cells and incubated for a further 3 hours. Thereafter, the slides were washed, and the cells fixed down using the remaining procedure mentioned in section 6.2.1.2. Mapping was carried out as detailed in section 6.2.2 and the % SERRS response was calculated using the procedure mentioned in section 6.2.2.2.

6.3.9 Cell Viability Studies of Bare and Functionalised Hollow Gold Nanoparticles

Cell toxicity studies were carried out as detailed in section 6.2.5.1. The only difference was that 30 μL of bare/functionalised HGNs were added to HUVECs. Experiments were carried out thrice with three replicates of each sample.

References

1   BHF-Heart   Statistics,   https://www.bhf.org.uk/what-we-do/our-research/heart-statistics, (accessed 27 January 2020).

2   World   Health   Organization,   https://www.who.int/health-topics/cardiovascular-diseases/#tab=tab_1, (accessed 27 January 2020).

3   W. Insull, *Am. J. Med.*, 2009, 122, S3–S14.

4   P. P. Toth, *Int. J. Clin. Pract.*, 2008, 62, 1246–1254.

5   P. Libby, P. M. Ridker and G. K. Hansson, *Nature*, 2011, 473, 317–325.

6   A. J. Lusis, *Nature*, 2010, 407, 233–241.

7   W. Martinet, D. M. Schrijvers and G. R. Y. De Meyer, *Basic Res. Cardiol.*, 2012, 107, 1–12.

8   G. J. Tortora and B. H. Derrickson, *Tortora's Principles of Anatomy and Physiology*, John Wiley and Sons, Global Edi.

9   A. Zampelas and E. Magriplis, *Nutrients*, 2019, 11, 1–4.

10   B. Bagheri, A. Alikhani, H. Mokhtari and M. Rasouli, *Med. Arch. (Sarajevo, Bosnia Herzegovina)*, 2018, 72, 103–107.

11   F. R. Maxfield and G. van Meer, *Curr. Opin. Cell Biol.*, 2010, 22, 422–429.

12   A. Mu, *Atherosclerosis: Risks, mechanisms and therapies*, John Wiley and Sons, 2015, vol. 53.

13   J. L. Goldstein and M. S. Brown, *Arterioscler. Thromb. Vasc Biol*, 2010, 29, 431–438.

14   R. B. Singh, S. A. Mengi, Y. J. Xu, A. S. Arneja and N. S. Dhalla, *Exp. Clin. Cardiol.*, 2002, 7, 40–53.

15   E. M. M. Besterman, *Br. Med. J.*, 1958, 1, 159–160.

16   I. E. Konstantinov and G. M. Jankovic, *Texas Hear. Inst. J.*, 2013, 40, 247–249.

17   I. E. Konstantinov, N. Mejevoi and N. M. Anichkov, *Texas Hear. Inst. J.*, 2006, 33, 417–423.

18   B. Sadowitz, K. G. Maier and V. Gahtan, *Vasc. Endovascular Surg.*, 2010, 44, 241–251.

19   M. Schachter, *Fundam. Clin. Pharmacol.*, 2005, 19, 117–125.

20   M. Jasińska, J. Owczarek and D. Orszulak-Michalak, *Pharmacol. Reports*, 2007, 59, 483–499.

21   A. J. Taylor, S. M. Kent, P. J. Flaherty, L. C. Coyle, T. T. Markwood and M. N. Vernalis, *Circulation*, 2002, 106, 2055–2060.

22   T. J. Smilde, S. Van Wissen, H. Wollersheim, M. D. Trip, J. J. P. Kastelein and A. F. H. Stalenhoef, *Lancet*, 2001, 357, 577–581.

23   J. S. Raichlen, W. a Riley, G. W. Evans, M. K. Palmer and D. H. O. Leary, *Jama*, 2007, 297, 1344–1353.

24   Coronary Heart Disease Treatment, https://www.nhs.uk/conditions/coronary-heart-disease/treatment/, (accessed 10 July 2020).

25   R. M. S. S. A. Almeida, F. Biscegli, J. Editors, N. Ribeiro, P. De Sousa, G. Romero, L. · Marcus, R. Monteiro, L. Nogueira and B. Associate, *Cardiovascular Surgery A Clinical Casebook*, Springer, 2019.

26   A. N. Kharlamov, A. E. Tyurnina, V. S. Veselova, O. P. Kovtun, V. Y. Shur and J. L. Gabinsky, *Nanoscale*, 2015, 7, 8003–8015.

27 J. B. Vines, J. H. Yoon, N. E. Ryu, D. J. Lim and H. Park, *Front. Chem.*, 2019, 7, 1–16.

28 R. . Feynman, in *Caltech Engineering and Science*, 1960, vol. 16, pp. 22–36.

29 S. K. Sahoo, S. Parveen and J. J. Panda, *Nanomedicine Nanotechnology, Biol. Med.*, 2007, 3, 20–31.

30 S. K. Murthy, *Int. J. Nanomedicine*, 2007, 2, 129–41.

31 S. Shrivastava and D. Dash, *J. Nanotechnol.*, 2009, 2009, 1–14.

32 G. Walters and I. P. Parkin, *J. Mater. Chem.*, 2009, 19, 574–590.

33 S. Eustis and M. A. El-Sayed, *Chem. Soc. Rev.*, 2006, 35, 209–217.

34 I. Freestone, N. Meeks, M. Sax and C. Higgitt, *Gold Bull.*, 2007, 40, 270–277.

35 M. Faraday, *Phil. Trans. R. Soc.*, 1857, 147, 145–181.

36 Y. Fu, P. Li, Q. Xie, X. Xu, L. Lei, C. Chen, C. Zou, W. Deng and S. Yao, *Adv. Funct. Mater.*, 2009, 19, 1784–1791.

37 J. Li, L. Liu, D. Zhang, D. Yang, J. Guo and J. Wei, *Synth. Met.*, 2014, 192, 15–22.

38 J. Singh, T. Dutta, K. H. Kim, M. Rawat, P. Samddar and P. Kumar, *J. Nanobiotechnology*, 2018, 16, 1–24.

39 L. Rodríguez-Sánchez, M. C. Blanco and M. A. López-Quintela, *J. Phys. Chem. B*, 2000, 104, 9683–9688.

40 K. L. McGilvray, M. R. Decan, D. Wang and J. C. Scaiano, *J. Am. Chem. Soc.*, 2006, 128, 15980–15981.

41 H. Kawasaki, *Nanotechnol. Rev.*, 2013, 2, 5–25.

42 K. W. Choi, D. Y. Kim, S. J. Ye and O. O. Park, *Adv. Mater. Res.*, 2014,

3, 199–216.

43   J. Turkevich, P. C. Stevenson and J. Hillier, *Discuss. Faraday Soc.*, 1951, 11, 55–75.

44   G. FRENS, *Nat. Phys. Sci.*, 1973, 241, 20–22.

45   H. Xia, Y. Xiahou, P. Zhang, W. Ding and D. Wang, *Langmuir*, 2016, 32, 5870–5880.

46   L. M. Liz-Marzán, *Chem. Commun.*, 2013, 49, 16–18.

47   M. Brust, M. Walker, D. Bethell, D. J. Schiffrin and R. Whyman, *J. Chem. Soc. Chem. Commun.*, 1994, 801–802.

48   S. D. Perrault and W. C. W. Chan, *J. Am. Chem. Soc.*, 2009, 131, 17042–17043.

49   K. M. Mayer and J. H. Hafner, *Chem. Rev.*, 2011, 111, 3828–3857.

50   X. Huang and M. A. El-Sayed, *J. Adv. Res.*, 2010, 1, 13–28.

51   X. D. Hoa, A. G. Kirk and M. Tabrizian, *Biosens. Bioelectron.*, 2007, 23, 151–160.

52   G. Mie, *Ann. Phys.*, 1908, 25, 377–452.

53   P. Newman, *Contributions on the optics of turbid media, particularly colloidal metal solutions*, Albuquerque, New Mexico, 1908, vol. 25.

54   M. Hu, J. Chen, Z.-Y. Li, L. Au, G. V. Hartland, X. Li, M. Marquez and Y. Xia, *Chem. Soc. Rev.*, 2006, 35, 1084.

55   T. Klar, M. Perner, S. Grosse, G. von Plessen, W. Spirkl and J. Feldmann, *Phys. Rev. Lett.*, 1998, 80, 4249–4252.

56   F. S. Ameer, S. Varahagiri, D. W. Benza, D. R. Willett, Y. Wen, F. Wang, G. Chumanov and J. N. Anker, *J. Phys. Chem. C*, 2016, 120, 20886–20895.

57 A. Guerrero-Martínez, S. Barbosa, I. Pastoriza-Santos and L. M. Liz-Marzán, *Curr. Opin. Colloid Interface Sci.*, 2011, 16, 118–127.

58 L. Rodríguez-Lorenzo, J. M. Romo-Herrera, J. Pérez-Juste, R. A. Alvarez-Puebla and L. M. Liz-Marzán, *J. Mater. Chem.*, 2011, 21, 11544–11549.

59 H. N. Xie, I. A. Larmour, Y. C. Chen, A. W. Wark, V. Tileli, D. W. McComb, K. Faulds and D. Graham, *Nanoscale*, 2012, 5, 765–771.

60 K. A. Willets and R. P. Van Duyne, *Annu. Rev. Phys. Chem.*, 2007, 58, 267–297.

61 W. Haiss, N. T. K. Thanh, J. Aveyard and D. G. Fernig, *Anal. Chem.*, 2007, 79, 4215–4221.

62 S. Agnihotri, S. Mukherji and S. Mukherji, *RSC Adv.*, 2014, 4, 3974–3983.

63 C. A. Mirkin, R. L. Letsinger, R. C. Mucic and J. J. Storhoff, *Nature*, 1996, 382, 607–609.

64 B. G. Ershov, E. V. Abkhalimov, R. D. Solovov and V. I. Roldughin, *Phys. Chem. Chem. Phys.*, 2016, 18, 13459–13466.

65 V. Wagner, A. Dullaart, A. K. Bock and A. Zweck, *Nat. Biotechnol.*, 2006, 24, 1211–1217.

66 C. K. W. Chan, L. Zhang, C. K. Cheng, H. Yang, Y. Huang, X. Y. Tian and C. H. J. Choi, *Small*, 2018, 14, 1–16.

67 N. D. James, R. J. Coker, D. Tomlinson, J. R. W. Harris, M. Gompels, A. J. Pinching and J. S. W. Stewart, *Clin. Oncol.*, 1994, 6, 294–296.

68 D. Bobo, K. J. Robinson, J. Islam, K. J. Thurecht and S. R. Corrie, *Pharm. Res.*, 2016, 33, 2373–2387.

69 D. Graham, R. Stevenson, D. G. Thompson, L. Barrett, C. Dalton and K.

Faulds, *Faraday Discuss.*, 2011, 149, 291–299.

70   A. Kapara, University of Strathclyde, 2019.

71   R. Kozlowski, A. Ragupathi and R. B. Dyer, *Bioconjug. Chem.*, 2018, 29, 2691–2700.

72   D. Öztekin Long, Nicole, M and Badre, *Nat Rev Drug Discov.*, 2013, 10, 835--852.

73   J. R. McCarthy, *Curr. Cardiovasc. Imaging Rep.*, 2010, 3, 42–49.

74   J. Noonan, S. M. Asiala, G. Grassia, N. MacRitchie, K. Gracie, J. Carson, M. Moores, M. Girolami, A. C. Bradshaw, T. J. Guzik, G. R. Meehan, H. E. Scales, J. M. Brewer, I. B. McInnes, N. Sattar, K. Faulds, P. Garside, D. Graham and P. Maffia, *Theranostics*, 2018, 8, 6195–6209.

75   M. W. Meyers, J. S. Rink, Q. Jiang, M. E. Kelly, J. M. Vercammen, C. S. Thaxton and M. R. Kibbe, *Physiol. Rep.*, 2017, 5, 1–16.

76   N. Kamaly, G. Fredman, J. J. R. Fojas, M. Subramanian, W. I. Choi, K. Zepeda, C. Vilos, M. Yu, S. Gadde, J. Wu, J. Milton, R. Carvalho Leitao, L. Rosa Fernandes, M. Hasan, H. Gao, V. Nguyen, J. Harris, I. Tabas and O. C. Farokhzad, *ACS Nano*, 2016, 10, 5280–5292.

77   Y. Zhao, A. Dunn, J. Lin and D. Shi, *Photothermal Effect of Nanomaterials for Efficient Energy Applications*, Elsevier Inc., 2018.

78   X. Huang, P. K. Jain, I. H. El-Sayed and M. A. El-Sayed, *Lasers Med. Sci.*, 2008, 23, 217–228.

79   J. Pašta, *Laser therapy in ophthalmology*, Woodhead Publishing Limited, 2013.

80   J. L. Bacon, *Lasers in gynecology*, Woodhead Publishing Limited, 2013.

81   E. N. Sobol, A. B. Shekhter and A. V. Baskov, *Lasers in orthopaedic*

surgery, Woodhead Publishing Limited, 2013.

82   X. Huang and M. A. El-Sayed, *Alexandria J. Med.*, 2011, 47, 1–9.

83   S. Link and M. A. El-Sayed, *Annu. Rev. Phys. Chem.*, 2003, 54, 331–366.

84   S. Link and M. A. El-Sayed, *Int. Rev. Phys. Chem.*, 2000, 19, 409–453.

85   P. E. McGuff, R. A. Deterling, L. S. Gottlieb, H. D. Fahimi and D. Bushnell, *Ann. Surg.*, 1964, 160, 765–777.

86   I. Cicha, C. Chauvierre, I. Texier, C. Cabella, J. M. Metselaar, J. Szebeni, L. Dézsi, C. Alexiou, F. Rouzet, G. Storm, E. Stroes, D. Bruce, N. MacRitchie, P. Maffia and D. Letourneur, *Cardiovasc. Res.*, 2018, 114, 1714–1727.

87   D. Yeager, Y. S. Chen, S. Litovsky and S. Emelianov, *Theranostics*, 2014, 4, 36–46.

88   E. Smith and G. Dent, *Modern Raman Spectroscopy: A Practical Approach*, 2005.

89   M. M. Harper, K. S. McKeating and K. Faulds, *Phys. Chem. Chem. Phys.*, 2013, 15, 5312–5328.

90   A. Paudel, D. Raijada and J. Rantanen, *Adv. Drug Deliv. Rev.*, 2015, 89, 3–20.

91   R. A. Halvorson and P. J. Vikesland, *Environ. Sci. Technol.*, 2010, 44, 7749–7755.

92   D. W. Li, W. L. Zhai, Y. T. Li and Y. T. Long, *Microchim. Acta*, 2014, 181, 23–43.

93   A. Smekel, *Naturwissenschaften*, 1923, 11, 873–875.

94   C. V RAMAN and K. S. KRISHNAN, *Nature*, 1928, 121, 501.

95   F. A. Miller and G. B. Kauffman, *J. Chem. Educ.*, 1989, 66, 795–801.

96   N. John and S. George, *Spectroscopic Methods for Nanomaterials Characterization*, Elsevier Inc., 2017, vol. 2.

97   E. V. Efremov, F. Ariese and C. Gooijer, *Anal. Chim. Acta*, 2008, 606, 119–134.

98   M. Fleischmann, P. J. Hendra and A. J. McQuillan, *Chem. Phys. Lett.*, 1974, 26, 163–166.

99   D. L. Jeanmaire and R. P. Van Duyne, *J. Electroanal. Chem.*, 1977, 84, 1–20.

100   M. G. Albrecht and J. A. Creighton, *J. Am. Chem. Soc.*, 1977, 99, 5215–5217.

101   A. Campion, P. Kambhampati, A. Campion and C. Harris, *Chem. Soc. Rev.*, 1998, 27, 241–250.

102   G. McNay, D. Eustace, W. E. Smith, K. Faulds and D. Graham, *Appl. Spectrosc.*, 2011, 65, 825–837.

103   M. Moskovits, *Rev. Mod. Phys.*, 1985, 57, 783–826.

104   K. Kneipp, H. Kneipp, I. Itzkan, R. R. Dasari and M. S. Feld, *Chem. Rev.*, 1999, 99, 2957–2975.

105   J. R. Lombardi and R. L. Birke, *Acc. Chem. Res.*, 2009, 42, 734–742.

106   W. Xie, B. Walkenfort and S. Schlücker, *J. Am. Chem. Soc.*, 2013, 135, 1657–1660.

107   L. Rocks, K. Faulds and D. Graham, *Chem. Commun.*, 2011, 47, 4415–4417.

108   T. B. Nguyen, T. K. Thu Vu, Q. D. Nguyen, T. D. Nguyen, T. A. Nguyen and T. H. Trinh, *Adv. Nat. Sci. Nanosci. Nanotechnol.*, 2012, 3, 1–5.

109   S. Tian, O. Neumann, M. J. McClain, X. Yang, L. Zhou, C. Zhang, P. Nordlander and N. J. Halas, *Nano Lett.*, 2017, 17, 5071–5077.

110   S. Mabbott, S. C. Fernandes, M. Schechinger, G. L. Cote, K. Faulds, C. R. Mace and D. Graham, *Analyst*, 2020, 145, 983–991.

111   H. Chon, S. Lee, S. Y. Yoon, E. K. Lee, S. I. Chang and J. Choo, *Chem. Commun.*, 2014, 50, 1058–1060.

112   H. Kearns, R. Goodacre, L. E. Jamieson, D. Graham and K. Faulds, *Anal. Chem.*, 2017, 89, 12666–12673.

113   K. K. Maiti, A. Samanta, M. Vendrell, K. S. Soh, M. Olivo and Y. T. Chang, *Chem. Commun.*, 2011, 47, 3514–3516.

114   K. Milligan, N. C. Shand, D. Graham and K. Faulds, *Anal. Chem.*, 2020, 92, 3253–3261.

115   J. Langer, D. J. de Aberasturi, J. Aizpurua, R. A. Alvarez-Puebla, B. Auguié, J. J. Baumberg, G. C. Bazan, S. E. J. Bell, A. Boisen, A. G. Brolo, J. Choo, D. Cialla-May, V. Deckert, L. Fabris, K. Faulds, F. Javier García de Abajo, R. Goodacre, D. Graham, A. J. Haes, C. L. Haynes, C. Huck, T. Itoh, M. Käll, J. Kneipp, N. A. Kotov, H. Kuang, E. C. Le Ru, H. K. Lee, J. F. Li, X. Y. Ling, S. A. Maier, T. Mayerhöfer, M. Moskovits, K. Murakoshi, J. M. Nam, S. Nie, Y. Ozaki, I. Pastoriza-Santos, J. Perez-Juste, J. Popp, A. Pucci, S. Reich, B. Ren, G. C. Schatz, T. Shegai, S. Schlücker, L. L. Tay, K. George Thomas, Z. Q. Tian, R. P. van Duyne, T. Vo-Dinh, Y. Wang, K. A. Willets, C. Xu, H. Xu, Y. Xu, Y. S. Yamamoto, B. Zhao and L. M. Liz-Marzán, *ACS Nano*, 2020, 14, 28–117.

116   S. McAughtrie, K. Faulds and D. Graham, *J. Photochem. Photobiol. C Photochem. Rev.*, 2014, 21, 40–53.

117   M. Fan, G. F. S. Andrade and A. G. Brolo, *Anal. Chim. Acta*, 2020, 1097, 1–29.

118   A. A. Stacy and R. P. Van Duyne, *Chem. Phys. Lett.*, 1983, 102, 365–370.

119 X. Qian, S. R. Emory and S. Nie, *J. Am. Chem. Soc.*, 2012, 134, 2000–2003.

120 L. Barrett, J. A. Dougan, K. Faulds and D. Graham, *Nanoscale*, 2011, 3, 3221–3227.

121 L. E. Jamieson, J. Greaves, J. A. McLellan, K. R. Munro, N. C. O. Tomkinson, L. H. Chamberlain, K. Faulds and D. Graham, *Spectrochim. Acta - Part A Mol. Biomol. Spectrosc.*, 2018, 197, 30–36.

122 G. J. Puppels, F. F. M. de Mul, C. Otto, J. Greve, M. Robert-Nicoud, D. J. Arndt-Jovin and T. M. Jovin, *Nature*, 1990, 347, 301–303.

123 R. Smith, K. L. Wright and L. Ashton, *Analyst*, 2016, 141, 3590–3600.

124 K. Majzner, A. Kaczor, N. Kachamakova-Trojanowska, A. Fedorowicz, S. Chlopicki and M. Baranska, *Analyst*, 2013, 138, 603–610.

125 J. Pan, T. Cha, H. Chen, F. Li and J. H. Choi, *3D DNA Nanostructure*, 2017, vol. 1500.

126 A. P. Alivisatos, K. P. Johnsoon, X. Peng, T. E. Wilson, C. J. Loweth, M. P. Bruchez Jr and P. G. Schultz, *Nature*, 1996, 382, 609–611.

127 M. Cárdenas, J. Barauskas, K. Schullén, J. L. Brennan, M. Brust and T. Nylander, *Langmuir*, 2006, 22, 3294–3299.

128 S. Dhar, W. L. Daniel, D. A. Giljohann, C. A. Mirkin and S. J. Lippard, *J. Am. Chem. Soc.*, 2009, 131, 14652–14653.

129 N. L. Rosi, D. A. Giljohann, C. S. Thaxton, A. K. R. Lytton-Jean, M. S. Han and C. A. Mirkin, *Oligonucleotide-modified gold nanoparticles for infracellular gene regulation*, 2006, vol. 312.

130 L. Poon, W. Zandberg, D. Hsiao, Z. Erno, D. Sen, B. D. Gates and N. R. Branda, *ACS Nano*, 2010, 4, 6395–6403.

131 R. Huschka, J. Zuloaga, M. W. Knight, L. V. Brown, P. Nordlander and

N. J. Halas, *J. Am. Chem. Soc.*, 2011, 133, 12247–12255.

132 M. Raouane, D. Desmaële, G. Urbinati, L. Massaad-Massade and P. Couvreur, *Bioconjug. Chem.*, 2012, 23, 1091–1104.

133 A. Khmelinskaia, J. Mücksch, E. P. Petrov, H. G. Franquelim and P. Schwille, *Langmuir*, 2018, 34, 14921–14931.

134 A. Khmelinskaia, M. Ibarguren, R. F. M. De Almeida, D. J. López, V. A. Paixão, H. Ahyayauch, F. M. Goñi and P. V. Escribá, *Langmuir*, 2014, 30, 2117–2128.

135 N. Wu, F. Chen, Y. Zhao, X. Yu, J. Wei and Y. Zhao, *Langmuir*, 2018, 34, 14721–14730.

136 W. L. Whitehouse, J. E. Noble, M. G. Ryadnov and S. Howorka, *Bioconjug. Chem.*, 2019, 30, 1836–1844.

137 Z. Zhang, Y. Yang, F. Pincet, M. C. Llaguno and C. Lin, *Nat. Chem.*, 2017, 9, 653–659.

138 H. G. Franquelim, A. Khmelinskaia, J. P. Sobczak, H. Dietz and P. Schwille, *Nat. Commun.*, 2018, 9, 1–10.

139 Y. F. Tian, C. F. Ning, F. He, B. C. Yin and B. C. Ye, *Analyst*, 2018, 143, 4915–4922.

140 P. Foroozandeh and A. A. Aziz, *Nanoscale Res. Lett.*, 2018, 13, 1–12.

141 F. Zhao, Y. Zhao, Y. Liu, X. Chang, C. Chen and Y. Zhao, *Small*, 2011, 7, 1322–1337.

142 A. Johnson-Buck, S. Jiang, H. Yan and N. G. Walter, *ACS Nano*, 2014, 8, 5641–5649.

143 A. Bunge, M. Loew, P. Pescador, A. Arbuzova, N. Brodersen, J. Kang, L. Dähne, J. Liebscher, A. Herrmann, G. Stengel and D. Huster, *J. Phys. Chem. B*, 2009, 113, 16425–16434.

144 M. Banchelli, F. Betti, D. Berti, G. Caminati, F. B. Bombelli, T. Brown, L. Marcus Wilhelmsson, B. Norden and P. Baglioni, *J. Phys. Chem. B*, 2008, 112, 10942–10952.

145 I. Pfeiffer and F. Höök, *J. Am. Chem. Soc.*, 2004, 126, 10224–10225.

146 C. M. Goodman, C. D. McCusker, T. Yilmaz and V. M. Rotello, *Bioconjug. Chem.*, 2004, 15, 897–900.

147 Y. Zhang, D. Xu, W. Li, J. Yu and Y. Chen, *J. Nanomater.*, 2012, 2012, 1–7.

148 E. Boisselier and D. Astruc, *Chem. Soc. Rev.*, 2009, 38, 1759–1782.

149 B. Klębowski, J. Depciuch, M. Parlińska-Wojtan and J. Baran, *Int. J. Mol. Sci.*, 2018, 19, 1–17.

150 S. Hong and X. Li, *J. Nanomater.*, 2013, 2013, 1–9.

151 J. Turkevich, P. C. Stevenson and J. Hillier, *Discuss. Faraday Soc.*, 1951, 11, 55.

152 S. Bhattacharjee, *J. Control. Release*, 2016, 235, 337–351.

153 E. Tomaszewska, K. Soliwoda, K. Kadziola, B. Tkacz-Szczesna, G. Celichowski, M. Cichomski, W. Szmaja and J. Grobelny, *J. Nanomater.*, 2013, 2013, 1–10.

154 A. E. Vladár and V. D. Hodoroaba, *Characterization of nanoparticles by scanning electron microscopy*, Elsevier Inc., 2019.

155 M. I. Ltd., *Zetasizer Nano Series User Manual: Issue 2.1*, 2004.

156 F. Li, H. Zhang, B. Dever, X. F. Li and X. C. Le, *Bioconjug. Chem.*, 2013, 24, 1790–1797.

157 E. Pensa, E. Cortés, G. Corthey, P. Carro, C. Vericat, M. H. Fonticelli, G. Benítez, A. A. Rubert and R. C. Salvarezza, *Acc. Chem. Res.*, 2012, 45, 1183–1192.

158   R. A. Haraszti, R. Miller, M. C. Didiot, A. Biscans, J. F. Alterman, M. R. Hassler, L. Roux, D. Echeverria, E. Sapp, M. DiFiglia, N. Aronin and A. Khvorova, *Mol. Ther.*, 2018, 26, 1973–1982.

159   X. Zhang, B. Liu, N. Dave, M. R. Servos and J. Liu, *Langmuir*, 2012, 28, 17053–17060.

160   J. J. Storhoff, R. Elghanian, C. A. Mirkin and R. L. Letsinger, *Langmuir*, 2002, 18, 6666–6670.

161   J. M. Carnerero, A. Sánchez-Coronilla, E. I. Martín, A. Jimenez-Ruiz and R. Prado-Gotor, *Phys. Chem. Chem. Phys.*, 2017, 19, 22121–22128.

162   R. Bar-Ziv and A. Libchaber, *Proc. Natl. Acad. Sci. U. S. A.*, 2001, 98, 9068–9073.

163   J. J. Storhoff, R. Elghanian, R. C. Mucic, C. A. Mirkin and R. L. Letsinger, *J. Am. Chem. Soc.*, 1998, 120, 1959–1964.

164   R. Elghanian, J. J. Storhoff, R. C. Mucic, R. L. Letsinger and C. A. Mirkin, *Science (80-.).*, 1997, 277, 1078–1081.

165   X. Zhang, M. R. Servos and J. Liu, *J. Am. Chem. Soc.*, 2012, 134, 7266–7269.

166   W. Haiss, N. T. K. Thanh, J. Aveyard and D. G. Fernig, *Anal. Chem.*, 2007, 79, 4215–4221.

167   X. Qian, S. R. Emory and S. Nie, *J. Am. Chem. Soc.*, 2012, 134, 2000–2003.

168   D. Graham, D. G. Thompson, W. E. Smith and K. Faulds, *Nat. Nanotechnol.*, 2008, 3, 548–551.

169   F. McKenzie and D. Graham, *Chem. Commun.*, 2009, 5757–5759.

170   A. Kamińska, I. Dzicielewski, J. L. Weyher, J. Waluk, S. Gawinkowski, V. Sashuk, M. Fiałkowski, M. Sawicka, T. Suski, S. Porowski and R. Hołyst,

J. Mater. Chem., 2011, 21, 8662–8669.

171   M. Schechinger, H. Marks, S. Mabbott, M. Choudhury and G. Cote, *Analyst*, 2019, 144, 4033–4044.

172   G. Wang and W. Sun, *J. Phys. Chem. B*, 2006, 110, 20901–20905.

173   S. Christau, T. Moeller, J. Genzer, R. Koehler and R. Von Klitzing, *Macromolecules*, 2017, 50, 7333–7343.

174   Sigma-Aldrich   Tween   20, https://www.sigmaaldrich.com/catalog/product/sial/p1379?lang=en&region=GB, (accessed 7 August 2020).

175   D. DIMITRIJEVIC, A. J. SHAW and A. T. FLORENCE, *J. Pharm. Pharmacol.*, 2000, 52, 157–162.

176   J. Pérez-Juste, I. Pastoriza-Santos, L. M. Liz-Marzán and P. Mulvaney, *Coord. Chem. Rev.*, 2005, 249, 1870–1901.

177   Y. Xia, W. Li, C. M. Cobley, J. Chen, X. Xia, Q. Zhang, M. Yang, E. C. Cho and P. K. Brown, *Acc. Chem. Res.*, 2011, 44, 914–924.

178   L. Scarabelli, M. Coronado-Puchau, J. J. Giner-Casares, J. Langer and L. M. Liz-Marzán, *ACS Nano*, 2014, 8, 5833–5842.

179   X. Xie, J. Liao, X. Shao, Q. Li and Y. Lin, *Sci. Rep.*, 2017, 7, 1–9.

180   B. D. Chithrani, A. A. Ghazani and W. C. W. Chan, *Nano Lett.*, 2006, 6, 662–668.

181   J. Zhao, H. Lu, S. Wong, M. Lu, P. Xiao and M. H. Stenzel, *Polym. Chem.*, 2017, 8, 3317–3326.

182   Y. J. Lee, E. Y. Ahn and Y. Park, *Nanoscale Res. Lett.*, 2019, 14, 1–14.

183   S. Behzadi, V. Serpooshan, W. Tao, M. A. Hamaly, M. Y. Alkawareek, E. C. Dreaden, D. Brown, A. M. Alkilany, O. C. Farokhzad and M. Mahmoudi, *Chem. Soc. Rev.*, 2017, 46, 4218–4244.

184 N. D. Donahue, H. Acar and S. Wilhelm, *Adv. Drug Deliv. Rev.*, 2019, 143, 68–96.

185 L. Kou, J. Sun, Y. Zhai and Z. He, *Asian J. Pharm. Sci.*, 2013, 8, 1–10.

186 F. Osaki, T. Kanamori, S. Sando, T. Sera and Y. Aoyama, *J. Am. Chem. Soc.*, 2004, 126, 6520–6521.

187 I. J. Goldberg and K. E. Bornfeldt, *Curr. Atheroscler. Rep.*, 2013, 15, 365.

188 X. Li, O. Gonzalez, X. Shen, S. Barnhart, F. Kramer, J. E. Kanter, A. Vivekanandan-Giri, K. Tsuchiya, P. Handa, S. Pennathur, F. Kim, R. A. Coleman, J. E. Schaffer and K. E. Bornfeldt, *Arterioscler. Thromb. Vasc. Biol.*, 2013, 33, 232–240.

189 H. Mitsutake, R. J. Poppi and M. C. Breitkreitz, *J. Braz. Chem. Soc.*, 2019, 30, 2243–2258.

190 F. Nicolson, L. E. Jamieson, S. Mabbott, K. Plakas, N. C. Shand, M. R. Detty, D. Graham and K. Faulds, *Chem. Sci.*, 2018, 9, 3788–3792.

191 F. Nicolson, B. Andreiuk, C. Andreou, H. T. Hsu, S. Rudder and M. F. Kircher, *Theranostics*, 2019, 9, 5899–5913.

192 I. R. Nabiev, H. Morjani and M. Manfait, *Eur. Biophys. J.*, 1991, 19, 311–316.

193 S. Laing, K. Gracie and K. Faulds, *Chem. Soc. Rev.*, 2016, 45, 1901–1918.

194 N. MacRitchie, G. Grassia, J. Noonan, P. Garside, D. Graham and P. Maffia, *Heart*, 2017, 0, 1–8.

195 S. McAughtrie, K. Lau, K. Faulds and D. Graham, *Chem. Sci.*, 2013, 4, 3566–3572.

196 Z. Li, L. Sun, Y. Zhang, A. P. Dove, R. K. O'Reilly and G. Chen, *ACS*

Macro Lett., 2016, 5, 1059–1064.

197   J. Zhao and M. H. Stenzel, *Polym. Chem.*, 2018, 9, 259–272.

198   A. Kapara, V. Brunton, D. Graham and K. Faulds, *Chem. Sci.*, 2020, 11, 5819–5829.

199   J. H. Kang and Y. T. Ko, *Int. J. Nanomedicine*, 2015, 10, 33–45.

200   C. Lorenz, P. Hadwiger, M. John, H. P. Vornlocher and C. Unverzagt, *Bioorganic Med. Chem. Lett.*, 2004, 14, 4975–4977.

201   H. J. Lee, W. Zhang, D. Zhang, Y. Yang, B. Liu, E. L. Barker, K. K. Buhman, L. V. Slipchenko, M. Dai and J. X. Cheng, *Sci. Rep.*, 2015, 5, 1–3.

202   J. A. Olzmann and P. Carvalho, *Nat. Rev. Mol. Cell Biol.*, 2019, 20, 137–155.

203   K. C. Huang, K. Bando, J. Ando, N. I. Smith, K. Fujita and S. Kawata, *Methods*, 2014, 68, 348–353.

204   F. Krombach, S. Münzing, A. M. Allmeling, J. T. Gerlach, J. Behr and M. Dörger, *Environ. Health Perspect.*, 1997, 105 Suppl, 1261–1263.

205   A. N. Kuzmin, A. Pliss and P. N. Prasad, *Anal. Chem.*, 2014, 86, 10909–10916.

206   A. Jaworska, L. E. Jamieson, K. Malek, C. J. Campbell, J. Choo, S. Chlopicki and M. Baranska, *Analyst*, 2015, 140, 2321–2329.

207   A. M. Schwartzberg, T. Y. Oshiro, J. Z. Zhang, T. Huser and C. E. Talley, *Anal. Chem.*, 2006, 78, 4732–4736.

208   J. P. Scaffidi, M. K. Gregas, V. Seewaldt and T. Vo-Dinh, *Anal. Bioanal. Chem.*, 2009, 393, 1135–1141.

209   J. Kneipp, H. Kneipp, B. Wittig and K. Kneipp, *J. Phys. Chem. C*, 2010, 114, 7421–7426.

210 C. E. Talley, L. Jusinski, C. W. Hollars, S. M. Lane and T. Huser, *Anal. Chem.*, 2005, 76, 7064–7068.

211 W. C. Cao, R. Jin and C. A. Mirkin, *Science.*, 2002, 297, 1536–1539.

212 Y. Li, M. Kröger and W. K. Liu, *Biomaterials*, 2014, 35, 8467–8478.

213 J. S. Suk, Q. Xu, N. Kim, J. Hanes and L. M. Ensign, *Adv. Drug Deliv. Rev.*, 2016, 99, 28–51.

214 T. Wang, Y. Guo, Y. He, T. Ren, L. Yin, J. P. Fawcett, J. Gu and H. Sun, *Acta Pharm. Sin. B*, 2020, 1–8.

215 N. Uzunbajakava, A. Lenferink, Y. Kraan, E. Volokhina, G. Vrensen, J. Greve and C. Otto, *Biophys. J.*, 2003, 84, 3968–3981.

216 F. M., *The Endothelium: Part 1: Multiple Functions of the Endothelial Cells–Focus on Endothelium-Derived Vasoactive Mediators*, Morgan & Claypool Life Sciences Publishers, 2011.

217 L. Liendl, J. Grillari and M. Schosserer, *GeroScience*, 2020, 42, 377–387.

218 J. Kneipp, H. Kneipp, M. McLaughlin, D. Brown and K. Kneipp, *Nano Lett.*, 2006, 6, 2225–2231.

219 Z. Movasaghi, S. Rehman and I. U. Rehman, *Appl. Spectrosc. Rev.*, 2007, 42, 493–541.

220 M. J. Stoddart, *Mammaliam Cell Viability: Methods and Protocols*, Humana Press, 2011, vol. 740.

221 L. R. Hirsch, A. M. Gobin, A. R. Lowery, F. Tam, R. A. Drezek, N. J. Halas and J. L. West, *Ann. Biomed. Eng.*, 2006, 34, 15–22.

222 B. Liu, C. Li, Z. Cheng, Z. Hou, S. Huang and J. Lin, *Biomater. Sci.*, 2016, 4, 890–909.

223 S. Preciado-Flores, D. Wang, D. A. Wheeler, R. Newhouse, J. K. Hensel,

A. Schwartzberg, L. Wang, J. Zhu, M. Barboza-Flores and J. Z. Zhang, *J. Mater. Chem.*, 2011, 21, 2344–2350.

224 A. M. Goodman, Y. Cao, C. Urban, O. Neumann, C. Ayala-Orozco, M. W. Knight, A. Joshi, P. Nordlander and N. J. Halas, *ACS Nano*, 2014, 8, 3222–3231.

225 S. J. Oldenburg, R. D. Averitt, S. L. Westcott and N. J. Halas, *Chem. Phys. Lett.*, 1998, 288, 243–247.

226 B. G. Prevo, S. A. Esakoff, A. Mikhailovsky and J. A. Zasadzinski, *Small*, 2008, 4, 1183–1195.

227 Q. Q. Ren, L. Y. Bai, X. S. Zhang, Z. Y. Ma, B. Liu, Y. Di Zhao and Y. C. Cao, *J. Nanomater.*, 2015, 2015, 1–7.

228 Y. Sun, B. Mayers and Y. Xia, *Adv. Mater.*, 2003, 15, 641–646.

229 Z. S. Zhang, Z. J. Yang, X. L. Liu, M. Li and L. Zhou, *Scr. Mater.*, 2010, 63, 1193–1196.

230 H. P. Liang, L. J. Wan, C. L. Bai and L. Jiang, *J. Phys. Chem. B*, 2005, 109, 7795–7800.

231 A. M. Schwartzberg, T. Y. Olson, C. E. Talley and J. Z. Zhang, *J. Phys. Chem. B*, 2006, 110, 19935–19944.

232 W. Lu, Q. Huang, G. Ku, X. Wen, M. Zhou, D. Guzatov, P. Brecht, R. Su, A. Oraevsky, L. V. Wang and C. Li, *Biomaterials*, 2010, 31, 2617–2626.

233 W. Lu, C. Xiong, G. Zhang, Q. Huang, R. Zhang, J. Z. Zhang and C. Li, *Cancer Ther.*, 2009, 15, 876–886.

234 J. You, G. Zhang and C. Li, *ACS Nano*, 2010, 4, 1033–1041.

235 R. Weissleder, *Nat. Biotechnol.*, 2001, 19, 316–317.

236 L. R. Hirsch, R. J. Stafford, J. A. Bankson, S. R. Sershen, B. Rivera, R. E. Price, J. D. Hazle, N. J. Halas and J. L. West, *Proc. Natl. Acad. Sci. U. S.*

A., 2003, 100, 13549–13554.

237   W. Lu, G. Zhang, R. Zhang, L. G. Flores ll, Q. Huang, J. G. Gelovani and C. Li, *Cancer Res.*, 2010, 70, 3177–3188.

238   Y. Sun, B. T. Mayers and Y. Xia, *Nano Lett.*, 2002, 2, 481–485.

239   Y. Sun and Y. Xia, *Nano Lett.*, 2003, 3, 1569–1572.

240   W. Wang, M. Dahl and Y. Yin, *Chem. Mater.*, 2013, 25, 1179–1189.

241   N. Leopold and B. Lendl, *J. Phys. Chem. B*, 2003, 107, 5723–5727.

242   J. R. Daniel, L. A. McCarthy, E. Ringe and D. Boudreau, *RSC Adv.*, 2019, 9, 389–396.

243   S. J. Oldenburg, S. L. Westcott, R. D. Averitt and N. J. Halas, *J. Chem. Phys.*, 1999, 111, 4729–4735.

244   V. Vongsavat, B. M. Vittur, W. W. Bryan, J. H. Kim and T. R. Lee, *ACS Appl. Mater. Interfaces*, 2011, 3, 3616–3624.

245   M. H. Kim, X. Lu, B. Wiley, E. P. Lee and Y. Xia, *J. Phys. Chem. C*, 2008, 112, 7872–7876.

246   Y. Liang, J. Liu, T. Liu and X. Yang, *Oncol. Lett.*, 2017, 14, 2254–2260.

247   M. P. Melancon, M. Zhou, R. Zhang, C. Xiong, P. Allen, X. Wen, Q. Huang, M. Wallace, J. N. Myers, R. J. Stafford, D. Liang, A. D. Ellington and C. Li, *ACS Nano*, 2014, 8, 4530–4538.

248   C. Xiong, W. Lu, M. Zhou, X. Wen and C. Li, *Cancer Nanotechnol.*, 2018, 9, 1–13.

249   M. P. Melancon, W. Lu, Z. Yang, R. Zhang, Z. Cheng, A. M. Elliot, J. Stafford, T. Olson, J. Z. Zhang and C. Li, *Mol Cancer Ther*, 2009, 7, 1730–1739.

250   H. Kearns, N. C. Shand, K. Faulds and D. Graham, *Chem. Commun.*,

2015, 51, 8138–8141.

251   M. Chandra, A. M. Dowgiallo and K. L. Knappenberger, *J. Am. Chem. Soc.*, 2010, 132, 15782–15789.

252   D. G. Mackanic, S. Mabbott, K. Faulds and D. Graham, *J. Phys. Chem. C*, 2016, 120, 20677–20683.

253   I. Grabowska-Jadach, D. Kalinowska, M. Drozd and M. Pietrzak, *Biomed. Pharmacother.*, 2019, 111, 1147–1155.

254   S. A. Lindley and J. Z. Zhang, *ACS Appl. Nano Mater.*, 2019, 2, 1072–1081.

255   J. Depciuch, M. Stec, A. Maximenko, J. Baran and M. Parlinska-Wojtan, *J. Mater. Sci.*, 2020, 55, 5257–5267.

256   A. Hatef, S. Fortin-Deschênes, E. Boulais, F. Lesage and M. Meunier, *Int. J. Heat Mass Transf.*, 2015, 89, 866–871.

257   F. Zhang, X. Han, Y. Hu, S. Wang, S. Liu, X. Pan, H. Wang, J. Ma, W. Wang, S. Li, Q. Wu, H. Shen, X. Yu, Q. Yuan and H. Liu, *Adv. Sci.*, 2019, 6, 1–9.

258   L. Cheng, D. Jiang, A. Kamkaew, H. F. Valdovinos, H. J. Im, L. Feng, C. G. England, S. Goel, T. E. Barnhart, Z. Liu and W. Cai, *Adv. Funct. Mater.*, 2017, 27, 1–10.

259   P. . Michelle Longmire, Peter L. Choyke, M.D., and Hisataka Kobayashi, M.D., *Nanomedicine*, 2012, 3, 703–717.

260   S. C. Gad, K. L. Sharp, C. Montgomery, J. D. Payne and G. P. Goodrich, *Int. J. Toxicol.*, 2012, 31, 584–594.

261   M. Borzenkov, G. Chirico, L. D'Alfonso, L. Sironi, M. Collini, E. Cabrini, G. Dacarro, C. Milanese, P. Pallavicini, A. Taglietti, C. Bernhard and F. Denat, *Langmuir*, 2015, 31, 8081–8091.

7. Appendices

## Appendix 1: Biosynthesis Pathway of Cholesterol

Figure 7.1: Biosynthesis pathway of cholesterol. Reprinted by permission from Springer Nature: [Springer Nature] [Nature Metabolism] [B. Huang, B. liang Song and C. Xu, *Nat. Metab.*, 2020, 2, 132–141], [Copyright©] (2020).

Appendix 2: Un-Normalised Extinction Spectrum of Conjugates
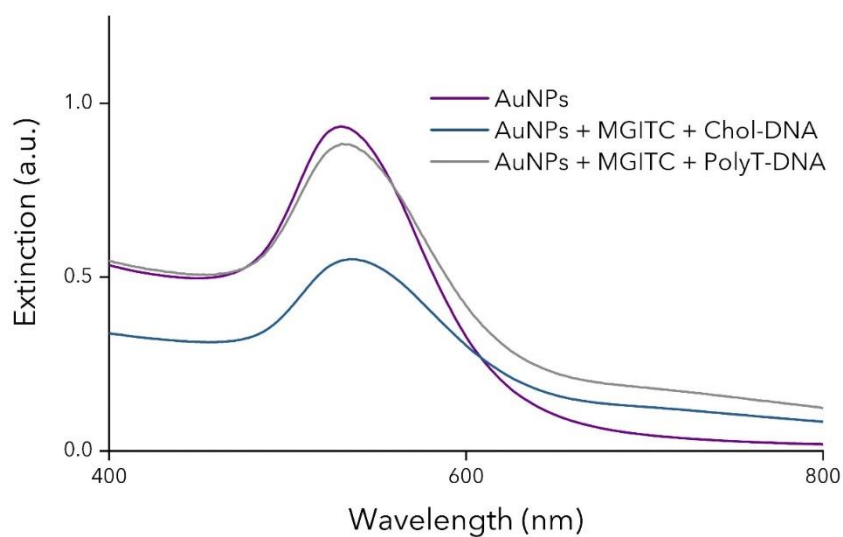


Figure 7.2: Extinction spectra of bare AuNPs (purple), cholesteryl-TEG functionalised AuNPs (blue) and PolyT functionalised AuNPs (grey). Spectra were acquired at a baselined scan rate of 600 nm/min, with three replicates. Spectra were averaged using Microsoft® Excel and Origin®.

The confidence interval results determine the degree of probability that the 'true' mean will fall between a range of values. The table below gives the ranges for 90, 95 and 99 % certainty for where the 'true' mean can lie.

Table 2: Confidence interval values obtained from the Student's t-test.

Conf. Levels in %	Lower Limits	Upper Limits
90	3.1	8.4
95	2.5	8.9
99	1.4	10.1
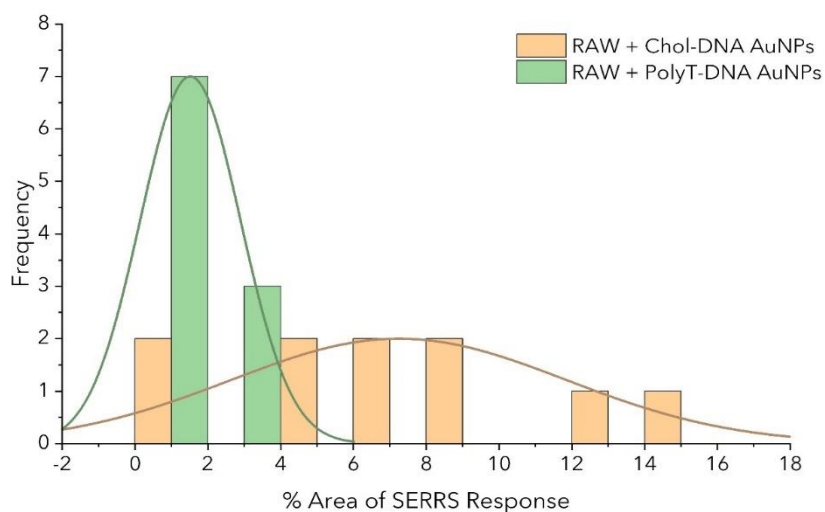
Figure 7.3: Histogram depicting the spread of % area SERRS response from 10 biological repeats of chol-DNA AuNPs and its control, polyT-DNA AuNPs. Diagram shows a larger spread of values from the chol-DNA conjugates in comparison to the control.

Figure 7.4: Comparison of intensity of silica standard on the inVia Raman confocal spectrometer at 5% and 10% laser power.

Table 3: Confidence interval values obtained from the Student's t-test.

| Conf. Levels in %	Lower Limits	Upper Limits
90	10.3	21.8
95	9	23
99	6.4	25.6
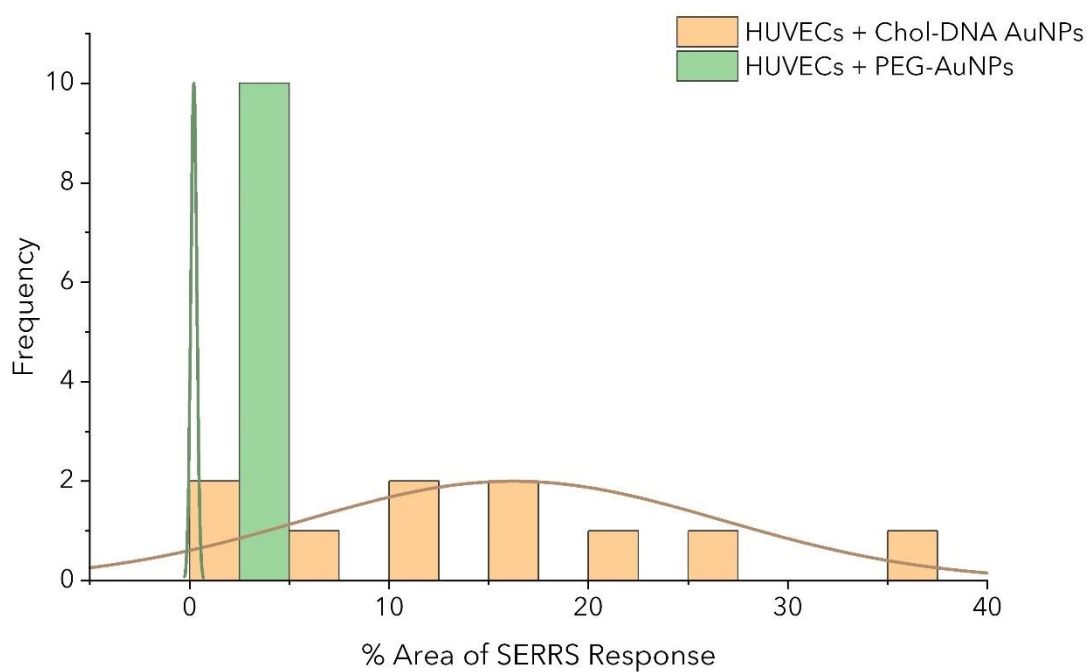
Figure 7.5: Histogram depicting the spread of % area SERRS response from 10 biological repeats of chol-DNA AuNPs and its control, PEG-AuNPs. Diagram shows a larger spread of values from the chol-DNA conjugates in comparison to the control.

Appendix 6: Extinction Spectrum of Synthesised HGNs with a LSPR of 748 nm
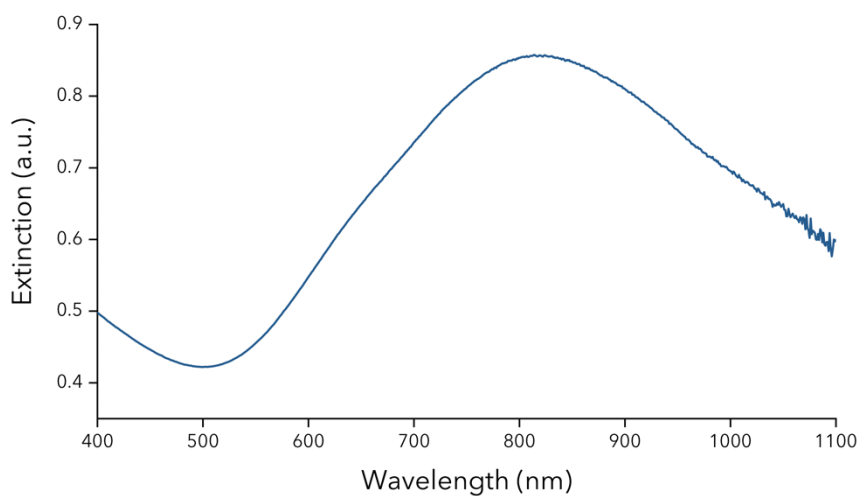

Figure 7.6: Extinction spectrum of HGNs showing a LSPR of 748 nm. The data presented is an average of three spectra taken at a scan rate of 600 nm/min.

## Appendix 7: Un-Normalised Extinction Spectrum of Chol-DNA HGNs
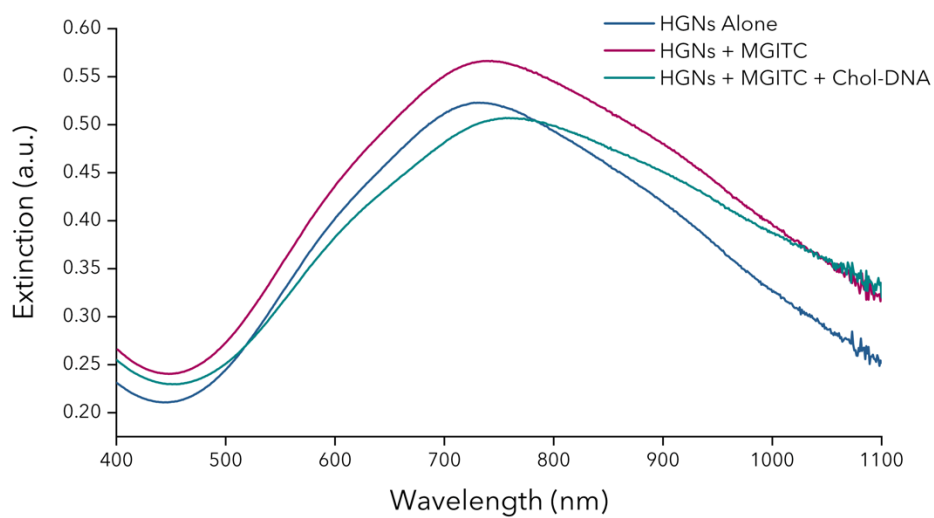
Figure 7.7: Un-normalised extinction spectra from the HGN functionalisation experiment showing HGNs alone (blue), HGNs + MGITC (purple), HGNs + MGITC + Chol-DNA (Teal). Spectra were acquired at a baselined scan rate of 600 nm/min, with three replicates. Spectra were averaged using Microsoft® Excel and Origin®.

## Appendix 8: Extinction spectra Comparing Control HGNs to Batch HGNs
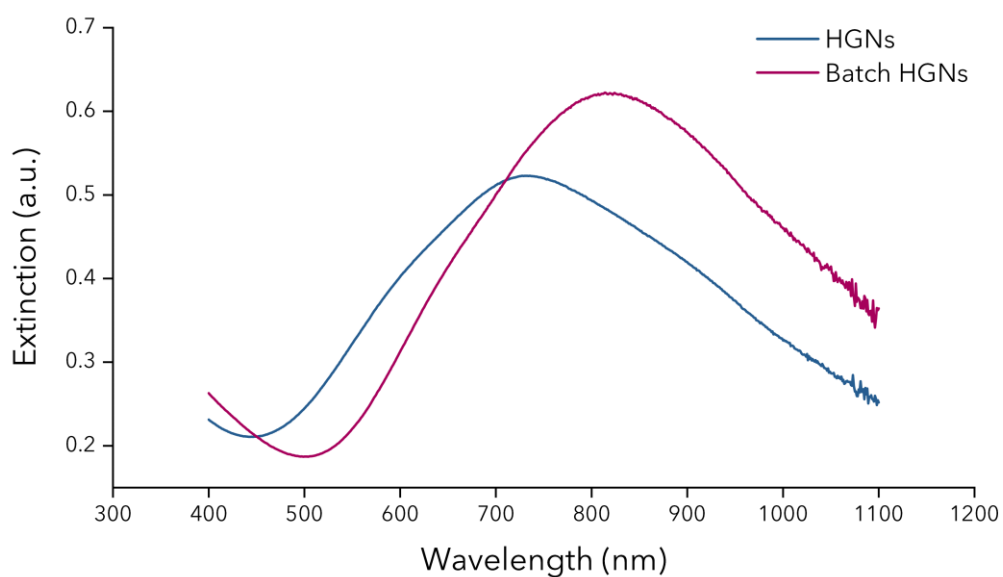
Figure 7.8: Extinction spectra comparing HGNs from the functionalisation experiment to the batch HGNs. Spectra were acquired at a baselined scan rate of 600 nm/min, with three replicates. Spectra were averaged using Microsoft® Excel and Origin®.

Appendix 9: Visual Comparison of Bare and Functionalised HGNs
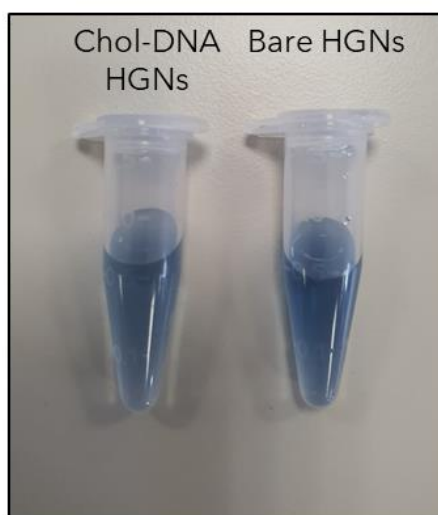
Figure 7.9: Image of Chol-DNA HGNs (left) and bare HGNs (right) after one week of synthesis.

8. List of Publications and Presentations

Publications:

1. "Extreme Red Shifted Nanotags," M. A. Bedics, H. Kearns, J. M. Cox, S. Mabbott, **F. Ali**, N. C. Shand, K. Faulds, J. B. Benedict, D. Graham, M. R. Detty, Chemical Science, 2015, 6, 2302-2306.

2. "Sensitive SERS Nanotags for Use with a Hand-Held 1064 nm Raman Spectrometer." H. Kearns, **F. Ali**, M. A. Bedics, N. Shand, K. Faulds, M. R. Detty, D. Graham, Royal Society Open Science, 2017, 4, 1-9.

Presentations:

1. "Using Cholesterol Modified Nanoparticles as Agents for Cardiovascular Disease Systems," Spring SciX, Glasgow, 2018, (*Poster*).

2. "Using Cholesterol Modified Nanoparticles as Agents for Cardiovascular Disease Systems," Strath-Wide, Glasgow, 2018, (*Oral*).

3. "Using Cholesterol Modified Nanoparticles as Agents for Cardiovascular Disease Systems," ARF, London, 2018, (*Poster*).

4. "Using Cholesterol Modified Nanoparticles as Agents for Cardiovascular Disease Systems," GRC/GRS, Rhode Island (USA), 2018, (*Poster*).

5. "Using Cholesterol Modified Nanoparticles as Agents for Cardiovascular Disease Systems," FACSS SciX, Palm Springs (USA), 2019, (*Oral*).